Theoretical design for artificial spin-triplet superconductors

Jaechul Lee

A thesis presented for the degree of
Doctor of Philosophy

Division of Applied Physics
Graduate School of Engineering
Hokkaido University

March 25, 2025

Theoretical design for artificial spin-triplet superconductors

Jaechul Lee

Abstract

The proximity effect has been an important issue in the physics of superconductivity. In a normal-metal/superconductor (NS) junction, Cooper pairs penetrate from a superconductor into a normal metal, and modify its electromagnetic and thermal properties. Such effect is called proximity effect. For instance, a normal metal in an NS junction indicates large diamagnetic response to an external magnetic field and has the gapped energy spectra at the Fermi level. The degree of the proximity effect depends on the junction parameters such as the transparency of a junction interface and the degree of disorder in a normal metal. In addition, the symmetry of the pair potential in a superconductor is a key parameter that changes the proximity effect qualitatively. The symmetry of the pair potential is categorized into two classes: spin-singlet even-parity and spin-triplet odd-parity. Spin-singlet s-wave superconductivity occurs in many metallic superconductors. Superconductivity in high-Tc cuprates belongs to spin-singlet d-wave symmetry class. However, spin-triplet superconductors are very rare. At present, only several heavy-fermionic compounds are candidates of spin-triplet superconductors. However, the spin-triplet superconductivity in these materials has not yet been confirmed. Theoretical studies from 2002 to 2007 have suggested very unusual transport properties in NS junctions consisting of spin-triplet superconductors. For example, the differential conductance in a spin-triplet p-wave NS junction at zero-bias is quantized irrespective of the transparency at the junction interface and the degree of disorder in a normal metal. Such remarkable phenomenon is called anomalous proximity effect (APE). At that time, microscopic mechanisms of the APE were not clear at all. Therefore, the APE was considered as a phenomenon unique to spin-triplet superconductors. Phenomenologically, the APE was understood as an interference phenomenon between two phase coherent effects: the formation of Andreev bound states at the junction interface and the usual proximity effect in a normal metal. The former is realized when the pair potential is an odd function of wavenumber in the current direction. The latter is realized when the pair potential is an even function of wavenumber in the transverse direction to the current. Only spin-triplet p-wave pair potentials satisfy these conditions. To observe the anomalous proximity effect in experiments, prescriptions for synthesizing artificial spin-triplet superconductors by combining existing materials and existing technologies. In 2015-2016, several theoretical studies show that the quantized value of the conductance is described well by an invariant $\mathcal{N}$ which is called Atiyah-Singer index and represents the number of resonant transmission channels at zero energy in a normal metal. In these theories, chiral symmetry of Hamiltonian is a key property that explains stability of highly degenerate zero-energy states in a dirty normal metal.

In this thesis, we propose theoretical recipes for artificial spin-triplet superconductors. Spin-orbit interactions have been important items that realizes topologically nontrivial electronic in various materials such as topological insulators, topological semimetals, and topological superconductors. Specific properties in topological materials can be tuned by controlling types of spin-orbit interactions such as Rashba type, Dresselhaus type, and spin helix type. In this thesis, we consider spin-singlet d-wave superconductors with spin helix type spin-orbit interactions. In a spin-singlet d-wave superconductor, the Andreev bound states are present, but the proximity effect is absent. A spin helix type spin-orbit interaction enables the proximity effect in a normal metal. In another spin-singlet d-wave superconductor, the Andreev bound states are absent, but the proximity effect is present. Another specific spin helix type spin-orbit interaction enables the Andreev bound states at the junction interface. As a result of introducing spin helix type spin-orbit interactions, such artificial superconductor indicates the APE. Namely artificial spin-triplet superconductivity is realized in a spin-singlet superconductor with a spin-orbit interaction. These studies indicate that the APE is the unusual phenomenon of superconductors that have nontrivial Atiyah-Singer index.

Acknowledgements

First of all, I would like to express my sincere gratitude to my supervisor, Prof. Yasuhiro Asano, for his continuous support throughout my graduate studies. His mentorship has been essential not only in deepening my understanding of physics but also in enriching my academic journey by mentoring me in effective presentation, scholarly writing, and principles of philosophical inquiry. His unwavering encouragement, immense knowledge, and patience have guided me at every step. He is not only a mentor, but also a lasting source of inspiration, particularly in the way I approach life.

I would also like to thank Prof. Kousuke Yakubo and Associate Prof. Hideaki Obuse for their invaluable advice on my research presentations and for teaching me how to effectively communicate with fellow scientists. In addition, I am deeply grateful to Prof. Byungwon Kang and Prof. Kyugnwan Kim, without whose guidance and support I could not have embarked on this journey. I would also like to extend my gratitude to the Asahi Glass Foundation for their generous financial support, which has been instrumental in my Ph.D. studies.

Lastly, I would like to express my heartfelt appreciation to my dear friends, Doosan Shin, Jinsu Son, and Jaeil Choi, for their unwavering support and constant motivation.

Contents

Chapter 1

General Introduction

1.1 Anomalous proximity effect

The proximity effect has been an important issue in the physics of superconductivity. In a normal-metal/superconductor (NS) junction, Cooper pairs penetrate from a superconductor into a normal metal and modify its electromagnetic and thermal properties. Such effect is called proximity effect. [1] For instance, a normal metal in an NS junction indicates large diamagnetic response to an external magnetic field and has the gapped energy spectra at the Fermi level. [2, 3] The Josephson current in superconductor/normal-metal/superconductor (SNS) flows as a result of the penetration of Cooper pairs into the normal-metal from the two superconductors. The degree of the proximity effect depends on the junction parameters such as the transparency of a junction interface and the degree of disorder in a normal metal. In addition, the symmetry of a superconductor is a key parameter that changes the proximity effect qualitatively. [4, 5, 6] It has been established that the electric transport properties in an NS junction show in Fig. 1.1 depend sensitively on the symmetry of the pair potential, where a superconductor is attached to a normal metal through a potential barrier. The electric current flows in the x direction and width of the junction in the y direction is W. The resistance at zero bias of an NS junction calculated based on the quasiclassical Green's function method is plotted as a function of the resistance of the normal metal R_{N}. In Fig. 1.1, the arrow points the normal resistance of the potential barrier R_{B}. In the classical mechanics, the total differential resistance at zero bias in such a junction is given by

$$R_{\mathrm{NS}} = R_{\mathrm{B}} + R_{\mathrm{N}}. \tag{1.1}$$

In quantum mechanics, the resistance at zero bias is represented as

$$R_{\mathrm{NS}} = \tilde{R}_{\mathrm{B}} + \tilde{R}_{\mathrm{N}}. \tag{1.2}$$

The phase coherent effects renormalize the resistance $\tilde{R}_{\mathrm{B}}$ and $\tilde{R}_{\mathrm{N}}$ in various ways depending on symmetries of the pair potential.

In an unconventional superconductor, the pair potential $\Delta(k_x, k_y)$ changes its sign on the Fermi surface, where we consider two-dimensional momentum space and k_x (k_y) is the wavenumber in the x (y) direction on the Fermi surface, (i.e., $k_x^2 + k_y^2 = k_F^2$). In Fig. 1.2, the schematic picture of the pair potential is illustrated on the two-dimensional Fermi surface. The presence of the proximity effect in a normal metal is described by[4]

$$\Delta(k_x, -k_y) \neq -\Delta(k_x, k_y). \tag{1.3}$$

In an unconventional superconductor, two types of Cooper pairs penetrate into a dirty normal metal. One originates from the positive part of the pair potential and the other originates from the negative part of the pair potential. When the pair potential is an odd function of k_y, the amplitudes of the two pairing correlations are equal to each other. Therefore, the pairing correlation vanishes in a dirty normal metal. As a result, the proximity effet is absent in a dirty metal and $\tilde{R}_{\mathrm{N}} = R_{\mathrm{N}}$. The pair potentials in d_{xy}- and p_y-wave symmetry are odd function of k_y. Therefore the zero bias resistance in these symmetries increases linearly with R_{N} as shown in Fig. 1.1. In s-wave and p_x-wave junction, the proximity effect changes the resistance of a normal metal to $\tilde{R}_{\mathrm{N}}$. The resistance deviates from the linear relationship in these cases. The surface Andreev bound states appear when the pair potential satisfies[7, 8]

$$\Delta(-k_x, k_y)\,\Delta(k_x, k_y) < 0. \tag{1.4}$$

The Andreev bound states at the NS interface decrease R_{B}, indicated by an horizontal arrow in Fig. 1.1, to $\tilde{R}_{\mathrm{B}}$ for d_{xy}- and p_x-wave junctions. The Sharvin conductance of the junction is defined by

$$G_{\mathrm{Sharvin}} = \frac{2e^2}{h} N_c, \tag{1.5}$$

$N_c = W k_F/\pi$ is the number of propagating channels on the Fermi surface, W is the width of the junction, k_F is the Fermi wavenumber, and spin degree of freedom of an electron arises a factor 2. In d_{xy}- and p_x-wave junctions $\tilde{R}_{\mathrm{B}}$ becomes

$$R_0 = \left[2G_{\mathrm{Sharvin}}\right]^{-1}, \tag{1.6}$$

where an extra factor 2 is derived from the perfect Andreev reflection. In Table 1.1, the unconventional pair potentials are classified according to whether they satisfy Eqs. (1.3) and (1.4). The resistance obey Eq. (1.1) for a p_y-wave junction because both the proximity effect in a normal metal and the Andreev bound states at an NS interface are absent. As a result, the total resistance increases linearly with R_{N} from R_{B}. In an d_{xy}-wave junction, the surface bound states decreases the resistance due to a potential barrier to $\tilde{R}_{\mathrm{B}} = R_0$.

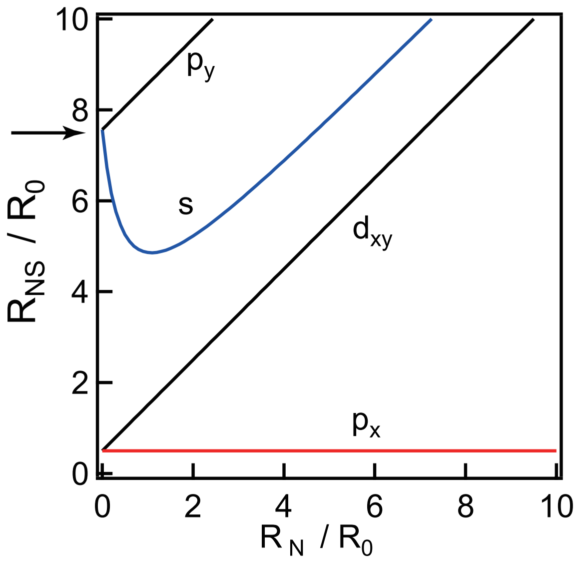

Figure 1.1: The resistance of an NS junction consisting of an unconventional superconductor is plotted as a function of the resistance of a normal metal R_N. The arrow points the resistance due to the potential barrier R_B. The conductance is calculated based on the quasiclassical Green's function method, where the Keldysh-Usadel equation is solved under appropriate boundary conditions.[5]

R_NS in this case also increases linearly with R_N because the proximity effect is absent in a normal metal. The results for an s-wave junction decreases from R_B with the increase of R_N then increases. Such reentrant behavior of the resistance is a result of the usual proximity effect [9, 10] which is caused by the multiple Andreev reflection near an NS interface. Finally in a p_x-wave junction, the resistance depends on neither R_B nor R_N. The Andreev reflection is always perfect even in the presence of the potential barrier and random impurities. This effect is called anomalous proximity effect. [5] Such drastic effect can be seen only in the zero-bias resistance or the zero-bias conductance. The conductance is quantized at

$$G_\mathrm{NS} = R_0^{-1} = \frac{4e^2}{h} N_c. \tag{1.7}$$

The perfect transmission of a Cooper pair through a dirty normal metal also causes the low-temperature anomaly in an SNS junction. [6] Phenomenologically, the anomalous proximity effect is understood as an interplay between the proximity effect in normal metals and the formation of bound states at the interface. However, it took more than a decade to reach a microscopic understanding of the anomalous proximity effect.

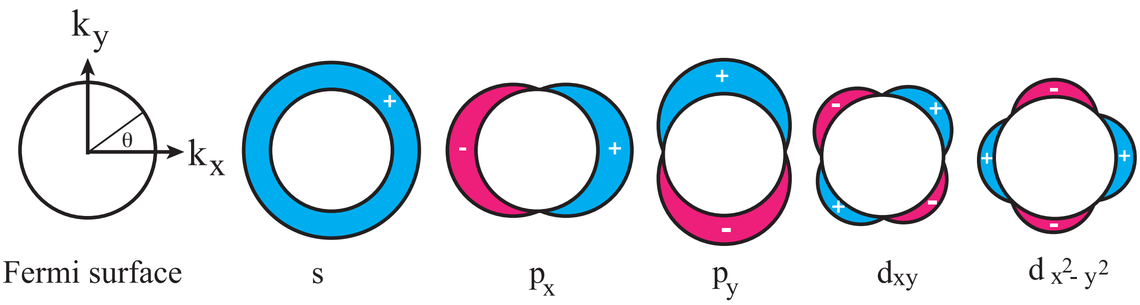

Figure 1.2: Pair potentials on the Fermi surface in two dimension.

Table 1.1: The relationship between the symmetry of the pair potential and the presence or absence of the two interference effects. The current flows in the x direction.

symmetry	s, $d_{x^2-y^2}$	d_{xy}	p_y	p_x
proximity effect	○	×	×	○
surface bound states	×	○	×	○

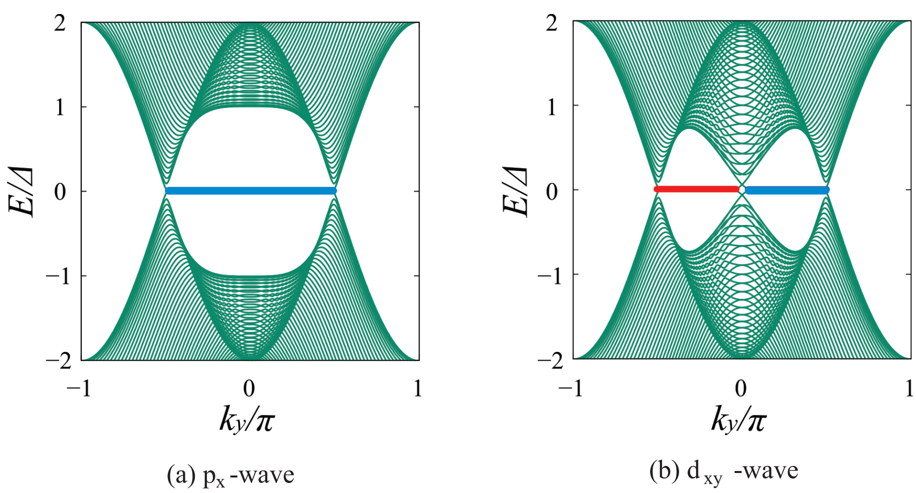

Figure 1.3: The eigenvalues of the BdG Hamiltonian are plotted as a function of k_y on a two-dimensional tight-binding model, where the periodic (hard wall) boundary boundary condition is applied in the y (x) direction. The Green dots represents the eigenvalue of the uniform states in the bulk. The blue and red dots indicate zero-energy states at a surface of $x = 0$ belonging to positive (negative) chiral states.

1.2 Atiyah-Singer Index

To explain the mechanism of the anomalous proximity effect, the analysis of the chiral property of the surface Andreev bound states at zero energy (Fermi level) is necessary. Chiral symmetry of the Bogoliubov-de Gennes (BdG) Hamiltonian

$$\Gamma\, H_{\mathrm{BdG}}\, \Gamma = -H_{\mathrm{BdG}},\ \Gamma^2 = 1, \tag{1.8}$$

has been used frequently to characterize the topologically nontrivial superconducting states [11, 12, 13]. The eigenvalues of the chiral operator Γ are either $\gamma = 1$ or -1. A mathematical theorem suggests two important features of the eigenstates of H_{BdG}

(i) The eigenstates of H_{BdG} at zero energy are simultaneously the eigenstates of Γ. Namely, the eigenstates at zero energy are classified into the positive chiral states with $\gamma = 1$ or negative chiral states belonging to $\gamma = -1$.

(ii) In contrast to the zero-energy states, the nonzero-energy states are not the eigenstates of Γ. They are described by an equal-weight linear combination of two zero-energy states: one has $\gamma = 1$ and the other has $\gamma = -1$.

The BdG Hamiltonian of superconductors in Table 1.1 preserves chiral symmetry. The superconducting states are topologically characterized by applying the dimensional reduction [13], where we consider one-dimensional Brillouin zone by fixing k_y at a certain value. The winding number can be defined in such a one-dimensional Brillouin zone as

$$\mathcal{W}(k_y) = \mathrm{sgn}[\Delta(k_x, k_y)], \tag{1.9}$$

when Eq. (1.4) is satisfied at k_y. The surface Andreev bound states appear as a result of the bulk-boundary correspondence of a topologically nontrivial superconducting states. In Fig. 1.3, the eigenvalues of the BdG Hamiltonian are plotted as a function of k_y on a two-dimensional tight-binding model, where the periodic (hard wall) boundary boundary condition is applied in the y (x) direction. The Green dots represent the eigenvalue of the uniform states in the bulk. The blue and red dots indicate zero-energy states at a surface of $x = 0$ belonging to positive (negative) chiral states. It is possible redefine the chiral operator Γ in Eq. (1.8) so that its eigenvalue is equal to the winding number, (i.e. $\gamma = \mathcal{W}$). We note that surface bound states are absent for s-wave and p_y-wave junctions as shown in Table 1.1. Fig. 1.3 shows that the degree of the degeneracy at zero energy is $N_c = Wk_F/\pi$ per spin at a surface of the p_x-wave and d_{xy}-wave superconductors. Such surface states are called flat band zero-energy states. The number of zero-energy states belonging to $\gamma = 1$ ($\gamma = -1$) is N_+ (N_-). The anomalous proximity effect happens because the flat band zero-energy states penetrate into a dirty normal metal with retaining their high degeneracy and form the resonant transmission channels at zero-energy. This is a phenomenological understanding of the anomalous proximity effect at 2007.

Quantum mechanics suggests that the large degree of the degeneracy is a result of high symmetry of the Hamiltonian. In Fig. 1.3, we consider one-dimensional Brillouin zone to characterize the superconducting states topologically by assuming the translational symmetry in the y direction. The large degree of degeneracy at the flat band zero-energy states are direct consequence of translational symmetry of the Hamiltonian. Therefore, random impurities would lift the degeneracy because they break translational symmetry. Theorems (i) and (ii) explain why the anomalous proximity effect happens in a p_x-wave junction and why the proximity effect is absent in a d_{xy}-wave junction. For a d_{xy}-wave junction, a half of the zero-energy states belong to the positive chiral eigenvalue $\gamma = 1$ and a rest half belongs to the negative eigenvalue $\gamma = -1$. According to theorem (ii), a positive chiral zero-energy state and a negative chiral zero-energy state couple to each other in the presence of random impurities in the normal metal, and form two nonzero energy states. As a result, the high degeneracy at zero energy is lifted due to impurities, which explains the absence of anomalous proximity effect in a d_{xy}-wave NS junction. In a p_x-wave junction, all the flat band zero-energy states belong to the positive chiral eigenvalue. Therefore, according to theorem (ii), they retain the large degree of the degeneracy even in the presence of random impurities. Their chiral partner stay the opposite end of the p_x-wave superconductor.[14] Theorem (i) also explains the reason of the perfect Andreev reflection at the NS interface at $x = 0$.[14] The number of zero-energy states penetrating into a dirty normal metal is described by

$$N_{\mathrm{ZES}} = \sum_{k_y} \mathcal{W}(k_y). \tag{1.10}$$

By its definition N_{ZES} is a topological invariant. Since

$$N_{\mathrm{ZES}} = N_+ - N_-, \tag{1.11}$$

the N_{ZES} is simultaneously an invariant defined by using the solutions of the differential equation. Such integer number is called Attiyah-Singer index, which is an invariant in mathematics. The conductance is quantized at

$$G_{\mathrm{NS}} = \frac{4e^2}{h} N_{\mathrm{ZES}}. \tag{1.12}$$

By applying the argument above, it is possible to discuss a universal property of the conductance in NS junction of a superconductor preserving chiral symmetry. The zero-bias conductance is summarized as

$$\lim_{R_{\mathrm{N}} \to \infty} G_{\mathrm{NS}} = \frac{4e^2}{h} N_{\mathrm{ZES}}. \tag{1.13}$$

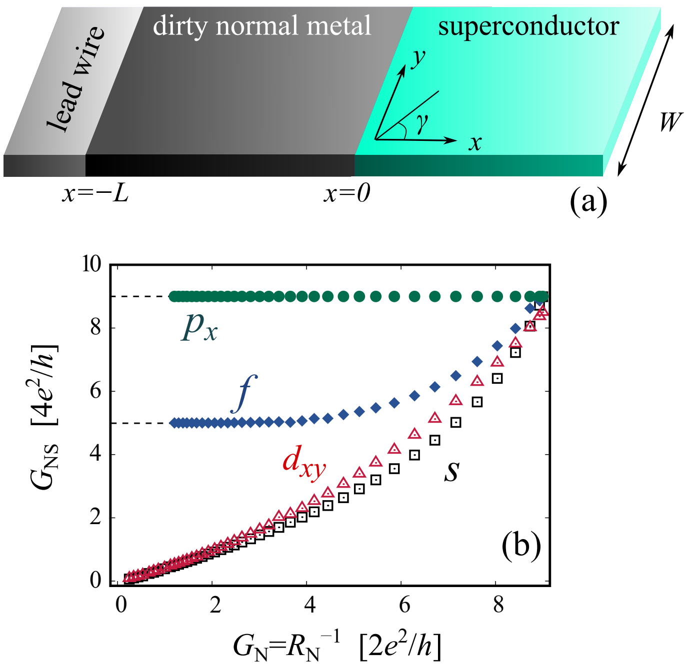

Figure 1.4: The conducrtance is plotted as a function of the conductance of a normal metal $G_{\rm N}$. The results for an f-wave junction decreases with decreasing $G_{\rm N}$ and saturates at 5 $(4e^2/h)$ in the limit of $G_{\rm N} = 0$. [15]

The number of resonant transmission channels in a normal metal $N_{\rm ZES}$ remains unchanged even in $R_{\rm N} \to \infty$. In this limit, electron transport is possible only through the resonant channels at zero energy. In NS junctions in Fig. 1.1, $N_{\rm ZES} = 0$ holds for s-, p_y-, and d_{xy}-wave cases, and $N_{\rm ZES} = N_c$ for p_x-wave case. The validity of the argument is checked in a f-wave junction whose pair potential is described by $\Delta(\hat{\boldsymbol{k}}) = \Delta k_x(k_F^2 - 2k_y^2)/k_F^3$. It is possible to estimate the index as

$$N_{\rm ZES} = \left[N_c(\sqrt{2} - 1) \right]_{\rm G}, \tag{1.14}$$

where $[\cdots]_{\rm G}$ means the integer part of a number. Numerical results of the conductance are shown in Fig. 1.4. The conductance for spin-singlet junctions goes to zero in the limit of $G_{\rm N} = 0$ as shown with lines indicated by s and d_{xy}. The results for a p_x-wave is constant at $\frac{4e^2}{h}9$, where $N_{\rm ZES} = 9$ as $N_c = 9$. The conductance for an f-wave junction decreases with decreasing $G_{\rm N}$ and saturates at 5 $(4e^2/h)$ in the limit of $G_{\rm N} = 0$. The Eq. (1.14) means that minimum value of the conductance is quantized at the Atiyah-Singer's index because of the anomalous proximity effect.

Table 1.2: The comparison between Mishra et. al. Ref. [19] and this thesis.

	pair potential	spin-orbit interactions	anomalous proximity effect
Mishra et. al.	$s+p$-wave	absent	$\circ$
This thesis	s-wave	present	$\times$
	d-wave	present	$\circ$

1.3 An experiment in T-shaped junctions

In 2007, Asano et. al., proposed an experiment that enables us to distinguish spin-triplet superconductors from spin-singlet ones.[16] The anomalous proximity effect of a spin-triplet odd-parity superconductor plays a key role in their proposal. According to the proposal, the differential conductance in a T-shaped NS junction show the zero-bias peak (dip) when a normal metal is connected to a spin-triplet (spin-singlet) superconductor. The zero-bias dip structure for a spin-singlet superconductor had been observed in a number of T-shaped proximity junctions. In 2021, an experiment reported a clear zero-bias peak in a T-shaped junction connecting to $CoSi_2$.[17] The results suggest spin-triplet superconductivity in $CoSi_2$. However, spin-singlet s-wave superconductivity has been well-established in a bulk $CoSi_2$.[18] A theory tried to fill the gap between the theory and the experiment.[19] In the experiment, a thin film of $CoSi_2$ is grown on a Si substrate. X-ray diffraction and high-resolution TEM measurements confirmed that the films have a high-quality crystalline structure with a sharp $CoSi_2$/Si interface. Furthermore, analysis of weak-antilocalization magnetoresistance allowed them to extract the spin-orbit scattering time, from which they inferred a spin-orbit interaction energy roughly 20 times larger than the superconducting gap energy. The authors of Ref. [19] assumed a spin-triplet p-wave pair potential as well as spin-singlet s-wave pair potential and recover the zero-bias peak in the conductance of a T-shaped junction. At present, however, the validity of the p-wave superconductivity in $CoSi_2$ is not clear.

1.4 Purpose of this thesis

Table 1.1, Eqs. (1.3) and (1.4) suggest that odd-parity pair potentials are a sufficient condition of a superconductor that indicates the anomalous proximity effect. However, unfortunately, spin-triplet odd-parity superconductors are very rare material. Only several uranium compounds such as UBe_{13}, UGe_2, and UTe_2 are candidates of the spin-triplet superconductor. But triplet superconductivity in these materials are still under debate. Under these circumstance, it would be very difficult to observe the anomalous proximity effect in experiments. This argument is true when the BdG Hamiltonian can be block diagonalized into two spin subspaces, where the BdG Hamiltonian is described effectively by 2×2 matrices. In the presence of spin-dependent potentials such as a Zeeman field and spin-orbit interactions, the 4×4 BdG Hamiltonian cannot be block diagonalized any longer. Eq. (1.13) implies that it could be possible to observe the anomalous proximity effect if we find chiral symmetry in 4×4 BdG Hamiltoninan and find a superconducting state that gives $N_{\mathrm{ZES}} \neq 0$.

A purpose of this thesis is to propose a theoretical prescription that enables a superconductor indicating the anomalous proximity effect by combining existing materials and existing technologies. Spin-orbit interactions play a key role in symmetry commversion between spin-singlet even parity and spin-triplet odd-parity. In what follows, we always assume pair potentials belonging to spin-singlet symmetry class, (i.e., $\hat{\Delta} = \Delta(\boldsymbol{k})\, i\hat{\sigma}_y$). We also introduce spin-orbit interactions described by

$$H_{\mathrm{SOI}} = \begin{cases} \lambda k_x \sigma_y & : x\text{−type} \\ -\lambda k_y \sigma_x & : y\text{−type} \\ \lambda(k_y \sigma_x - k_x \sigma_x) & : \text{Rashba,} \end{cases} . \tag{1.15}$$

The last one is known as Rashba spin-orbit interaction derived from lacking inversion symmetry in the z direction. The first and second interaction cause the superspin-helix states in semiconductor physics. Such magnetically active interactions generate spin-triplet odd-parity Cooper pairs in a spin-singlet superconductor. The existence of a Cooper pairs are described by the anomalous Green's function

$$\hat{F}(\boldsymbol{k}) = F^{\mathrm{S}}(\boldsymbol{k})\, i\hat{\sigma}_y + \boldsymbol{F}^{\mathrm{T}}(\boldsymbol{k}) \cdot \boldsymbol{\sigma}\, i\hat{\sigma}_y. \tag{1.16}$$

The definition of the Green's function will be given in succeeding sections. Here we highlight only an important point of argument. The first term represents a spin-singlet Cooper pair that forms the pair potential through the gap equation

$$\hat{\Delta}(\boldsymbol{k})\, i\hat{\sigma}_y \propto \frac{1}{V_{\mathrm{vol}}} \sum_{\boldsymbol{p}} g(\boldsymbol{k} - \boldsymbol{p}) \hat{F}(\boldsymbol{k}), \tag{1.17}$$

where g represents an attractive interaction working between two electrons with opposite spins to each other and enables a spin-singlet Cooper pair. Therefore, only the spin-singlet correlation F^{S} contributes to the pair potential. The spin-triplet Cooper pairs exist as the pairing correlation described by F^{T} but do not contribute to the pair potential. However, we will show that spin-triplet Cooper pairs generated by spin-orbit interactions cause the anomalous proximity effect.

Chapter **2**

Odd-parity pairing correlations in a d-wave superconductor

Abstract

We discuss the effects of spin-orbit interactions on the symmetry of a Cooper pair in a spin-singlet d_{xy}-wave superconductor and on the chiral property of the surface Andreev bound states at zero energy. We demonstrate a spin-orbit interaction induces a spatially uniform spin-triplet p-wave pairing correlation in a superconductor and an odd-frequency spin-triplet s-wave pairing correlation at a surface. The spin-orbit interaction splits the Fermi surface into two depending on the spin configuration. As a result of splitting, the index can be a nontrivial nonzero value. On the basis of the close relationship among the odd-frequency s-wave pairing correlation at a surface, the nonzero index of surface bound states, and the anomalous proximity effect, we provide a design of a superconductor that causes the strong anomalous proximity effect.

2.1 Introduction

The anomalous proximity effect has been considered as a part of Majorana physics [11, 12, 20, 21, 22, 23] because a spin-triplet superconductor hosts Majorana fermions at its surface. Unfortunately, well-established spin-triplet superconductors have never been discovered yet. A recipe for an artificial spin-triplet superconductor is desired to observe the anomalous proximity effect in experiments.

Tamura and Tanaka [24] have studied theoretically the LDOS at a dirty normal metal attached to a d_{xy}-wave superconducting film with the Rashba spin-orbit interaction, where the NS interface is parallel to the y direction as illustrated in Figs. 2.1(a)-(c). Their numerical results indicate signs of the anomalous proximity effect. The modest enhancement of the LDOS at the zero energy suggests the penetration of the zero-energy states (ZESs) into a dirty metal. In addition, they found an odd-frequency spin-triplet s-wave Cooper pair in the normal metal. (See recent review papers on odd-frequency pairing correlations.[25, 26]) Although the signal of the proximity effect is very weak, the results are highly nontrivial due to reasons as follows. It has been already established in the absence of spin-orbit interactions that a d_{xy}-wave superconductor in Fig. 2.1 (c) does not exhibit any proximity effect in a dirty metal [4, 27, 28]. Spin-orbit interaction may induce a spin-triplet Cooper pair in a spin-singlet superconductor [29, 30, 31, 32, 33, 12, 34, 35, 36]. However, mechanisms of the symmetry conversion to an odd-frequency s-wave Cooper are still unclear.

In this chapter, we theoretically study the effects of spin-orbit interactions in a spin-singlet d_{xy}-wave superconductor on symmetry of a Cooper pair and on chiral property of Andreev bound states at its surface. We analyze the symmetry of a Cooper pair by using the anomalous Green's function obtained by solving the Gor'kov equation [37] analytically. The results show that a specific spin-orbit interaction generates a spin-triplet p_x-wave pairing correlation in bulk and an odd-frequency spin-triplet s-wave pairing correlation at a surface. The Bogoliubov-de Gennes (BdG) Hamiltonian of such a d_{xy}-wave superconductor preserves a nontrivial chiral symmetry, which enable us to define an index by using the chiral eigenvalues of surface Andreev bound states at the zero energy. We find that the index, a measure of the strength of the anomalous proximity effect, can be nonzero values only in the presence of the spin-orbit interaction. On the basis of obtained results, we explain why the signs of the anomalous proximity effect in Ref. [24] is weak and provide a design for a superconductor which causes the strong anomalous proximity effect.

2.2 Anomalous proximity effect

In this section, we explain the conductance quantization in an NS junction due to anomalous proximity effect, and necessary conditions for a superconductor exhibiting the anomalous proximity effect.

2.2.1 Chiral property of zero-energy states

The most drastic phenomenon of the anomalous proximity effect may be the quantization of the differential conductance in a NS junction shown in Fig. 2.1(c). The conductance at the zero bias can be described by

$$G_{\mathrm{NS}} = \frac{2e^2}{h}|\mathcal{N}_{\mathrm{ZES}}|, \tag{2.1}$$

in the limit of strong potential disorder in a normal metal, where $|\mathcal{N}_{\mathrm{ZES}}|$ represents a number of the zero-energy states (ZESs) remaining at a dirty surface of a superconductor. [5, 15, 38] We first explain properties of the index $\mathcal{N}_{\rm ZES}$ in the case of a spin-triplet p_x-wave superconductor which is an example of superconductor exhibiting the anomalous proximity effect. At a clean surface of a p_x-wave superconductor, topologically protected bound states appear at the zero energy as a result of a nontrivial winding number $\mathcal{W}(k_y) = \pm 1$ in one-dimensional Brillouin zone. [13] In Fig. A.1(a) in Appendix A, we plot the eigenvalues of the BdG Hamiltonian for a p_x-wave superconductor on a two-dimensional tight-binding lattice. The superconducting gap has two nodes at $k_y = \pm k_F$ with $k_F = \pi/2$ being the Fermi wavenumber. The degree of the degeneracy at the zero energy is equal to the number of propagating channels on the Fermi surface N_c because each propagating channel $-k_F < k_y < k_F$ accommodates a ZES at a surface. We also show the results for a d_{xy}-wave superconductor in Fig. A.1(b). The winding number $\mathcal{W}(k_y)$ can be defined only in the presence of the translational symmetry in the y direction. Therefore, the large degree of degeneracy at the zero energy in both Figs. A.1(a) and (b) is a direct consequence of translational symmetry of the Hamiltonian in the y direction. The zero-bias conductance in such a ballistic NS junction is described by

$$G_{\rm NS} = \frac{2e^2}{h} N_c. \tag{2.2}$$

The results are valid for both a p_x-wave junction and a d_{xy}-wave junction.

Random impurities near the surface may lift the degeneracy at the zero energy because they break translational symmetry. The index $|\mathcal{N}_{\rm ZES}|$ in Eq. (2.1) represents the number of the ZESs remains even in the presence of potential disorder. As discussed in detail later, the index $\mathcal{N}_{\rm ZES}$ can be defined when the Bogoliubov-de Gennes Hamiltonian preserves a chiral symmetry. Therefore we discuss fundamental symmetries of BdG Hamiltonian in this paragraph. The BdG Hamiltonian in momentum space is represented as

$$\check{H}_{\rm BdG}(\boldsymbol{k}) = \left[\begin{array}{cc} \hat{H}_{\rm N}(\boldsymbol{k}) & \hat{\Delta}(\boldsymbol{k}) \\ -\hat{\Delta}^*(-\boldsymbol{k}) & -\hat{H}^*_{\rm N}(-\boldsymbol{k}) \end{array} \right], \tag{2.3}$$

where $\hat{H}_{\rm N}(\boldsymbol{k})$ and $\hat{\Delta}(\boldsymbol{k})$ are the normal state Hamiltonian and the pair potential, respectively. [38] Throughput this chapter, symbols $\check{\cdot\cdot}$ and $\hat{\cdot\cdot}$ represent 4×4 and 2×2 matrices, respectively. The Hamiltonian for a p_x-wave superconductor in Eq. (A.2) preserves time-reversal symmetry,

$$\mathcal{T}_-\, \check{H}_{\rm BdG}\, \mathcal{T}_-^{-1} = \check{H}_{\rm BdG}, \quad \mathcal{T}_- = i\hat{\sigma}_2\, \mathcal{K}, \tag{2.4}$$

where $\mathcal{K}$ denotes taking the complex conjugation for Hamiltonian in real space, and taking the complex conjugation plus applying $\boldsymbol{k} \to -\boldsymbol{k}$ for Hamiltonian in momentum space. The Pauli's matrix in spin space is denoted by $\hat{\sigma}_j$ for $j = 1-3$. A BdG Hamiltonian always preserves particle-hole symmetry,

$$\mathcal{C}\, \check{H}_{\rm BdG}\, \mathcal{C}^{-1} = -\check{H}_{\rm BdG}, \quad \mathcal{C} = \hat{\tau}_1\, \mathcal{K}, \tag{2.5}$$

where $\hat{\tau}_j$ for $j = 1 - 3$ is the Pauli's matrix in particle-hole space. By combining the two symmetries, any Hamiltonian belonging to class DIII preserves a chiral symmetry

$$\left\{\check{\Gamma}_{\mathrm{DIII}},\, \check{H}_{\mathrm{BdG}}\right\} = 0, \quad \check{\Gamma}_{\mathrm{DIII}} = \hat{\tau}_1\, \hat{\sigma}_2. \tag{2.6}$$

Since $\check{\Gamma}^2_{\mathrm{DIII}} = 1$, the eigenvalue of the chiral operator is either 1 or -1. A ZES is always an eigenstate the chiral operator [13]. Indeed, it is easy to confirm that the Hamiltonian in Eq. (A.2) anticommutes to $\check{\Gamma}_{\mathrm{DIII}}$ and that the wave function of surface bound states at the zero energy $\phi_{p_x,\pm}$ in Eq. (A.5) is the eigenfunction of $\check{\Gamma}_{\mathrm{DIII}}$ belonging to the chial eigenvalue of ± 1. The index in Eq. (2.1) can be defined by

$$\mathcal{N}_{\mathrm{ZES}} \equiv N_+ - N_-, \tag{2.7}$$

where $N_\pm$ is the number of the ZESs belonging to the chiral eigenvalue of ± 1. The index is an invariant as long as the Hamiltonian preserves the chiral symmetry in Eq. (2.6). Thus $\mathcal{N}_{\mathrm{ZES}}$ calculated in a clean superconductor remains unchanged even in the presence of potential disorder because the random impurity potential $V_{\mathrm{imp}}(\boldsymbol{r})\, \hat{\tau}_3$ preservers the chiral symmetry in Eq. (2.6). The anomalous proximity effect happens when the index takes a nontrivial value $\mathcal{N}_{\mathrm{ZES}} \neq 0$. However, ZESs of H_{BdG} in class DIII always satisfy $\mathcal{N}_{\mathrm{ZES}} = 0$ in terms of their chiral eigenvalues of $\check{\Gamma}_{\mathrm{DIII}}$ [39]. Therefore, the BdG Hamiltonian of a superconductor exhibiting the anomalous proximity effect must satisfy following necessary conditions,

(i) H_{BdG} anticommutes to an extra chiral operator other than $\check{\Gamma}_{\mathrm{DIII}}$,

(ii) Zero-energy states at a surface of a superconductor have such a chiral property as $\mathcal{N}_{\mathrm{ZES}} \neq 0$ in terms of the extra chiral operator.

We show a simple way to find an extra chiral operator as follows. The Hamiltonian in Eq. (A.2) remains unchanged under the rotation around the first axis in spin space,

$$\check{R}_1\, \check{H}_{p_x}\, \check{R}_1^{-1} = \check{H}, \quad \check{R}_1 = \hat{\sigma}_1\, \hat{\tau}_3. \tag{2.8}$$

Using such a spin rotation symmetry it is possible to define a time-reversal like symmetry of Hamiltonian

$$\mathcal{T}_+\, \check{H}_{p_x}\, \mathcal{T}_+^{-1} = \check{H}_{p_x}, \quad \mathcal{T}_+ = \check{R}_1 \mathcal{T}_- = -\hat{\sigma}_3\, \hat{\tau}_3\, \mathcal{K}. \tag{2.9}$$

As a result of the spin-rotation symmetry of the Hamiltonian, we find

$$\{\check{\Gamma}_{\mathrm{BDI}},\, \check{H}_{p_x}\} = 0, \quad \check{\Gamma}_{\mathrm{BDI}} = i\mathcal{T}_+\, \mathcal{C} = \hat{\sigma}_3\, \hat{\tau}_2. \tag{2.10}$$

Since $\mathcal{T}_+^2 = 1$, $\check{H}_{p_x}$ belongs also to class BDI. The wave function of ZESs at a surface of a p_x-wave superconductor can be represented alternatively as $\phi_{p_x,\sigma}$ in Eq. (A.6). We find that $\phi_{p_x,\sigma}$ belongs to the positive chiral eigenvalues of $\check{\Gamma}_{\mathrm{BDI}}$ irrespective of σ. Therefore we find $N_+ = N_c$ and $N_- = 0$, which results in $\mathcal{N}_{\mathrm{ZES}} = N_c$. A p_x-wave superconductor satisfies the conditions (i) and (ii) in terms of the chiral operator $\check{\Gamma}_{\mathrm{BDI}}$. Two of authors showed that some superconductors under strong Zeeman field in the presence of spin-orbit interactions preserve such an extra chiral symmetry and host flat-band ZESs at their dirty surfaces. [39] The anomalous proximity effect has been considered to be a part of Majorana physics because such artificial superconductors host Majorana fermions at their surface. [40, 41] At present, however, we are thinking that a superconductor hosting Majorana fermions is a sufficient condition for the anomalous proximity effect. The necessary conditions (i) and (ii) are more relaxed than those generating Majorana fermions.

2.2.2 An odd-frequency s-wave pair

The anomalous proximity effect has two aspects: the penetration of a quasiparticle at the zero energy into a dirty metal as discussed in Sec. 2.2.1 and the penetration of an odd-frequency Cooper pair into a dirty metal. The existence of $\mathcal{N}_{\mathrm{ZES}}$-fold degenerate ZESs can be observed as a large zero-energy peak in the local density of states (LDOS) at a dirty metal. In the mean-field theory of superconductivity, the density of states can be calculated from the normal Green's function $\hat{G}$ and the pairing correlations are described by the anomalous Green's function $\hat{F}$. As the two Green's functions are related to each other through the Gor'kov equation, the enhancement of $\hat{G}$ at the zero energy causes an anomaly of $\hat{F}$ at the zero energy. The anomalous Green's function in Matsubara representation $\hat{F}(\boldsymbol{k}, i\omega_n)$ enables us to analyze symmetry of pairing correlations, where $\omega_n = (2n+1)\pi T$ is a fermionic Matsubara frequency and T is a temperature. The anomalous Green's function obeys the antisymmetric relation under the permutation of two electrons consisting of a Cooper pair,

$$\hat{F}^{\mathrm{T}}(-\boldsymbol{k}, -i\omega_n) = -\,\hat{F}(\boldsymbol{k}, i\omega_n), \tag{2.11}$$

where T means the transpose of a matrix. In the standard representation, the anomalous Green's function is decomposed into four spin components as

$$\hat{F}(\boldsymbol{k}, i\omega_n) = i\left[f_0(\boldsymbol{k}, i\omega_n) + \boldsymbol{f}(\boldsymbol{k}, i\omega_n)\cdot\hat{\boldsymbol{\sigma}}\right]\hat{\sigma}_2, \tag{2.12}$$

where f_0 is a spin-singlet component and $\boldsymbol{f}$ represents three spin-triplet components. In a dirty normal, the diffusive motion of a quasiparticle makes the Green's function be isotropic in momentum space as

$$\hat{F}(i\omega_n) = i\left[f_0(i\omega_n) + \boldsymbol{f}(i\omega_n)\cdot\hat{\boldsymbol{\sigma}}\right]\hat{\sigma}_2. \tag{2.13}$$

The relation in Eq. (2.11) implies that the spin-singlet component is an even function of ω_n as $f_0(-i\omega_n) = f_0(i\omega_n)$. The spin-triplet components, on the other hand, are odd function of ω_n as $\boldsymbol{f}(-i\omega_n) = -\boldsymbol{f}(i\omega_n)$. To compensate the anomaly of $\hat{G}$ at $\omega_n \to 0$, the anomalous Green's function must have a component of $\hat{F}(i\omega_n) \propto 1/\omega_n$. [42] Such an odd-frequency pair must be spin-triplet. Thus the last necessary condition for the anomalous proximity effect is

(iii) An odd-frequency spin-triplet s-wave pairing correlation $\boldsymbol{f} \propto 1/\omega_n$ exists at a surface as a result of the large zero-energy peak in the local density of states.

In a spin-singlet d_{xy}-wave superconductor, however, no spin-triplet pairing correlation exists in the absence of spin-dependent potentials.

2.3 d_{xy}-wave superconductor with spin-orbit interactions

2.3.1 Motivations

To make clear a motivation of this study, we show that a spin-singlet d_{xy}-wave superconductor without spin-orbit interaction does not cause the anomalous proximity effect. A spin-singlet d_{xy}-wave pair potential is defined by,

$$\hat{\Delta}(\boldsymbol{k}) = \Delta_{\boldsymbol{k}}\, i\hat{\sigma}_2, \quad \Delta_{\boldsymbol{k}} = \Delta\, \bar{k}_x \bar{k}_y, \tag{2.14}$$

where $k_x(k_y)$ is the wavenumber in the $x(y)$ direction. The wave numbers in the pair potential are normalized to the Fermi wavenumber k_F as $\bar{k}_x = k_x/k_F$ and $\bar{k}_y = k_y/k_F$. It is easy to confirm that the Hamiltonian for a d_{xy}-wave superconductor in Eq. (A.7) anticommutes to $\check{\Gamma}_{\mathrm{BDI}}$ and that the wave function of the ZESs at a surface of a d_{xy}-wave superconductor are given in Eq. (A.9). Their chiral eigenvalues depend on $\mathrm{sgn}(k_y)$ reflecting the sign change of the pair potential at $k_y = 0$. As displayed in Fig. A.1(b), the number of the ZESs at $k_y > 0$ is equal to that at $k_y < 0$. Although Eq. (A.7) satisfy condition (i), the index $\mathcal{N}_{\mathrm{ZES}}$ is always zero in the absence of spin-orbit interactions. Therefore, we concluded that random impurity potential completely lifts the high degeneracy at the zero energy in Fig. A.1(b) and that a d_{xy}-wave superconductor does not show the proximity effect in the absence of spin-dependent potentials.

In the presence of Rashba spin-orbit interaction in a d_{xy}-wave superconductor, numerical results of LDOS and those of the pairing correlation in a dirty metal indicate that condition (iii) may be satisfied [24]. The BdG Hamiltonian in momentum space reads,

$$\check{H}_0 =(\xi_{\boldsymbol{k}} - \lambda k_x \hat{\sigma}_2)\, \hat{\tau}_3 + \lambda k_y \hat{\sigma}_1 - \Delta_{\boldsymbol{k}} \hat{\tau}_2\, \hat{\sigma}_2, \tag{2.15}$$

where $\xi_{\boldsymbol{k}} = \boldsymbol{k}^2/2m - \epsilon_F$ is the kinetic energy of a quasiparticle measured from the Fermi energy $\epsilon_F = k_F^2/(2m)$ and λ represents the strength of the spin-orbit interaction. When the two spin-orbit interaction terms $-\lambda k_x \hat{\sigma}_2 \hat{\tau}_3$ and $\lambda k_y \hat{\sigma}_1$ coexist, $\check{\Gamma}_{\text{DIII}}$ is the only chiral operator anticommutes to $\check{H}_0$. Since $\mathcal{N}_{\text{ZES}} = 0$ in terms of the chiral eigenvalues of $\check{\Gamma}_{\text{DIII}}$, the degeneracy of the ZESs is fragile in the presence of potential disorder. [39] Thus we infer that the anomalous proximity effect in such junction would be very weak. Namely, the zero-bias conductance in an NS junction would not be quantized and the zero-energy peak in LDOS would disappear in the limit of strong potential disorder.

In such a situation, the goal of this chapter is to make clear roles of the spin-orbit interaction terms in the anomalous proximity effect. To achieve the objective, we analyze the chiral property of the surface bound states of two different superconductors: the Hamiltonian of one superconductor contains only a spin-orbit interaction $\lambda k_y \hat{\sigma}_1$ and that of the other contains only $-\lambda k_x \hat{\sigma}_2 \hat{\tau}_3$. After showing if $\mathcal{N}_{\text{ZES}}$ is 0 or not for the two superconductors, we make clear how an odd-frequency spin-triplet s-wave pair appears at a surface. On the basis of the obtained results, we provide a theoretical design of a superconductor that exhibits the strong anomalous proximity effect.

2.3.2 Surface bound states

We divide the Rashba spin-orbit interaction into two parts: $\lambda k_y \hat{\sigma}_1$ and $-\lambda k_x \hat{\sigma}_2 \hat{\tau}_3$ to study how they modify independently the chiral properties of zero-energy states and the symmetry of a Cooper pair at a surface. Fig. 2.1 shows the schematic pictures of a superconductor under consideration. A superconductor in Fig. 2.1(a) is infinitely long in the x direction and the width of the superconductor is W in the y direction. We apply the periodic boundary condition in the y direction. In what follows, we analyze the two BdG Hamiltonians given by

$$\check{H}_1 = \xi_{\boldsymbol{k}} \hat{\tau}_3 + \lambda k_y \hat{\sigma}_1 - \Delta_{\boldsymbol{k}} \hat{\tau}_2 \, \hat{\sigma}_2, \tag{2.16}$$

and

$$\check{H}_2 = \xi_{\boldsymbol{k}} \hat{\tau}_3 - \lambda k_x \hat{\sigma}_2 \hat{\tau}_3 - \Delta_{\boldsymbol{k}} \hat{\tau}_2 \, \hat{\sigma}_2. \tag{2.17}$$

We assume the relation

$$\Delta \ll \lambda k_F \ll \epsilon_F, \tag{2.18}$$

and discuss the effects of the spin-orbit interaction on the superconducting states within the first order of

$$\alpha \equiv \frac{\lambda k_F}{2\epsilon_F} \ll 1. \tag{2.19}$$

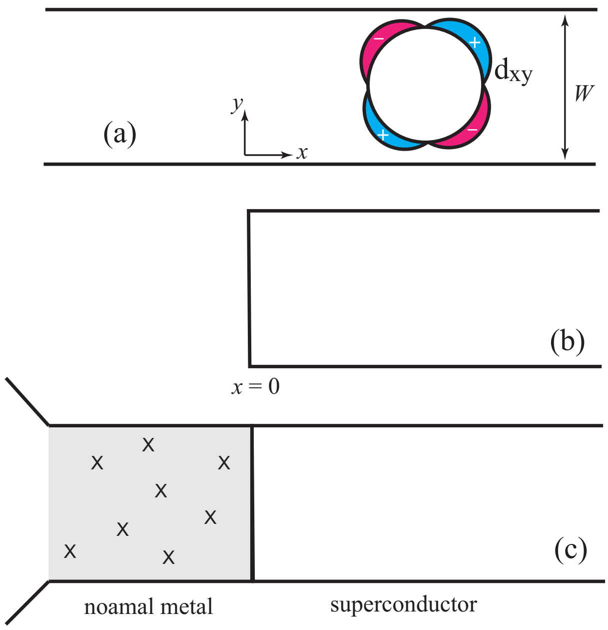

Figure 2.1: Schematic pictures of superconducting proximity structures. A spin-singlet d_{xy}-wave superconductor is infinitely long in the x direction in (a). The width of the superconductor is W in the y direction. The Green's function at a surface is calculated for a semi-infinite superconductor as shown in (b). We attach a normal metal to a superconductor at $x = 0$ in (c), where "cross" symbols represent impurities. A Cooper pair penetrates into the normal metal and causes the proximity effect.

The main purpose of the next two subsections are checking if the two Hamiltonian preserve extra chiral symmetry and calculating the index $\mathcal{N}_{\mathrm{ZES}}$. In addition, we also define the wave number on the Fermi surface and the number of the propagating channels N_c, which are necessary items to represent the anomalous Green's function.

We first focus on the $\check{H}_1$ in Eq. (2.16). The positive eigenvalues of $\check{H}_1$ are calculated to be

$$E_{1,\pm} = \sqrt{\xi_{1,\pm}^2 + \Delta_{\boldsymbol{k}}^2}, \quad \xi_{1,\pm}(k, k_y) = \xi_{\boldsymbol{k}} \pm \lambda\, k_y. \tag{2.20}$$

The two Fermi surfaces characterized by $\xi_{1,\pm} = 0$ are illustrated in Fig. 2.2(a). A wave number in the y direction k_y indicates a transport channel. As shown in Fig. 2.2(a), k_y axis are divided into three regions: (I) $-B_+ \leq k_y \leq -B_-$, (II) $-B_- \leq k_y \leq B_-$, and (III) $B_- \leq k_y \leq B_+$, with $B_\pm = [\sqrt{1+\alpha^2} \pm \alpha]k_F$. The wave numbers in the x direction are calculated as

$$p_{1\pm} \equiv \left[k_F^2 - k_y^2 \mp 2\alpha k_y k_F\right]^{1/2}, \tag{2.21}$$

as a function of k_y. A transport channel at k_y on the Fermi surface of $\pm$ branch is

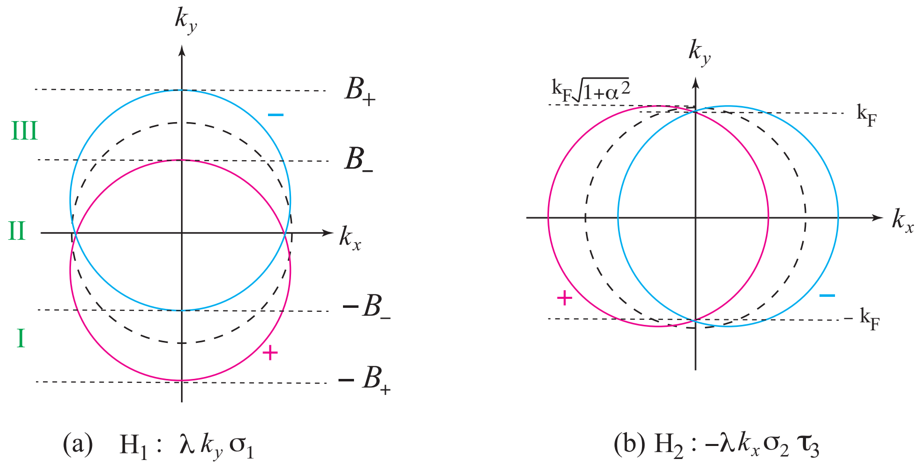

Figure 2.2: The two Fermi surfaces for H_1 and those for H_2 are illustrated in (a) and (b), respectively. In (a), the lower (upper) circle indicated by " + " (" − ") represents a Fermi surface calculated from $\xi_{1,+}(\boldsymbol{k}) = 0$ ($\xi_{1,-}(\boldsymbol{k}) = 0$). In (b), the left (right) circle represent a Fermi surface calculated from $\xi_{2,+}(\boldsymbol{k}) = 0$ ($\xi_{2,-}(\boldsymbol{k}) = 0$).

propagating for $p_{1\pm}^2 > 0$ and is evanescent for $p_{1\pm}^2 < 0$. Therefore,

$$n_+(k_y) \equiv \Theta(p_{1+}^2) + \Theta(p_{1-}^2), \tag{2.22}$$

represents the number of the propagating channels at k_y, where $\Theta(x)$ is the step function. We also define

$$n_-(k_y) \equiv \Theta(p_{1+}^2) - \Theta(p_{1-}^2), \tag{2.23}$$

for the latter use. In Figs. 2.3(a) and (b), we plot $n_\pm$ as a function of k_y. As shown in Fig 2.3(a), both $\pm$ branches are propagating in (II), whereas only one branch is propagating in (I) and (III). The number of propagating channels is calculated as

$$N_c \equiv \sum_{k_y} n_+(k_y) = \frac{W}{2\pi} \int_{-\infty}^{\infty} dk_y \, n_+(k_y), \tag{2.24}$$

$$= \left[\frac{2W k_F}{\pi} \right]_{\mathrm{G}}, \tag{2.25}$$

where $[\cdots]_{\mathrm{G}}$ is the Gauss's symbol meaning the integer part of the argument. Since a propagating channel hosts a ZES, the number of the ZESs at a surface is N_c. A superconductor described by H_1 hosts highly degenerate ZESs at its surface around $x \gtrsim 0$ in Fig. 2.1 (b). As shown in Fig. 2.3(b), n_- is an odd function of k_y. We use this property when we describe an induced pairing correlation by a spin-orbit interaction.

The wave functions of a surface bound states at the zero energy are described by

$$\psi_{1+}(x) = \begin{bmatrix} 1 \\ 1 \\ is_k \\ -is_k \end{bmatrix} e^{-q_x x} \sin p_{1+}x, \tag{2.26}$$

$$\psi_{1-}(x) = \begin{bmatrix} -1 \\ 1 \\ is_k \\ is_k \end{bmatrix} e^{-q_x x} \sin p_{1-}x, \tag{2.27}$$

$$s_k = \mathrm{sgn}(k_y). \tag{2.28}$$

Here the wavenumber in superconducting state is given approximately by

$$\left[p_{1s}^2 \pm 2m\Delta|\bar{p}_{1s}\bar{k}_y|\right]^{1/2} \approx p_{1s} \pm iq_x, \tag{2.29}$$

for $s = \pm$. The imaginary part of the wave number is estimated at $\epsilon = 0$ as $q_x = (\Delta/v_F)|\bar{k}_y|$ with $v_F = k_F/m$ being the Fermi velocity. As shown in Eqs. (2.26) and (2.27), q_x characterizes the spatial area of the surface bound states. The Hamiltonian Eq. (2.16) anticommutes to the extra chiral operator $\check{\Gamma}_{\mathrm{BDI}}$ in Eq. (2.10). It is easy to show

$$\check{\Gamma}_{\mathrm{BDI}}\, \psi_{1\pm} = g_\pm \psi_{1\pm}, \quad g_\pm = \pm s_k. \tag{2.30}$$

The chiral eigenvalues g_+, g_- and $g_+ + g_-$ are plotted as a function of k_y in Figs. 2.3(c), (d) and (e), respectively. By reflecting the sign change of the pair potential, both g_+ and g_- change their signs at $k_y = 0$ as shown in Figs. 2.3(c) and (d). The index in terms of the chiral eigenvalue of $\check{\Gamma}_{\mathrm{BDI}}$ can be calculated as

$$\mathcal{N}_{\mathrm{ZES}} = \sum_{k_y} [g_+ + g_-] = \left[-\frac{2Wk_F}{\pi}\alpha\right]_{\mathrm{G}}. \tag{2.31}$$

The index is a finite value in the presence of spin-orbit interaction. Thus, we conclude that $\check{H}_1$ satisfies necessary conditions (i) and (ii) in Sec. 2.2.1. The zero-bias conductance in a dirty NS junction in Fig. 2.1(c) can be quantized as Eq. (2.1). The shift of the Fermi surface by the spin-orbit interaction in Fig. 2.2 (a) makes the index be a nonzero value because the integrand of Eq. (2.31) is nonzero at (I) and (III). Therefore we will make clear what happen on the anomalous Green's function in these regions in Sec. 2.3.3.

Next, we focus on $\check{H}_2$ in Eq. (2.17). The positive eigenvalues of $\check{H}_2$ are calculated to be

$$E_{2,\pm} = \sqrt{\xi_{2,\pm}^2 + \Delta_{\boldsymbol{k}}^2}, \quad \xi_{2,\pm}(k, k_y) = \xi_{\boldsymbol{k}} \pm \lambda\, k. \tag{2.32}$$

In Fig. 2.2(b), we illustrate the two splitting Fermi surfaces characterized by $\xi_{2,\pm} = 0$. The wave numbers in the x direction on the Fermi surface are calculated as

$$p_{2\pm} = \sqrt{k_F^2 - k_y^2} \mp \alpha k_F. \tag{2.33}$$

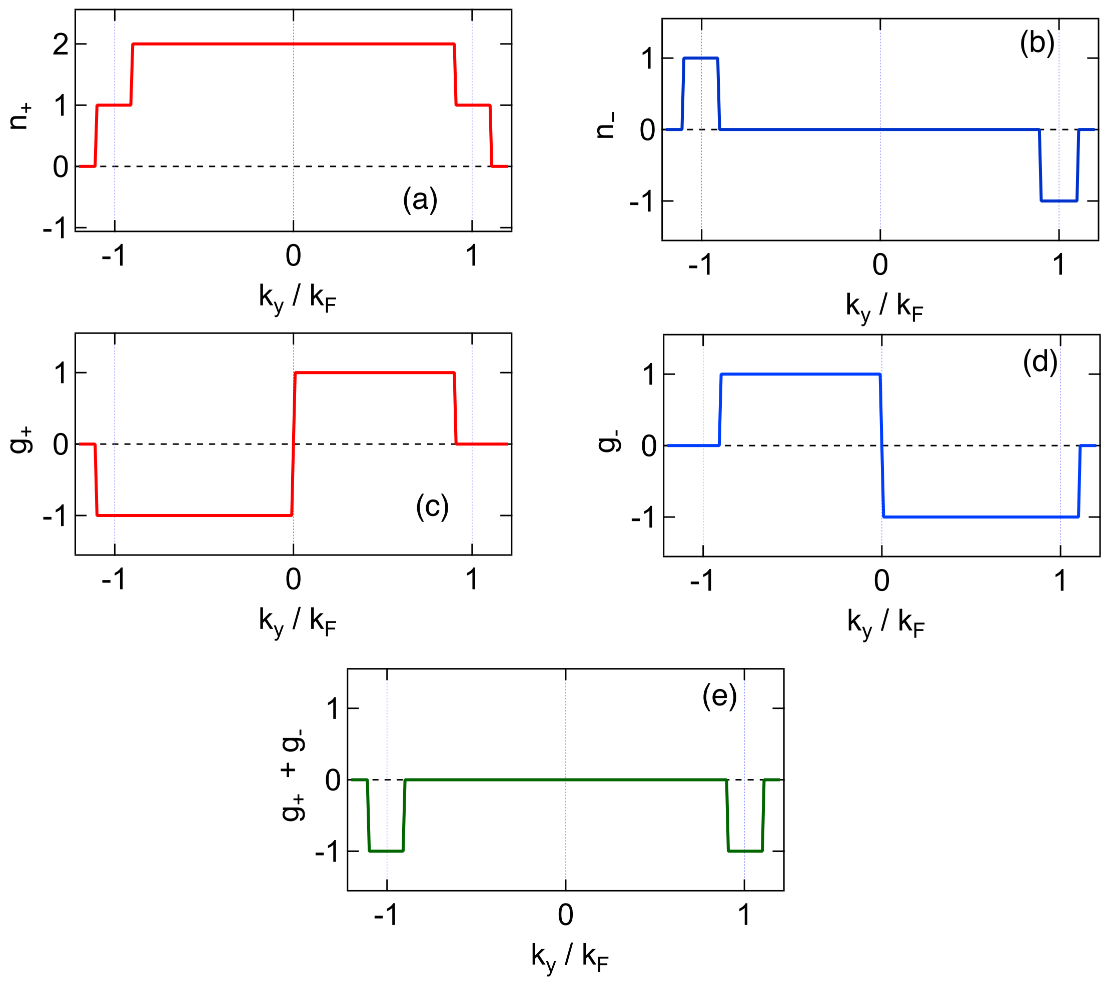

Figure 2.3: In (a), $n_+(k_y)$ represents the number of propagating channels at k_y. $n_-(k_y)$ in (b) is an odd function of k_y. The chiral eigenvalues of the ZESs g_+ and g_- are plotted in (c) and (d), respectively. In (e), the summation of the chiral eigenvalues $g_+ + g_-$ is shown. $n_-(k_y)$ in (b) and $g_+ + g_-$ in (e) are nonzero at (I) and (III).

For $|k_y| \leq k_F$, the transport channels are propagating. A topologically protected ZES appears for each propagating channel. The wave functions of such surface bound states are calculated as

$$\psi_{2+}(x) = \begin{bmatrix} s_k \\ -is_k \\ 1 \\ -i \end{bmatrix} e^{-q_x x} \sin p_{2+}x, \tag{2.34}$$

$$\psi_{2-}(x) = \begin{bmatrix} s_k \\ is_k \\ -1 \\ -i \end{bmatrix} e^{-q_x x} \sin p_{2-}x. \tag{2.35}$$

The Hamiltonian $\check{H}_2$ anticommutes to an extra chiral operator $\hat{\tau}_1$, which is derived from the invariance of $\check{H}_2$ under the rotation about the second axis in spin space $\hat{\sigma}_2\,\hat{\tau}_0$. It is easy to show that $\hat{\tau}_1\,\psi_{2\pm} = \pm s_k\,\phi_{2\pm}$. We find $\mathcal{N}_{\mathrm{ZES}} = 0$ because the chiral eigenvalues depend on $\mathrm{sgn}(k_y)$. Namely, $\check{H}_2$ does not satisfy necessary condition for the anomalous proximity effect (ii) in Sec. 2.2.1. Thus we conclude the a superconductor described by $\check{H}_2$ does not exhibit the anomalous proximity effect because the random impurity potential at its surface lifts the degeneracy at the zero energy.

2.3.3 Pairing correlations at a surface

The purpose of this section is to check a close relationship between conditions (ii) and (iii) discussed in Sec. 2.2. As $\check{H}_1$ satisfies condition (ii), an odd-frequency spin-triplet s-wave pairing correlation is expected to appear at a surface of a superconductor. We will make clear mechanisms of generating such an odd-frequency pair. As $\check{H}_2$ does not satisfy (ii), we will confirm that an odd-frequency spin-triplet s-wave pairing correlation is absent at its surface.

To this end, we calculate the Green's function at a surface of a superconductor as shown in Fig. 2.1(b). The outline of the derivation is as follows. We first solve the Gor'kov equation for the retarded Green's function,

$$\left[\epsilon + i\delta - \check{H}_{\mathrm{BdG}}(\boldsymbol{k})\right]\,\check{G}_\epsilon(\boldsymbol{k}) = \hat{\tau}_0\,\hat{\sigma}_0, \tag{2.36}$$

$$\check{G}_\epsilon(\boldsymbol{k}) = \begin{bmatrix} \hat{G}_\epsilon(\boldsymbol{k}) & \hat{F}_\epsilon(\boldsymbol{k}) \\ -\undertilde{\hat{F}}_\epsilon(\boldsymbol{k}) & -\undertilde{\hat{G}}_\epsilon(\boldsymbol{k}) \end{bmatrix} \tag{2.37}$$

where $i\delta$ is a small imaginary part of energy. The 'undertilded' function is defined by

$$\undertilde{X}_\epsilon(\boldsymbol{k}) \equiv X^*_{-\epsilon}(-\boldsymbol{k}), \tag{2.38}$$

where X is an arbitrary function. Secondly, we calculate the Green's function in real space,

$$\check{G}(\boldsymbol{r},\boldsymbol{r}') = \int_{-\infty}^{\infty} \frac{dk}{2\pi} e^{ik(x-x')} \sum_{k_y} \frac{e^{ik_y(y-y')}}{W} \check{G}(\boldsymbol{k}). \tag{2.39}$$

for an infinitely long superconductor in the x direction as shown in Fig. 2.1(a). Finally, we introduce a high potential barrier $V\delta(x)\,\hat{\tau}_3$ to divide the infinitely long superconductor into two semi-infinitely long superconductors. One of them is illustrated in Fig. 2.1(b). The Green's function at a surface $\check{G}^{\mathrm{S}}(\boldsymbol{r},\boldsymbol{r}')$ can be calculated by solving the Lippmann-Schwinger equation exactly as explained in Appendix C. The Green's function at a semi-infinite superconductor $\check{\mathbb{G}}$ is represented as

$$\check{\mathbb{G}}(\boldsymbol{r},\boldsymbol{r}') = \check{G}(\boldsymbol{r},\boldsymbol{r}') + \check{G}^{\mathrm{S}}(\boldsymbol{r},\boldsymbol{r}'). \tag{2.40}$$

In the text, we will show only the results of calculation and details of derivation are given in Appendix B.

We first study the pairing correlations at a surface of a superconductor described by $\check{H}_1$. The resulting anomalous Green's function at a surface is given by,

$$\begin{aligned}
\hat{F}^{\mathrm{S}}_{i\omega_n}(\boldsymbol{r},\boldsymbol{r}') =& \frac{1}{W} \sum_{k_y} \frac{e^{ik_y(y-y')}}{2\,v_F} e^{-q_x(x+x')} \left[\frac{i}{\Omega_n} \sin p_x(x-x')\,\Delta\,\bar{k}_y\,n_+(k_y) \right.\\
& - \frac{i}{\Omega_n} \sin p_x(x-x')\,\Delta\,\bar{k}_y\,n_-(k_y)\,\hat{\sigma}_1 \\
& + \frac{2}{\omega_n} \sin p_x x\,\sin p_x x'\,\Delta\,\bar{k}_y\,n_+(k_y) \\
& \left. -\frac{2}{\omega_n} \sin p_x x\,\sin p_x x'\,\Delta\,\bar{k}_y\,n_-(k_y)\,\hat{\sigma}_1 \right] i\hat{\sigma}_2,
\end{aligned} \tag{2.41}$$

where $\Omega_n = \sqrt{\omega_n^2 + \Delta_{\boldsymbol{k}}^2}$, $p_x = \sqrt{k_F^2 - k_y^2 + 2\alpha|k_y|k_F}$, and we applied the analytic continuation $\epsilon + i\delta \to i\omega_n$ to analyze the symmetry of pairing correlations. We use the standard expression in Eq. (2.12) to decompose the anomalous Green's function into four spin components. The first term in Eq. (2.41) represents spin-singlet d_{xy}-wave pairing correlation because it changes sign under $x \leftrightarrow x'$ and $y \leftrightarrow y'$ independently. Such pairing correlation is linked to the pair potential in the presence of attractive interactions between two electrons. The third term represents the pairing correlation belongs to an odd-frequency spin-singlet p_y-wave symmetry class. This correlation function changes the sign under $y \leftrightarrow y'$, whereas it preserves the sign under $x \leftrightarrow x'$. The spin-singlet d_{xy}-wave component in the anomalous Green's function is an odd function of $x-x'$, which is responsible for two phenomena at a surface: the appearance of highly degenerate bound states at the zero energy and the appearance of an odd-frequency p_y-wave pairing correlation. The first and the third terms in Eq. (2.41) exist even in the absence of spin-orbit interactions. The spin-orbit interaction in $\check{H}_1$ generates a spin-triplet p_x-wave symmetry at the second term from a spin-singlet d_{xy}-wave pairing correlation. It is easy to confirm that the second term remains unchanged under $y \leftrightarrow y'$ and changes its sign under $x \leftrightarrow x'$. In addition, the third term corresponds to an equal spin pairing correlation in the standard expression in Eq. (2.12). The anomalous Green's function in an infinitely long superconductor consists of two pairing correlations. One belongs to a spin-singlet d_{xy}-wave symmetry. The other belongs to a spin-triplet p_x-wave symmetry as shown in Eq. (B.19). Since the spin-triplet p_x-wave pairing correlation is also an odd function of $x - x'$, it induces a subdominant pairing correlation at a surface as shown in the last term of Eq. (2.41). The relation among the four components are illustrated schematically in Fig. 2.4(a). The last pairing correlation in Eq. (2.41) belongs to an odd-frequency spin-triplet s-wave symmetry. It is easy to check that this component does not change its sign in $x \leftrightarrow x'$ and $y \leftrightarrow y'$ independently. As shown in $n_-(k_y)$ in Fig. 2.3(b), this odd-frequency correlation is nonzero at region (I) and (III) in k_y. This property is closely related to the fact that $g_+ + g_-$ in Eq. (2.31) is a nonzero value of -1 at these regions as shown in Fig. 2.3(e). We conclude that spin-orbit interaction in $\check{H}_1$ generates an odd-frequency spin-triplet s-wave pairing correlation at a surface. Thus a superconductor described by $\check{H}_1$ satisfies also the last necessary condition (iii) for the anomalous proximity effect.

The local density of states at a surface is calculated from the normal Green's function as

$$N_{\mathrm{S}}(x,\epsilon) \equiv -\frac{1}{2\pi}\mathrm{Im}\int_{-W/2}^{W/2} dy \mathrm{Tr}\left[\check{G}_\epsilon^{\mathrm{S}}(\boldsymbol{r},\boldsymbol{r})\right]. \tag{2.42}$$

The calculated results of the normal Green's function at a surface is given by

$$\begin{aligned}\hat{G}_\epsilon^{\mathrm{S}}(\boldsymbol{r},\boldsymbol{r}') = \sum_{k_y} \frac{i\, e^{ik_y(y-y')} e^{-q_x(x+x')}}{2W v_{p_x}\Omega} \Big[&\epsilon \cos p_x(x+x') \\ &+ i\,\Omega\, \sin p_x(x+x') + 2\frac{\Delta_{\hat{\boldsymbol{k}}}^2}{\epsilon + i\delta}\, \sin p_x x\, \sin p_x x'\Big] \\ &\times \left[n_+(k_y) + n_-(k_y)\,\hat{\sigma}_1\right].\end{aligned} \tag{2.43}$$

The LDOS at a surface results in

$$\begin{aligned}N_{\mathrm{S}}(x,\epsilon) =&\delta(\epsilon)\sum_{k_y} \frac{2|\Delta_{\boldsymbol{k}}|}{v_{p_x}} \left\{\sin(p_x x)e^{-q_x x}\right\}^2 \\ &\times n_+(k_y),\end{aligned} \tag{2.44}$$

for $\epsilon \ll \Delta$. The local density of states at a surface has a peak at the zero energy, which reflects the presence of highly degenerate surface bound states at the zero energy. The appearance of an odd-frequency pairing correlation and that of surface bound states at the zero energy are linked to each other directly. Mathematically, $\epsilon + i\delta$ in the denominator of $\hat{G}^{\mathrm{S}}$ in Eq. (2.43) and ω_n in the denominator of the odd-frequency components of $\hat{F}^{\mathrm{S}}$ in Eq. (2.41) have the same origin within the analytic continuation $\epsilon + i\delta \to i\omega_n$. The transformation of

$$\frac{1}{\epsilon + i\delta} = \frac{P}{\epsilon} - i\pi\delta(\epsilon), \tag{2.45}$$

implies that the zero-energy peak in LDOS is a consequence of appearing an odd-frequency Cooper pair at a surface.

The Green's function of a superconductor described by $\check{H}_2$ is also calculated by solving the Lippmann-Schwinger equation. The anomalous Green's function at a surface results in

$$\begin{aligned} F^{\mathrm{S}}_{i\omega_n}(\boldsymbol{r}, \boldsymbol{r}') = & \frac{1}{W} \sum_{k_y} e^{ik_y(y-y')} \frac{e^{-q_x(x+x')}}{v_x} \\ & \times \left[i\,\frac{\Delta_{\boldsymbol{k}}}{\Omega_n} \sin k_x(x-x') + \frac{2}{\omega_n} \Delta_{\boldsymbol{k}} \sin k_x x \, \sin k_x x' \right. \\ & \left. + \frac{\alpha\,\Delta\,\bar{k}_y}{\Omega_n} \cos k_x(x-x')\,\hat{\sigma}_2 \right] i\,\hat{\sigma}_2. \end{aligned} \tag{2.46}$$

The first term belongs to spin-singlet d_{xy}-wave symmetry and is linked to the pair potential. The second term is induced at a surface and belongs to odd-frequency spin-singlet p_y-wave symmetry. Due to breaking local inversion symmetry at a surface, spin-singlet p_y-wave component is generated from spin-singlet d_{xy}-wave pairing correlation. As already discussed in Eq. (2.41), these two correlations exist in the absence of spin-orbit interactions. The spin-orbit interaction in $\check{H}_2$ generates a spin-triplet p_y-wave symmetry pairing correlation at the third term which changes sign under $y \leftrightarrow y'$ but retains its sign under $x \leftrightarrow x'$. The relations among the pairing correlations are illustrated in Fig. 2.4(b). In Eq (2.46), however, an odd-frequency spin-triplet s-wave correlation is absent as we expected at the beginning of this section. The usual proximity effect is also absent in a normal metal attached to a superconductor because all of the pairing correlations in Eq. (2.46) are odd functions of $y - y'$ [4, 27, 28]. Thus the spin-orbit interaction $\lambda k_x \hat{\sigma}_2\,\hat{\tau}_3$ does not contribute to the proximity effect.

2.4 Discussion

We have concluded that a superconductor described by $\check{H}_1$ in Eq. (2.16) satisfies all the necessary conditions for the anomalous proximity effect. On the other hand, a superconductor described by $\check{H}_2$ in Eq. (2.17) does not exhibit any type of proximity effect. Here we

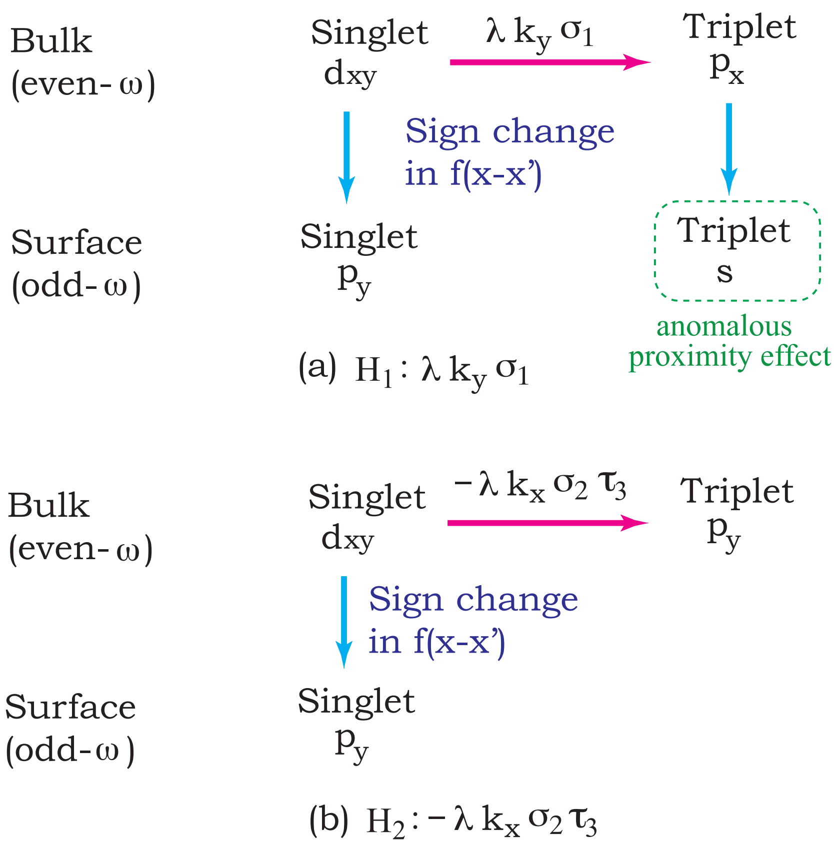

Figure 2.4: The pairing correlations appearing in a d_{xy}-wave superconductor. At a surface of d_{xy}-wave superconductor, an odd-frequency spin-singlet p_y-wave pairing correlation always appear as a result of the sign change in the d_{xy}-wave pairing correlation under $x \leftrightarrow x'$. In (a), a spin-orbit interaction $\lambda k_y \hat{\sigma}_1$ induces spin-triplet p_x-wave pairing correlation in bulk. An odd-frequency spin-triplet s-wave component appears at a surface as a result of the sign change of the p_x-wave pairing correlation. In (b), $-\lambda k_x \hat{\sigma}_2 \hat{\tau}_3$ induces spin-triplet p_y-wave pairing correlation in bulk while this interaction does not generate an odd-frequency spin-triplet s-wave correlation at a surface.

discuss briefly the proximity effect of a d_{xy}-wave superconductor where the two spin-orbit interaction terms coexist and form the Rashba spin-orbit interaction $\lambda k_y \hat{\sigma}_1 - \lambda k_x \hat{\sigma}_2 \hat{\tau}_3$. Unfortunately, the coexistence of the two interaction terms weakens the anomalous proximity effect seriously because the interaction $-\lambda k_x \hat{\sigma}_2 \hat{\tau}_3$ breaks the extra chiral symmetry of $\check{H}_1$. It is easy to confirm that $-\lambda k_x \hat{\sigma}_2 \hat{\tau}_3$ does not anticommute to Γ_{BDI}. Therefore, random impurity potential lifts the degeneracy at the zero energy. This explains why the signal of the anomalous proximity effect in Ref. [24] is very weak. Simultaneously, this discussion will determine the design guidelines for superconductors. We conclude that a d_{xy}-wave superconductor described by $\check{H}_1$ is necessary to observe the strong anomalous proximity effect such as the conductance quantization in a NS junction in Eq. (2.1) and the fractional current-phase relationship of the Josephson current in an SNS junction.

The control of spin-orbit interactions has been an important issue also in spintronics. The spin-orbit interaction in $\check{H}_1$ can be realized by tuning the Rashba spin-orbit interaction and the Dresselhaus spin-orbit interaction. It has been known that such type of interaction stabilizes a specialized spin configuration in momentum space called persistent spin helix. [43, 44, 45, 46, 47] Thus it would be possible to fabricate a superconductor exhibits the strong anomalous proximity effect by combining existing technologies. The anomalous proximity effect has been considered as a phenomenon unique to spin-triplet superconductors such as a p_x-wave superconductor in Eq. (A.2), a Majorana nanowire [11, 12, 20, 21], and two-dimensional artificial spin-triplet superconductors hosting flat-Majorana band at its surface [40, 41]. It is no doubt that the existence of spin-triplet order parameter (pair potential) is a sufficient condition for a superconductor exhibiting the anomalous proximity effect. On the other hand, we conclude that the necessary conditions discussed in Sec. 2.2 can be satisfied by a specific spin-triplet pairing correlation on a spin-singlet superconductor. Our results indicate a way of enriching the superconducting properties of high-T_c cuprate superconductors.

2.5 Summary

We theoretically studied the effects of spin-orbit interactions in a spin-singlet d_{xy}-wave superconductor on symmetry of the pairing correlations and those on chiral properties of the zero-energy bound states at a surface. The Hamiltonian for a d_{xy}-wave superconductor with a specific spin-orbit interaction preserves a chiral symmetry. The chiral property of the surface bound states is analyzed in terms of an index $\mathcal{N}_{\mathrm{ZES}}$ which is a measure of the strength of the anomalous proximity effect. Our results show that the spin-orbit interaction modifies the chiral property of the surface bound states drastically. As a result, $\mathcal{N}_{\mathrm{ZES}}$ can be nontrivial nonzero values. The symmetry of the pairing correlations at a surface of a superconductor are analyzed by using the anomalous Green's function which is obtained by solving the Gor'kov equation and the Lippmann-Schwinger equation analytically. The spin-orbit interactions induce spatially uniform spin-triplet p-wave pairing correlations in a d_{xy}-wave superconductor. A p-wave pairing correlation generates an odd-frequency spin-triplet s-wave Cooper pair at a surface of a d_{xy}-wave superconductor. We conclude that the presence of a spin-triplet pairing correlation causes the anomalous proximity effect even when a spin-triplet order parameter is absent.

To assist these conclusions, we should study low-energy transport properties through a dirty normal metal such as the conductance in a NS junction and the Josephson current in a SNS junction. The investigation by using numerical simulation is under way. Results will be presented in somewhere else.

Chapter 3

Theoretical model for an effective spin-triplet superconductor

Abstract

The proximity effect from a spin-triplet p_x-wave superconductor to a dirty normal-metal has been shown to result in various unusual electromagnetic properties, reflecting a co-operative relation between topologically protected zero-energy quasiparticles and odd-frequency Cooper pairs. However, because of a lack of candidate materials for spin-triplet p_x-wave superconductors, observing this effect has been difficult. In this chapter, we demonstrate that the anomalous proximity effect, which is essentially equivalent to that of a spin-triplet p_x-wave superconductor, can occur in a semiconductor/high-T_c cuprate superconductor hybrid device in which two potentials coexist: a spin-singlet d-wave pair potential and a spin–orbit coupling potential sustaining the persistent spin-helix state. As a result, we propose an alternative and promising route to observe the anomalous proximity effect related to the profound nature of topologically protected quasiparticles and odd-frequency Cooper pairs.

3.1 Introduction

When a superconductor (SC) is attached to a normal-metal, Cooper pairs (CPs) penetrate into the attached normal segment and modify the electromagnetic properties there. This phenomenon is known as the proximity effect and has been a central research subject in the field of superconductivity. When we consider a conventional spin-singlet s-wave SC, the attached normal-metal exhibits superconducting-like electromagnetic properties. However, the proximity effect from a spin-triplet p_x-wave SC to a dirty normal-metal (DN) has been shown to result in various counter-intuitive transport properties such as

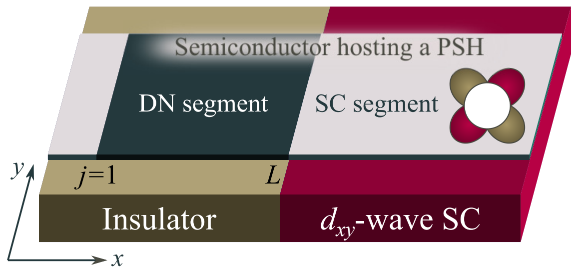

Figure 3.1: Schematic of an effective dirty normal-metal (DN)/d_{xy}-wave superconductor (SC) junction in the presence of a persistent spin helix (PSH).

the quantization of zero-bias conductance (ZBC) in DN/SC junctions [5, 48, 16, 14, 15] and the fractional current-phase relationship in Josephson currents of SC/DN/SC junctions [6, 49, 50]. Moreover, although the spin-triplet p_x-wave SC shows a diamagnetic response, the magnetic response in the attached DN is reversed to paramagnetic [51]. Such a drastic proximity effect of a spin-triplet p_x-wave SC has been referred to as an anomalous proximity effect (APE).

The APE of spin-triplet p_x-wave SCs has attracted intensive attention because its mechanism is related to two particles clad in novel concepts: a topologically-protected zero-energy quasiparticle and an odd-frequency CP. The zero-energy states (ZESs) originally located at a surface of a spin-triplet p_x-wave SC [52, 53, 54, 8, 13] can penetrate into the attached DN while retaining the high degree of degeneracy at zero-energy [5, 48, 55, 42, 56], where the robustness of the penetrated ZESs is ensured by topological protection [14, 15]. The unusual transport properties are a direct consequence of the resonant tunneling of quasiparticles via such topologically protected ZESs in the DN. Moreover, it has been shown that the ZESs penetrated from a spin-triplet p_x-wave are accompanied by odd-frequency CPs [55, 42, 56, 57, 23, 58], which are responsible for the paramagnetic response in the DN [51, 59, 60, 61, 25]. The APE is a remarkable phenomenon related to the intrinsic natures of topologically protected zero-energy quasiparticles and odd-frequency CPs. Thus, experimental observations of this effect are an important topic in the physics of superconductivity.

The main difficulty in observing the APE is a serious lack of candidate materials for spin-triplet p_x-wave SCs. Thus far, several theoretical models for effective p_x-wave SCs have been proposed, including models for semiconductor/s-wave SC hybrids under magnetic fields [40, 41, 39] and helical p-wave SCs (which are also rare) under magnetic fields [39, 62, 63]. However, experimentally realizing these models is also challenging because strong Zeeman potentials that exceed the superconducting pair potentials are needed to induce effective p_x-wave superconductivity. To resolve this stalemate, in this Letter, we explore an alternative route to observing the APE.

A central component of our scheme is to demonstrate the APE purely from *spin-singlet* SCs, whereas the spin-triplet p_x-wave SCs have been speculated to be critical for realizing the APE [5, 48, 55, 42, 56, 16, 14, 15, 6, 49, 50, 51]. Specifically, we demonstrate the APE in a two-dimensional (2D) semiconductor fabricated on an insulator/high-T_c cuprate SC junction, as shown in Fig. 3.1. We assume a proximity-induced spin-singlet d_{xy}-wave pair potential for the segment above the high-T_c cuprate SC. For the segment above the insulator, we assume a nonmagnetic disorder potential that can be introduced, for example, using a focused ion beam technique [64, 65]. Consequently, the 2D semiconductor becomes an effective DN/spin-singlet d_{xy}-wave SC junction. In addition, we assume that the semiconductor hosts a persistent spin helix (PSH) state, which has been studied intensively in the field of spintronics [43, 66, 47, 67]. As described in detail later, a spin–orbit coupling (SOC) potential sustaining the PSH induces a spin-triplet p_x-wave pairing *correlation* in the SC segment [24, 68], whereas the pairing *correlation* does not contribute to the superconducting *gap* directly. The induced spin-triplet p_x-wave pairing correlation in the SC segment is a source of robust odd-frequency spin-triplet s-wave pairing correlation in the attached DN segment. Moreover, on the basis of an Atiyah–Singer index theorem [14, 15, 39, 69], we will demonstrate the emergence of topologically-protected ZESs in the DN segment only in the presence of PSH. Remarkably, PSH states have been already realized in a number of experiments using semiconductor quantum well systems [44, 46, 45, 70]. Furthermore, it has been recently shown that the PSH is realized intrinsically in 2D ferroelectric materials such as group-IV monochalcogenide monolayers [71, 72, 73, 74, 75, 76, 77]. Thus, the recent rapid progress in the physics of the PSH provides a great potential for the realization of the proposed experimental setup. Consequently, we report a promising route to observing the APE.

3.2 Model

We describe the present system using a 2D tight-binding model. A lattice site is indicated by a vector $\boldsymbol{r} = j\boldsymbol{x} + m\boldsymbol{y}$, where $\boldsymbol{x}$ ($\boldsymbol{y}$) is a unit vector in the x (y) direction. The system comprises three segments: a semi-infinite lead wire (ballistic semiconductor segment) for $-\infty \leq j < 1$, a DN segment (dirty semiconductor segment) for $1 \leq j \leq L$, and a semi-infinite SC segment (ballistic semiconductor segment with a proximity-induced pair potential) for $L < j < \infty$. In the y direction, the number of lattice sites is given by W and a periodic boundary condition is applied. The Bogoliubov–de Gennes (BdG) Hamiltonian reads $H = H_{\mathrm{kin}} + H_{\mathrm{PSH}} + H_{\Delta} + H_{\mathrm{v}}$. The kinetic energy is given by

$$\begin{aligned} H_{\mathrm{kin}} =& -t \sum_{\langle \boldsymbol{r},\boldsymbol{r}' \rangle} \sum_{\sigma=\uparrow,\downarrow} (c^{\dagger}_{\boldsymbol{r},\sigma} c_{\boldsymbol{r}',\sigma} + c^{\dagger}_{\boldsymbol{r}',\sigma} c_{\boldsymbol{r},\sigma}) \\ &+ (4t-\mu) \sum_{\boldsymbol{r},\sigma} c^{\dagger}_{\boldsymbol{r},\sigma} c_{\boldsymbol{r},\sigma}, \end{aligned} \tag{3.1}$$

where $c^{\dagger}_{\boldsymbol{r},\sigma}$ ($c_{\boldsymbol{r},\sigma}$) is the creation (annihilation) operator for an electron at $\boldsymbol{r}$ with spin σ; t and μ denote the nearest-neighbor hopping integral and chemical potential, respectively. The PSH is characterized by a unidirectional SOC potential given by

$$H_{\mathrm{PSH}} = \frac{i\lambda}{2} \sum_{\boldsymbol{r},\sigma} s_{\sigma} (c^{\dagger}_{\boldsymbol{r}+\boldsymbol{y},\sigma} c_{\boldsymbol{r},\sigma} - c^{\dagger}_{\boldsymbol{r},\sigma} c_{\boldsymbol{r}+\boldsymbol{y},\sigma}), \tag{3.2}$$

where $s_{\uparrow(\downarrow)} = +1(-1)$. The SOC potential in Eq. (3.2) describes a Dresselhaus[110] SOC potential realized in zinc-blende III–V semiconductor quantum wells grown along the [110] direction [43, 66, 70]. The equivalent SOC potentials can also be obtained in quantum wells in which Rashba and Dresselhaus[100] SOC potentials have equal amplitudes [43, 66, 44, 46, 45] and in ferroelectric thin-film materials [71, 72, 73, 74, 75, 76, 77]. The proximity-induced spin-singlet d_{xy}-wave pair potential is given by

$$\begin{aligned} H_{\Delta} =& \frac{\Delta}{4} \sum_{j=L+1}^{\infty} \sum_{m=1}^{W} (c^{\dagger}_{\boldsymbol{r}+\boldsymbol{x}+\boldsymbol{y},\uparrow} c^{\dagger}_{\boldsymbol{r},\downarrow} + c^{\dagger}_{\boldsymbol{r},\uparrow} c^{\dagger}_{\boldsymbol{r}+\boldsymbol{x}+\boldsymbol{y},\downarrow} \\ &- c^{\dagger}_{\boldsymbol{r}+\boldsymbol{x}-\boldsymbol{y},\uparrow} c^{\dagger}_{\boldsymbol{r},\downarrow} - c^{\dagger}_{\boldsymbol{r},\uparrow} c^{\dagger}_{\boldsymbol{r}+\boldsymbol{x}-\boldsymbol{y},\downarrow}) + \mathrm{H.c.}, \end{aligned} \tag{3.3}$$

where Δ denotes the amplitude of the pair potential. The disorder potential in the DN segment is described by

$$H_{v} = \sum_{j=1}^{L} \sum_{m=1}^{W} \sum_{\sigma} v(\boldsymbol{r}) c^{\dagger}_{\boldsymbol{r},\sigma} c_{\boldsymbol{r},\sigma}, \tag{3.4}$$

where $v(\boldsymbol{r})$ is given randomly in the range $-X \leq v(\boldsymbol{r}) \leq X$.

In the following numerical calculations, we fix the parameters as $\mu = t$, $\lambda = 0.5t$, $\Delta = 0.1t$, $L = 50$, and $W = 50$. For simplicity, we assume that t, μ, and λ are uniform in the entire system. For the ensemble average, 500 samples are used. To observe the APE experimentally, the thermal coherence length $\xi_T = \sqrt{\hbar D/2\pi k_B T}$ must be longer than the length of the DN segment, where T and D represent the temperature and the diffusion constant in the DN segment, respectively. For simplicity, we assume zero temperature in the following calculations.

3.3 Results

3.3.1 Zero-bias conductance

We first focus on the differential conductance in the present device. Within the Blonder–Tinkham–Klapwijk formalism [78, 79, 7], the differential conductance is calculated by

$$G_{\mathrm{NS}}(eV) = \frac{e^2}{h}\sum_{\zeta,\zeta'}\left[\delta_{\zeta,\zeta'} - \left|r^{ee}_{\zeta,\zeta'}\right|^2 + \left|r^{he}_{\zeta,\zeta'}\right|^2\right]_{E=eV}, \tag{3.5}$$

where $r^{ee}_{\zeta,\zeta'}$ and $r^{he}_{\zeta,\zeta'}$ denote a normal and an Andreev reflection coefficient at energy E, respectively. The indexes ζ and ζ' label an outgoing and incoming channel in the lead wire, respectively. These reflection coefficients are calculated using recursive Green's function techniques [**?** 80]. In Fig. 3.2(a), we show the ZBC, i.e., $G_{\mathrm{NS}}(eV = 0)$ as a function of the normal resistance $R_N = G_{\mathrm{N}}^{-1}(eV = 0)$, where the normal conductance $G_{\mathrm{N}}(eV)$ is calculated by setting $\Delta = 0$. We vary the value of R_N by changing the magnitude of the disorder potential, X. The dotted black line denotes the result corresponding to the absence of the PSH (i.e., λ=0). In this case, the ZBC decreases to zero with increasing resistance in the normal segment R_N. Nevertheless, as shown by the solid red line, the ZBC in the presence of the PSH shows saturation with increasing resistance and shows a quantization in the dirty limit as

$$\lim_{R_N\to\infty} G_{\mathrm{NS}}(eV = 0) = \frac{2e^2}{h}|\mathbb{Z}|, \tag{3.6}$$

where $|\mathbb{Z}| = 6$ in the case of the present parameters. In Fig. 3.2(b), we also show G_{NS} at $R_N = 0.55(h/e^2)$ as a function of the bias voltage. The results clearly show that only the conductance spectrum in the presence of the PSH exhibits a sharp ZBC peak. The quantization of the ZBC in the dirty limit is a representative manifestation of the APE [5, 48, 14, 15]. The integer number of $\mathbb{Z}$, which characterizes the strength of the APE, will later be derived analytically. We now discuss the local density of states (LDOS) in the DN segment. The LDOS averaged over the lattice sites in the y direction is calculated by

$$\rho_{\mathrm{NS}}(j, E) = -\frac{1}{\pi W}\sum_{m=1}^{W} \mathrm{Tr}\left[\mathrm{Im}\left\{\check{G}(\boldsymbol{r}, \boldsymbol{r}, E + i\delta)\right\}\right], \tag{3.7}$$

where $\check{G}(\boldsymbol{r}, \boldsymbol{r}', E)$ represents the Green's function, δ is a small imaginary component added to the energy, E, and Tr denotes the trace in spin and Nambu spaces. Fig. 3.3(a) shows $\rho_{\mathrm{NS}}(j, E)$ at the center of the DN segment (i.e., $j = L/2$) as a function of the energy. We chose $X = 2t$ and $\delta = 10^{-4}\Delta$. The result is normalized by the LDOS in the normal states ρ_N calculated by setting $\Delta = 0$. When the PSH is present, the LDOS exhibits a sharp zero-energy peak (solid red line), whereas the peak is not observed when the PSH is absent

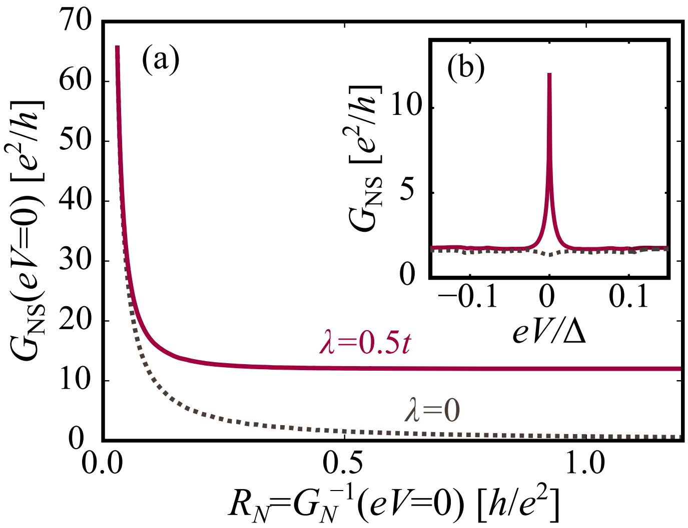

Figure 3.2: (a) ZBC as a function of the normal resistance R_N. (b) Differential conductance at $R_N = 0.55(h/e^2)$ as a function of the bias voltage. The solid red (dotted black) line denotes the result corresponding to the presence (absence) of the PSH with $\lambda = 0.5t$ ($\lambda = 0$).

(dotted black line). The zero-energy peak in the LDOS suggests that ZESs originally located at the junction interface penetrate into the DN segment, which is responsible for the quantization of the conductance minimum in Eq. (3.6) [5, 48, 14, 15].

Here, we discuss the odd-frequency CPs in the DN segment. SOC potentials have been shown to induce spin-triplet pairing correlations in spin-singlet SCs [24, 68], whereas the pairing correlation does not contribute to the superconducting gap directly. According to the analysis in Ref. [68], the SOC potential in Eq. (3.2), which sustains the PSH, generates an even-frequency spin-triplet p_x-wave correlation in the spin-singlet d_{xy}-wave SC. Therefore, as in the case of pure DN/p_x-wave SC junctions [58, 68], we can reasonably expect that the even-frequency spin-triplet p_x-wave pairing correlations induced in the SC segment can function as the source of odd-frequency spin-triplet s-wave correlations in the attached DN segment. We here focus only on the odd-frequency spin-triplet s-wave CPs, whose pair amplitude is evaluated by

$$F^{\rm odd}_{S_z=0}(j,\omega) = \frac{1}{\sqrt{2}W} \sum_{m=1}^{W} [F^{\rm odd}_{\uparrow,\downarrow}(\boldsymbol{r},\omega) + F^{\rm odd}_{\downarrow,\uparrow}(\boldsymbol{r},\omega)], \tag{3.8}$$

$$F^{\rm odd}_{\sigma,\sigma'}(\boldsymbol{r},\omega) = [F_{\sigma,\sigma'}(\boldsymbol{r},\boldsymbol{r},\omega) - F_{\sigma,\sigma'}(\boldsymbol{r},\boldsymbol{r},-\omega)]/2, \tag{3.9}$$

where $F_{\sigma,\sigma'}(\boldsymbol{r},\boldsymbol{r}',\omega)$ represents the anomalous part of the Matsubara Green's function. We also confirm that other components of the odd-frequency spin-triplet s-wave CPs,

$$F^{\rm odd}_{S_z=1(-1)}(j,\omega) = \sum_{m} F^{\rm odd}_{\uparrow,\uparrow(\downarrow,\downarrow)}(\boldsymbol{r},\omega)/W,$$

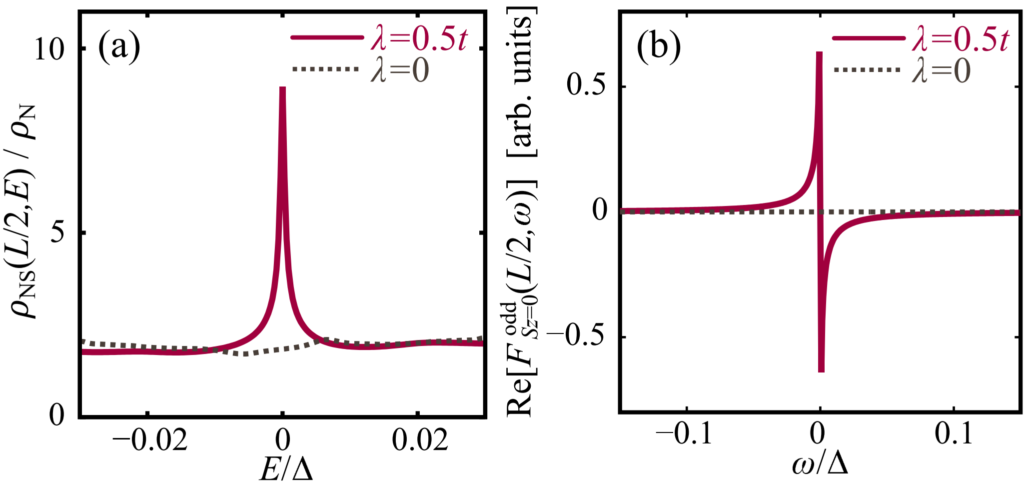

Figure 3.3: (a) LDOS at the center of the DN segment as a function of the energy. (b) Pair amplitudes for the odd-frequency spin-singlet s-wave component at the center of the DN segment as a function of the Matsubara frequency.

are absent in the present junction. Fig. 3.3(b), shows the real part of $F^{\mathrm{odd}}_{S_z=0}$ at the center of the DN segment as a function of the Matsubara frequency ω, where the imaginary part of $F^{\mathrm{odd}}_{S_z=0}$ is also found to be zero identically. As expected, $F^{\mathrm{odd}}_{S_z=0}$ in the DN segment becomes finite in the presence of the PSH (solid red line), whereas in the absence of the PSH (dotted black line), $F^{\mathrm{odd}}_{S_z=0} = 0$. As a result, we confirm the formation of the odd-frequency spin-triplet s-wave CPs in the DN, which is an important aspect of the APE.

3.3.2 Index theorem

We here discuss an Atiyah–Singer index theorem that characterizes the APE in the present junction. To evaluate the topological property of the SC segment, we remove the DN segment from the system and apply a periodic boundary in the x direction. Moreover, for simplicity, we describe the present SC in continuous space. Consequently, the BdG Hamiltonian in momentum space is given by

$$H(\boldsymbol{k}) = \xi(\boldsymbol{k})\sigma_0\tau_z + \lambda k_y \hat{\sigma}_z \tau_0 - \Delta(\boldsymbol{k})\sigma_y\tau_y, \tag{3.10}$$

where $\xi(\boldsymbol{k}) = (\hbar^2 k^2/2m) - \mu$ with m representing the effective mass of an electron, $\Delta(\boldsymbol{k}) = \Delta(k_x k_y/k_F^2)$ with $k_F = \sqrt{2m\mu}/\hbar$ representing the Fermi wavenumber, σ_α (τ_α) for $\alpha = x, y, z$ are the Pauli matrices acting on spin (Nambu) space, and σ_0 (τ_0) is the unit matrix in spin (Nambu) space. The BdG Hamiltonian $H(\boldsymbol{k})$ intrinsically preserves particle–hole symmetry as $CH(\boldsymbol{k})C^{-1} = -H(-\boldsymbol{k})$, where $C = \tau_x\mathcal{K}$ with $\mathcal{K}$ representing the complex conjugation operator. We also find time-reversal symmetry as $T_- H(\boldsymbol{k}) T_-^{-1} = H(-\boldsymbol{k})$ with

$T_- = i\sigma_y\tau_0\mathcal{K}$. Because $C^2 = +1$ and $T_-^2 = -1$, the BdG Hamiltonian belongs to the DIII symmetry class [81]. Importantly, because of the nature of the PSH [43], the BdG Hamiltonian preserves spin-rotation symmetry along the z axis even in the presence of the SOC potential: $R_z H(\boldsymbol{k}) R_z^{-1} = H(\boldsymbol{k})$ with $R_z = \sigma_z\tau_z$. By combining T_- and R_z, we obtain $T_+ H(\boldsymbol{k}) T_+^{-1} = H(-\boldsymbol{k})$, where $T_+ = R_z T_-$ represents an additional time-reversal symmetry obeying $T_+^2 = +1$. Because $C^2 = +1$ and $T_+^2 = +1$, we find that $H(\boldsymbol{k})$ can be simultaneously classified into the BDI symmetry class [81]. The energy spectrum of $H(\boldsymbol{k})$ is given by $E_{s_\sigma}(\boldsymbol{k}) = \pm\sqrt{\{\xi(\boldsymbol{k}) + s_\sigma \lambda k_y\}^2 + \Delta^2(\boldsymbol{k})}$. The branch of $E_{s_\sigma}(\boldsymbol{k})$ exhibits four superconducting gap nodes at $(k_x, k_y) = (\pm k_F, 0)$ and $(0, \pm k_\lambda - s_\sigma \bar{\lambda})$, where

$$k_\lambda = \sqrt{k_F^2 + \bar{\lambda}^2}, \quad \bar{\lambda} = m\lambda/\hbar^2. \tag{3.11}$$

On the basis of the Atiyah–Singer index theorem [14, 15, 39, 69], a topological index that characterizes the number of zero-energy states at a *dirty* surface of a nodal SC is given by

$$\mathbb{Z} = \sum_{k_y}{}' w_{\mathrm{BDI}}(k_y), \tag{3.12}$$

$$w_{\mathrm{BDI}}(k_y) = \frac{i}{4\pi}\int dk_x \mathrm{Tr}[S_+ \{H(\boldsymbol{k})\}^{-1} \partial_{k_x} H(\boldsymbol{k})], \tag{3.13}$$

where $S_+ = iT_+C = -\sigma_x\tau_y$ represents the chiral symmetry operator with respect to the BDI symmetry class and $\sum'_{k_y}$ denotes a summation over k_y excluding the nodal points. Using Eq. (3.13), we obtain

$$w_{\mathrm{BDI}}(k_y) = \begin{cases} 1 & \text{for} \quad k_\lambda - \bar{\lambda} < |k_y| < k_\lambda + \bar{\lambda} \\ 0 & \text{otherwise} \end{cases}, \tag{3.14}$$

and therefore $\mathbb{Z} = \sum_{k_\lambda - \bar{\lambda} < |k_y| < k_\lambda + \bar{\lambda}}$. When the momentum k_y is assumed to be a continuous variable, the discrete summation of k_y is replaced with the integration as

$$\sum_{k_y} \to \frac{W}{2\pi}\int dk_y. \tag{3.15}$$

Using Eq. (3.15), we obtain

$$\mathbb{Z} = [(\lambda k_F/2\mu) N_c]_{\mathrm{G}}, \tag{3.16}$$

where $[\cdots]_{\mathrm{G}}$ is the Gauss symbol giving the integer part of the argument, and $N_c = 2Wk_F/\pi$, where $[N_c]_{\mathrm{G}}$ represents the number of propagating channels. The index $\mathbb{Z}$ becomes finite only in the presence of the PSH ($\lambda \neq 0$). According to the Atiyah–Singer index theorem [14, 15, 39, 69], the $|\mathbb{Z}|$ ZESs can robustly remain at zero-energy even in the presence of potential disorders; they can therefore penetrate into the attached DN while retaining their $|\mathbb{Z}|$-fold degeneracy [14, 15]. In the presence of the chiral symmetry of S_+, each ZES can form a perfect Andreev reflection channel at zero-energy [15, 82], which explains the ZBC quantization in Eq. (3.6).

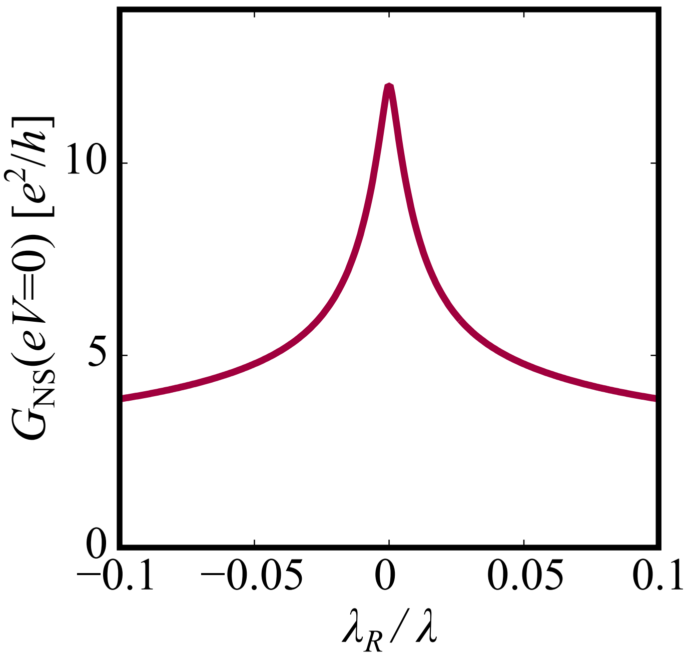

Figure 3.4: ZBC as a function of the strength of the Rashba SOC potential. We chose $X = 2t$.

We here note that the number of stable ZESs in typical *fully gapped* topological SCs is limited to a few. However, the present hybrid system can host the ZESs with a high degree of degeneracy at zero-energy. For instance, when we assume that $\mu = 2$meV, $\lambda = 10$meVnm, and $m = 0.07m_e$, where m_e is the electron rest mass, we obtain $\mathbb{Z} \approx [0.128N_c]_{\mathrm{G}}$, which means that approximately 10% of the propagating channels contribute to the resonant transmission. We can therefore reasonably expect a drastic signature of the APE, which should be easily detectable in experiments.

3.4 Discussion

We briefly discuss an effect of a perturbative Rashba SOC potential described by $H_R(\boldsymbol{k}) = \lambda_R(k_y\sigma_x\tau_0 - k_x\sigma_y\tau_z)$. Because the Rashba SOC breaks the chiral symmetry of S_+, the index $\mathbb{Z}$ in Eq. (3.12) can no longer be defined. Therefore, in the presence of Rashba SOC, the ZESs cannot retain their high degree of degeneracy at zero-energy. Fig. 3.4 shows the ZBC as a function of the strength of the Rashba SOC λ_R. The ZBC is substantially increased in the vicinity of the PSH state (i.e., $\lambda_R = 0$). In principle, the amplitude of Rashba SOC potentials can be tuned experimentally by applying gate voltages or pressures. Therefore, in experiments, a sudden enhancement in the ZBC as the strength of the Rashba SOC is varied is a possible observable signature of the APE.

In summary, we demonstrate that a spin-singlet d_{xy}-wave SC in the presence of PSH exhibits the APE. The proposed experimental setup can be fabricated by interfacing existing materials. Our proposal therefore represents a promising approach to observing the APE.

Chapter **4**

Anomalous proximity effect in a spin-singlet superconductor without surface Andreev bound states

Abstract

The anomalous proximity effect of a spin-triplet p-wave superconductor has been known as a part of the Majorana Physics. We demonstrate that a spin-singlet d-wave superconductor exhibits the anomalous proximity effect when a special type of the spin-orbit interaction works in the superconductor. The results show the quantization of the zero-bias conductance in a dirty normal-metal/superconductor junction. We also discuss a relation between our findings and recent experimental results on a $CoSi_2/TiSi_2$ junction.

4.1 Introduction

When a superconductor (SC) is attached to a normal metal, Cooper pairs penetrate from the SC into the normal metal and modify its electromagnetic and thermal properties. This phenomenon, known as the proximity effect, exhibits distinct behavior depending on the symmetry of the pair potential. Specifically, the proximity effect of a spin-triplet p-wave SC indicates remarkable transport phenomena such as the quantization of zero-bias conductance in a dirty normal-metal / superconductor (DN/SC) junction [5, 48] and the fractional current-phase relationship of a Josephson currents in a SC/DN/SC junction [6, 49]. These unusual phenomena are referred to as anomalous proximity effect (APE).

The APE is a result of the interplay between two interference effects: the proximity effect in a DN attached to a SC and the formation of Andreev bound states at the surface of a SC. The presence or absence of the proximity in a DN depends sensitively on the symmetry of the pair potential [83]. To host Andreev bound states at the surface of a SC, the pair potential is necessary to chenge its sign on the Fermi surface [52, 53, 7, 8]. Symmetry analysis in the early stages of the study suggested that the APE is a phenomenon unique to spin-triplet SCs. [49] In addition to the conductance quantization in a DN/SC junction, the APE causes the zero-bias anomaly of the conductance spectra in a T-shaped junction [16], and the unusual surface impedance [51]. Unfortunately, it would be very difficult to observe the APEs in experiments because spin-triplet SCs are very rare. A topological material based compound $Cu_xBi_2Se_3$ and several uranium compounds such as UPt_3, UBe_{13}, UGe_2, and UTe_2 are candidates of the spin-triplet SC [84, 85, 86, 87, 88, 89, 90]. However, spin-triplet superconductivity in these materials are still under debate.

The fabrication of artificial spin-triplet SCs is an important issue these days to realize the quantum computation by applying non-Abelian statistics of Majorana Fermions. [11, 12, 20, 21, 23, 91]. The APE is a part of the Majorana physics because Majorana zero modes are a special case of the Andreev bound states at the surface of a spin-triplet SC [23]. These theoretical studies have suggested that spin-orbit interactions (SOIs) enable the realization of spin-triplet superconductivity in a spin-singlet SC. Moreover, a theory shows that a nonzero invariant $\mathcal{N}_{\mathrm{ZES}}$, mathematically known as an Atiyah-Singer index, represents exactly the quantized value of the zero-bias conductance in a DN/SC junction [14, 15]. Namely, $\mathcal{N}_{\mathrm{ZES}}$ represents the number of zero-energy states that penetrates from a surface of SC into a DN and form the resonant transmission channels. Therefore, a superconducting state described by the Bogoliubov de Gennes (BdG) Hamiltonian leading to $\mathcal{N}_{\mathrm{ZES}} \neq 0$ causes the APE. The conclusions of these theories lead us to infer that spin-triplet superconductivity is only a sufficient condition for $\mathcal{N}_{\mathrm{ZES}} \neq 0$. Two of authors looked for necessary conditions for the BdG Hamiltonian that provide a nonzero index [39]. We found that several Hamiltonians breaking time-reversal symmetry describe the artificial SCs hosting Majorana zero modes [40, 41, 39]. In addition, we also found that a Hamiltonian for a spin-singlet d_{xy}-wave SC with a specialized SOI gives a nonzero index. [68, 92] It has been well established that a d_{xy}-wave SC without SOIs hosts highly degenerate zero-energy states at its clean surface parallel to the y direction [52, 53, 7, 8]. But in the absense of SOIs, $\mathcal{N}_{\mathrm{ZES}} = 0$ holds true, which means that zero-energy states are fragile under impurity scatterings. A SOI changes such fragile zero-energy states to robust zero-energy states. [68, 92]

In 2021, an experiment observed a clear signal of APE [17]. The conductance spectra in a T-shaped junction connecting to $CoSi_2$ grown on a Si substrate show the zero-bias anomaly which is a typical phenomenon of the APE. [16] Their analysis of weak-antilocalization magnetoresistance allowed them to extract the spin-orbit scattering time, from which they inferred a spin-orbit interaction energy roughly 20 times larger than the superconducting gap energy. However, spin-singlet s-wave superconductivity has been well-established in bulk $CoSi_2$ [93, 94]. Unlike a d_{xy}-wave SC, the zero-energy states are absent at the junction interface. At present, it is not clear if SOIs can cause the APE in a junction that consists a spin-singlet SC without any surface Andreev bound states. We discuss this issue in the present chapter.

In this chapter, we theoretically study the differential conductance in a DN/SC junction as shown in Fig. 4.1. We assume the spin-singlet s-wave and spin-singlet $d_{x^2-y^2}$-wave pair potentials in a SC. In the absence of SOIs, the Andreev bound states are absent at an interface of a junction consisting of such superconductors. We introduce three types of SOIs in a SC and the nonmagnetic random impurity potential in a DN. The conductance is calculated based on the Blonder-Tinkham-Klapwijk formula and the transport coefficients are obtained by using the recursive Green's function method. A $d_{x^2-y^2}$-wave SC with a spin-helix type SOI causes the APE. Unfortunately, an s-wave SC does not exhibit the APE with any types of SOIs.

This chapter is organized as follows. We explain our theoretical model in Sec. 4.2. The results of the differential conductance are presented in Sec. 4.3. We explain why spin-helix type SOI is necessary for the APE and why an s-wave SC does not indicate APE in Sec. 4.4. The discussion of our results is presented in Sec.4.5. The conclusion is given in Sec. 4.6. In Appendix, we discuss important roles of chiral symmetry in the APE.

4.2 Model

We describe a DN/SC junction on a two-dimensional tight-binding lattice as shown in Fig. 4.1, where L is the length of a DN, W is the width of a junction, $\boldsymbol{x}(\boldsymbol{y})$ is the unit vector in the $x(y)$ direction, and a vector $\boldsymbol{r} = j\boldsymbol{x} + m\boldsymbol{y}$ indicates a lattice site. The Hamiltonian consists of four terms,

$$H = H_{\mathrm{kin}} + H_{\mathrm{imp}} + H_{\mathrm{SOI}} + H_{\Delta} \tag{4.1}$$

The kinetic energy of an electron is represented by

$$\begin{aligned} H_{\mathrm{kin}} = &- t \sum_{\boldsymbol{r},\boldsymbol{r'}} \sum_{\alpha=\uparrow,\downarrow} \left(c^{\dagger}_{\boldsymbol{r},\alpha} c_{\boldsymbol{r'},\alpha} + c^{\dagger}_{\boldsymbol{r'},\alpha} c_{\boldsymbol{r},\alpha} \right) \\ &+ (4t - \mu) \sum_{\boldsymbol{r},\alpha} c^{\dagger}_{\boldsymbol{r},\alpha} c_{\boldsymbol{r},\alpha}, \end{aligned} \tag{4.2}$$

where t is the nearest-neighbor hopping integral, μ is the chemical potential, and $c^{\dagger}_{\boldsymbol{r},\alpha}(c_{\boldsymbol{r},\alpha})$ is the creation (annihilation) operator of an electron with spin α at $\boldsymbol{r}$. The second term

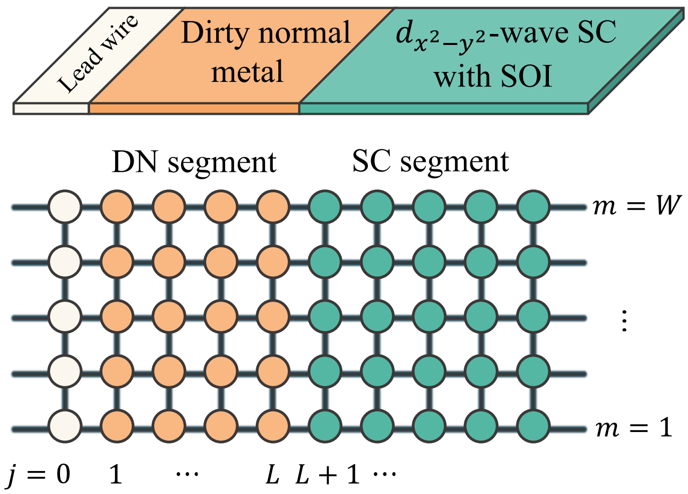

Figure 4.1: Schematic figure of a two-dimensional dirty normal-metal / SC junction below. We consider spin-singlet pair potentials (s-wave or $d_{x^2-y^2}$-wave) and three types of spin-orbit interactions in a SC. We also introduce nonmagnetic random impurities in a normal metal near the junction interface.

represents the random impurity potential in a normal metal

$$H_{\mathrm{imp}} = \sum_{j=1}^{L} \sum_{m=1}^{W} \sum_{\alpha} V_{\boldsymbol{r}} c^{\dagger}_{\boldsymbol{r},\alpha} c_{\boldsymbol{r},\alpha}, \tag{4.3}$$

where $V_{\boldsymbol{r}}$ is potential given randomly in the range of $-V_{\mathrm{imp}}/2 \leq V_{\boldsymbol{r}} \leq V_{\mathrm{imp}}/2$ and L denote the length of a DN in the x direction. We consider the SOI in a SC as

$$\begin{aligned} H_{\mathrm{SOI}} =& \frac{i}{2} \sum_{\boldsymbol{r},\alpha,\alpha'} \left[\lambda_x \left(c^{\dagger}_{\boldsymbol{r},\alpha} c_{\boldsymbol{r}+\boldsymbol{x},\alpha'} - c^{\dagger}_{\boldsymbol{r}+\boldsymbol{x},\alpha} c_{\boldsymbol{r},\alpha'} \right) (\sigma_y)_{\alpha,\alpha'} \right. \\ & \left. - \lambda_y \left(c^{\dagger}_{\boldsymbol{r},\alpha} c_{\boldsymbol{r}+\boldsymbol{y},\alpha'} - c^{\dagger}_{\boldsymbol{r}+\boldsymbol{y},\alpha} c_{\boldsymbol{r},\alpha'} \right) (\sigma_x)_{\alpha,\alpha'} \right], \end{aligned} \tag{4.4}$$

where $\lambda_{x(y)}$ represents the strength of SOI coupled with a momentum $k_x(k_y)$, and σ_i for $i = x, y$, and z represets the Pauli matrix in spin space. In this chapter, we mainly consider the three types SOI,

$$(\lambda_x, \lambda_y) = (\lambda, 0) \qquad x\text{-type}, \tag{4.5a}$$

$$(\lambda_x, \lambda_y) = (0, \lambda) \qquad y\text{-type}, \tag{4.5b}$$

$$(\lambda_x, \lambda_y) = (\lambda, \lambda) \qquad \text{RSOI}. \tag{4.5c}$$

The last one is the Rashba spin-orbit interaction (RSOI). The pair potential for a spin-singlet $d_{x^2-y^2}$ symmetry class is described by

$$H_\Delta = \frac{\Delta}{2} \sum_{j=L+1}^{\infty} \sum_{m=1}^{W} \Big(c^\dagger_{\boldsymbol{r}+\boldsymbol{x},\uparrow} c^\dagger_{\boldsymbol{r},\downarrow} + c^\dagger_{\boldsymbol{r},\uparrow} c^\dagger_{\boldsymbol{r}+\boldsymbol{x},\downarrow} \tag{4.6}$$

$$- c^\dagger_{\boldsymbol{r}+\boldsymbol{y},\uparrow} c^\dagger_{\boldsymbol{r},\downarrow} - c^\dagger_{\boldsymbol{r},\uparrow} c^\dagger_{\boldsymbol{r}+\boldsymbol{y},\downarrow} + \text{H.c.} \Big) , \tag{4.7}$$

with Δ being the amplitude of the pair potential. For a spin-singlet s-wave SC, we choose

$$H_\Delta = \Delta \sum_{j=L+1}^{\infty} \sum_{m=1}^{W} \left[c^\dagger_{\boldsymbol{r},\uparrow} c^\dagger_{\boldsymbol{r},\downarrow} + \text{H.c.} \right] . \tag{4.8}$$

The differential conductance of a DN/SC junction is calculated based on the Blonder-Tinkham-Klapwijk formula [78],

$$G_{\text{NS}}(eV) = \frac{e^2}{h} \sum_{k_y} \sum_{l,l',\alpha,\alpha'} \times \left[\delta_{l,l'} \delta_{\alpha,\alpha'} - |r^{\text{ee}}_{l,\alpha;l',\alpha'}|^2 + |r^{\text{he}}_{l,\alpha;l',\alpha'}|^2 \right]_{E=eV} , \tag{4.9}$$

where $r^{\text{ee}}_{l,\alpha;l',\alpha'}$ is the normal reflection coefficient from the l' th propagating channel with spin α' in the electron branch to the l th propagating channel with spin α in the electron branch, whereas $r^{\text{he}}_{l,\alpha;l',\alpha'}$ is the Andreev reflection coefficient from the l' th propagating channel with spin α' in the electron branch to the l th propagating channel with spin α in the hole branch. These reflection coefficients are calculated by using the recursive Green's function method [95, 80].

In this chapter, the energy is measured in units of t and we fix several parameters as $\mu = 2t$, $\Delta = 0.1t$, $L = 50$, and $W = 25$. We use 500 different samples for the ensemble averaging over random impurity configurations.

4.3 Results

4.3.1 d-wave

We first study the conductance in a junction consisting of a $d_{x^2-y^2}$-wave SC. In Fig. 4.2(a), the zero-bias conductance $G_{\text{NS}}(0)$ is plotted as a function of the normal state resistance of a DN R_{N} for $\lambda = 0.5t$. The results for the y-type SOI, those for RSOI, and those without SOI almost overlap with one another. They decrease with increasing R_{N} and vanish for large R_{N}. The effects of the SOI on the zero-bias conductance are negligible for y-type SOI and RSOI. These usual behaviors can be explained by the classical expression of the

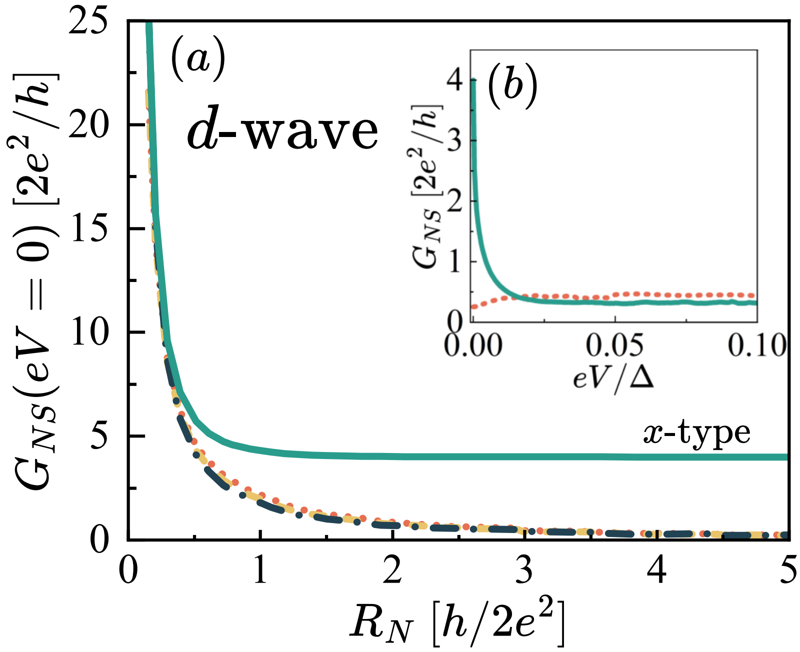

Figure 4.2: (a) The zero-bias differential conductance of a DN/SC junction as a function of normal state resistance R_{N} in a normal metal. The results for y-type SOI, those for RSOI, and those without SOI almost overlap with one another. They decrease to zero for $R_{\mathrm{N}} \to \infty$. The results for x-type SOI remain a finite value for $R_{\mathrm{N}} \to \infty$. (b) The differential conductance is plotted as a function of the bias voltage at $R_N = 4.5(h/e^2)$.

total resistance of the resistors in series. Because the resistance in a SC is zero, the total resistance of the junction would be given by

$$R_{\mathrm{NS}} = R_{\mathrm{B}} + R_{\mathrm{N}} = G_{\mathrm{NS}}^{-1}, \tag{4.10}$$

where R_{B} is the normal resistance due to the potential barrier at the DN/S interface. In the present results the Sharvin resistance replaces R_{B} because we do not introduce potential barrier at the interface. The relation $G_{\mathrm{NS}} \to 0$ is expected for large R_{N}. However, the conductance for x-type SOI deviates from such a classical relationship and saturates at a finite value of $4G_0$ for large R_{N} with $G_0 = 2e^2/h$. Such unusual behavior is an aspect of the APE.[15]. The resonant states at zero energy form the perfect transmission channels in a DN and cause the APE. Thus such an anomalous transport property remains only around zero bias. In Fig. 4.2(b), the differential conductance G_{NS} at $R_{\mathrm{N}} = 4.5G_0^{-1}$ is plotted as a function of the bias voltage eV. The results for the x-type SOI decrease rapidly with increasing eV. As a consequence, the results for the x-type SOI exhibits a sharp peak at zero-bias. The width of the zero-bias peak depends on R_{N}. For comparison, we plot the results for RSOI in Fig. 4.2(b) with a broken line. The conductance exhibits no distinct peak structures around zero bias.

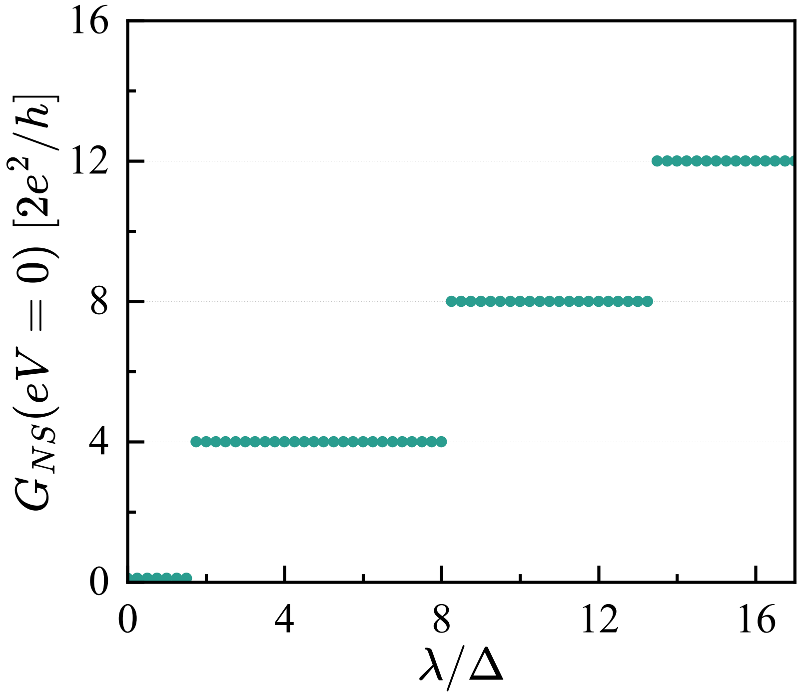

Figure 4.3: The zero-bias conductance of a $d_{x^2-y^2}$-wave junction for x-type SOI is plotted as a function of the strength of SOI λ_x at $R_N = 4.5G_0^{-1}$.

In a $d_{x^2-y^2}$-wave SC with x-type SOI, the zero-bias conductance in the limit of $R_{\mathrm{N}} \to \infty$ depends on the amplitude of SOI λ as shown in Fig. 4.3, where $G_{\mathrm{NS}}(0)$ is plotted as a function of λ. The conductance remains zero for $\lambda < 0.175t$ and jumps to a finite value of $8G_0$ at $\lambda_x = 0.175t$. Such step-like behavior is observed also at $\lambda_x = 0.85t$ and $\lambda_x = 1.35t$. The conductance is quantized at $4G_0$, 8 G_0, and 12 G_0, these steps. As we will discuss in Sec. 4.4, the minimum value of the conductance is given by $G_0\mathcal{N}_{\mathrm{ZES}}$, where a factor 2 is derived from the perfect Andreev reflection and $\mathcal{N}_{\mathrm{ZES}}$ is the number of zero-energy states that form the perfect transmission channels in a DN. The results indicate that $\mathcal{N}_{\mathrm{ZES}}$ changes discontinuously by 4. Such a discontinuous behavior is also a typical property of the APE.

4.3.2 s-wave

At the end of the numerical simulation, we discuss the absence of the APE in a DN/SC junction for an s-wave symmetry. In Fig. 4.4(a), we plot the zero-bias conductance as a function of R_{N} for a s-wave superconductor including x-type SOI, y-type SOI, and RSOI with $\lambda = 0.5t$. For comparison, we also plot the results without SOI $\lambda = 0$ in the figure. All of the results overlap with one another, which indicate that the effects of SOI on the conductance are negligible in an s-wave junction. In all cases, the zero-bias conductance

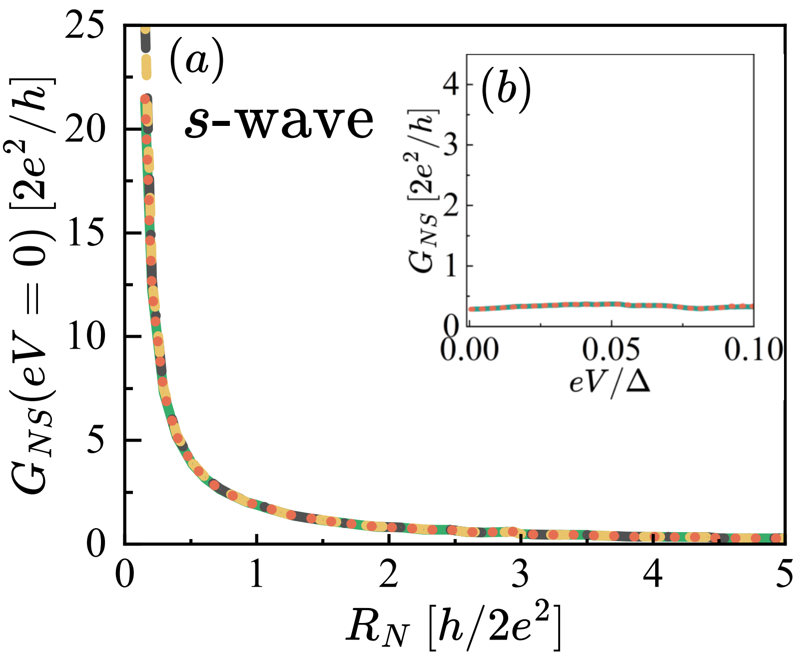

Figure 4.4: (a) The conductance for an s-wave DN/SC junction. The zero-bias differential conductance is plotted as a function of normal state resistance R_{N} in a normal metal. Although we consider x- and y-types SOI, RSOI, and absence of SOI, all of the results almost overlap with one another. (b) The differential conductance is plotted as a function of the bias voltage at $R_N = 4.5(h/e^2)$.

decreases to zero with increasing R_{N}. In the inset of Fig. 4.4(b), we also plot the differential conductance G_{NS} at $R_N = 4.5G_0^{-1}$ as a function of the bias voltages. The results show that the conductance is insensitive to the bias voltage. The results in Fig. 4.4 suggest that s-wave superconductor junctions do not indicate the APE regardless of the type of SOI. We will discuss the reasons in Sec. 4.4.

4.4 Modified pair potential and Index

To analyze the numerical results, we discuss how x-type SOI modifies the pair potential on the Fermi surface of a $d_{x^2-y^2}$ SC. In this section, we discuss the Hamiltonian in continuous space

$$H_{\mathrm{BdG}}(\boldsymbol{k}) = (\xi_{\boldsymbol{k}} - \lambda_x k_x \hat{\sigma}_y)\tau_z - \Delta(\boldsymbol{k})\sigma_y \tau_y. \tag{4.11}$$

which enable us to derive the analytical expression of the quantized value of the conductance minumum. There are two conditions for a superconductor that indicates the APE: the existence of the Andreev bound states at its surfaces parallel to the y direction and the presence of the usual proximity effect. [6] A SC causes the usual proximity effect when its the pair potential satisfies [83]

$$\Delta(k_x, -k_y) \neq -\Delta(k_x, k_y), \tag{4.12}$$

where k_x and k_y are the wave number on the Fermi surface. The pair potentials considered in this chapter are described by

$$\Delta(\boldsymbol{k}) = \begin{cases} \Delta(k_x^2 - k_y^2)/k_F^2 & : d_{x^2-y^2}-\text{wave} \\ \Delta & : s-\text{wave} \end{cases}, \tag{4.13}$$

where k_F is the Fermi wave number on the isotropic Fermi surface. Both $d_{x^2-y^2}$-wave pair potential and s-wave pair potential satisfy Eq. (4.12). This condition is also satisfied even in the presence of SOIs. In the junction geometry in Fig. 4.1, the wave number in the y direction k_y indicates a transport channel in the x direction. Meanwhile, the presence of the surface Andreev bound states is ensured when the pair potential satisfies [7, 8]

$$\Delta(k_x, k_y)\Delta(-k_x, k_y) < 0. \tag{4.14}$$

Either $d_{x^2-y^2}$-wave pair potential or s-wave pair potential do not satisfy the condition in the absence of SOIs. [6]

The SOIs modify the shape of the Fermi surface as shown in Fig. 4.5, where we illustrate the pair potential on the Fermi surface in the presence of SOIs. The black dot indicates the Γ point in the two-dimensional Brillouin zone ($\boldsymbol{k} = 0$). The results for $d_{x^2-y^2}$-wave pair potentials in Fig. 4.5 show that the x-type SOI shifts the two Fermi surfaces: one moves to $+k_x$ direction and the other moves to $-k_x$ direction. As a result, Eq. (4.14) is satisfied along the black dotted lines, where the corresponding k_y domain is determined by Eq.(D.5). The one-dimensional winding number at fixed k_y is defined by [13]

$$\mathcal{W}(k_y) \equiv -\frac{1}{4\pi i}\int_{-\infty}^{\infty} dk_x\, I(k_y), \tag{4.15}$$

$$I(k_y) = \mathrm{Tr}\left[\hat{\tau}_x\, H_{\mathrm{BdG}}^{-1}\, \partial_{k_x}\, H_{\mathrm{BdG}}\right], \tag{4.16}$$

$$\{H_{\mathrm{BdG}}, \hat{\tau}_x\}_+ = 0. \tag{4.17}$$

The one-dimensional winding number is

$$\mathcal{W}(k_y) = \mathcal{W}(-k_y) = 2, \tag{4.18}$$

for all k_y values indicated by the black dotted line in 4.5(a). Because the pair potential is an even function of k_y, it is possible to show

$$\mathcal{N}_{\mathrm{ZES}} = \sum_{k_y} \mathcal{W}(k_y), \tag{4.19}$$

remains a finite value for each Fermi surface. This index represents the number of zero-energy states which form the resonant transmission channels in a DN. [15] The conductance at for large enough R_{N} is quantized

$$G_{\mathrm{NS}} = G_0 \times |\mathcal{N}_{\mathrm{ZES}}|. \tag{4.20}$$

Thus $\mathcal{N}_{\mathrm{ZES}}$ increases by 2 with increasing λ_x. As a result, the quantized conductance increases by $4G_0$ with increasing λ_x as shown in Fig. 4.3. When we assume doubly degenerate circular Fermi surfaces at $\lambda = 0$, the index is approximately calculated as

$$\mathcal{N}_{\mathrm{ZES}} \approx \left[2N_c \, \frac{\lambda_x k_F}{\mu} \right]_{\mathrm{G}}, \tag{4.21}$$

where $[\cdots]_{\mathrm{G}}$ means the integer part of the argument, N_c is the number of propagatting channels on the Fermi surface per spin. Details of the derivation are supplied in Appendix D. Thus the quantized value of the conductance increases monotonically with increasing λ_x. In Fig. 4.3, the conductance jumps discontinuously because the number of propagating channels are limited for $W = 25$ in the numerical simulation. The width of the plateaus in Fig. 4.3 decreases as W increases, because the index $\mathcal{N}_{\mathrm{ZES}}$ also depends on N_c. In contrast, the index is an invariant remains unchanged even in the presence of random impurity potential. Details of the proof were given in Ref. [15] and are summarized in Appendix.

The $d_{x^2-y^2}$-wave pair potentials with the y-type SOI in Fig. 4.5(b) and that with the RSOI in Fig. 4.5(c) do not satisfy Eq. (4.14) because they are always even functions of k_x. In Fig. 4.5(d), we also illustrate the pair potential for s-wave symmetry with the x-type SOI. Although the SOI splits the Fermi surface into two and modifies the amplitudes of the pair potentials, it does not change the sign of the pair potentials. Therefore, the APE is absent in these junctions.

4.5 Discussion

Finally, we discuss a relation between the conclusions of this chapter and the experimental results in $CoSi_2/TiO_2$ on a Si substrate [17]. The experiment in a T-shaped proximity junction shows a clear zero-bias peak in the conductance spectra, which is an aspect of the APE. They reported strong SOIs near the $CoSi_2$/Si interface, suggesting that these SOIs show to result in the APE in the $CoSi_2$ spin-singlet s-wave SC. At the same time, one of the authors of the experimental report theoretically demonstrated the zero-bias conductance peak [19, 96]. Their studies on two-dimensional T-shaped junctions [19] and DN/SC junctions [96] where substrate-induced RSOC lead to mixing of the spin-singlet and spin-triplet order parameters. In the spin-triplet dominant limit, their theoretical

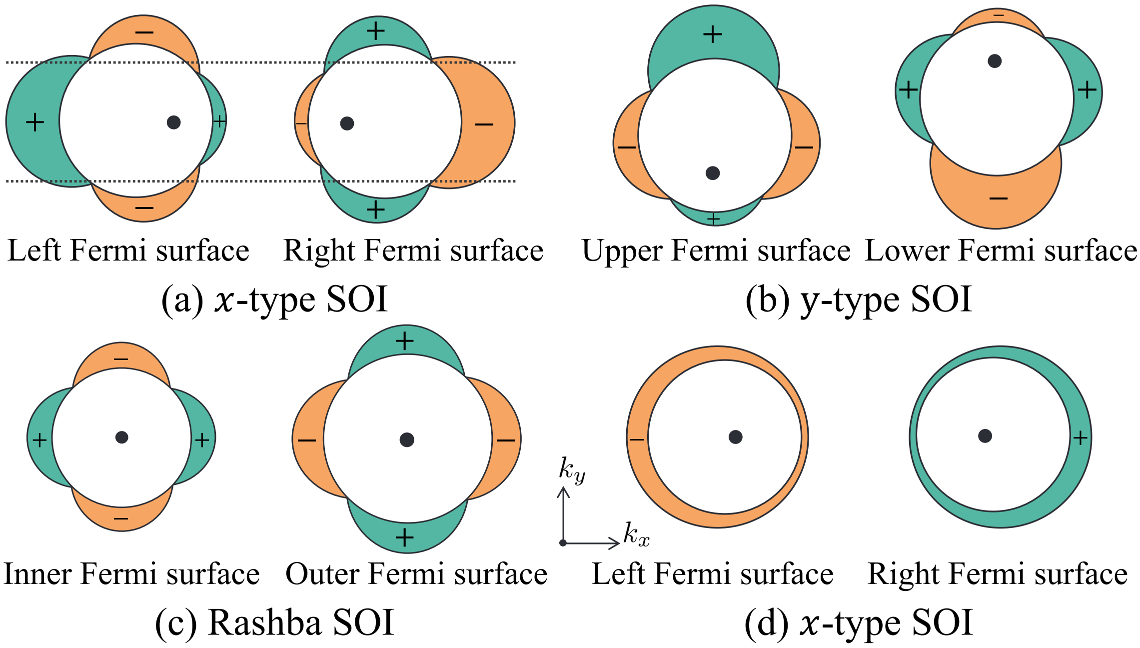

Figure 4.5: The pair potentials of a $d_{x^2-y^2}$-wave SC on the Fermi surface with (a) x-type SOI and (b) y-type SOI, and (c) RSOI. The black dot in the figure indicates the Γ point ($\boldsymbol{k} = 0$). On the dotted lines in (a), the condition $\Delta(k_x, k_y)\Delta(-k_x, k_y) < 0$ is satisfied. In (d), the pair potentials of an s-wave SC are illustrated for x-type SOI.

results show a robust zero-bias peak in the conductance of these junctions. This suggests the possibility that $CoSi_2$ becomes a noncentrosymmetric SC in two-dimensional junctions with strong SOI.

In this chapter, we considered a different scenario where the SC has only a spin-singlet order parameter. Our findings indicate a fundamental resistance to SOI-induced effects due to the isotropic and sign invariant nature of s-wave symmetry. Conversely, we found a robust APE in a $d_{x^2-y^2}$-wave SC with specific SOI, which arise from the formation of a resonant transmission channel stabilized by the anisotropic d-wave symmetry. Our finding suggests that the APE in $CoSi_2$ may result from the symmetry change from s-wave to d-wave at two-dimentional thin $CoSi_2$ film.

4.6 Summary

We theoretically studied the effects of the spin-orbit interaction (SOI) in a spin-singlet superconductor on the low-energy transport properties in a dirty normal-metal/superconductor junction as shown in Fig. 1. We introduce the random impurity potential in a normal metal and the spin-singlet d-wave pair potential in a superconductor (SC). The differential conductance is calculated based on the Blonder-Tinkham-Klapwijk formula and the transport coefficients are calculated numerically by using the recursive Green's function method. We investigate two types of pair potentials in DN/SC junctions, both of which lack ABS at the interface in the absence of SOIs. In the simulation, we consider three types of SOI such as x-type, y-type, and Rashba type. Our results demonstrate that a d-wave SC with x-type SOI exhibits the anomalous proximity effect, whereas a d-wave SC with y-type SOI and a d-wave SC with Rashba SOI do not indicate the APE. The numerical results also show that an s-wave SC with any types of SOI does not show the APE. We explain the reasons of these results by analyzing the sign change of the pair potential on the Fermi surface modified by SOIs.

The APE is a characteristic phenomenon of spin-triplet SCs. Therefore, the observation of the APE in experiments would be difficult because the spin-triplet SCs are very rare even now. Our findings suggest an alternative route for observing the APE and provide an experimental setup for realizing an effective spin-triplet SC.

Chapter **5**

Effect of the exchange potential and spin-orbit interaction on a spin-singlet Cooper pairs

Abstract

We investigate theoretically the proximity effect in a ferromagnetic semiconductor with the Rashba spin-orbit interaction. The interplay between the exchange potential and the spin-orbit interactions enhances the symmetry variety of Cooper pairs depending on the degree of disorder in the ferromagnet. In the ballistic limit, spin-singlet s-wave Cooper pairs are the most dominant in the presence of strong spin-orbit interaction because the spin-momentum locking stabilizes a Cooper pair consisting of two electrons that are time-reversal partners of each other. We demonstrate that the spin-orbit interactions induce equal-spin-triplet p-wave pairs. In the dirty regime, on the other hand, equal-spin-triplet s-wave pairs dominate because random impurity potentials disrupt the locking. The exchange splitting in the conduction band leads to an imbalance between the two equal-spin pairing components. In a half-metallic ferromagnet, only one equal-spin pairing component survives and carries the spin-polarized supercurrent. We analyze the effects of the spin-orbit interaction on the Josephson current.

5.1 Introduction

The proximity effect in ferromagnetic metals has long been a central topic in the physics of superconductivity [97, 98, 99]. The interplay between the exchange potential in ferromagnets and superconductivity significantly enriches the symmetry of Cooper pairs. Specifically, the uniform exchange potential induces the formation of opposite-spin-triplet

Cooper pairs from spin-singlet s-wave Cooper pairs. These pairing functions exhibit oscillatory behavior and decay spatially within the ferromagnet, which plays a crucial role in 0-π transitions in superconductor/ferromagnet/superconductor (SFS) junctions [100, 101, 102]. Furthermore, the inhomogeneity in the magnetic moments near the junction interface promotes the generation of equal-spin-triplet Cooper pairs, which carry the long-range Josephson current in SFS junctions [99, 103, 104, 105, 106]. In the diffusive transport regime, all spin-triplet components belong to the odd-frequency symmetry class [99, 107, 108, 109, 110].

SFS junctions consisting of ferromagnetic semiconductors offer a promising route for exploring spin-triplet Cooper pairs [111]. This is due to their tunable magnetic moment through doping, allowing precise control of the spin configuration. Moreover, long-range phase coherence is anticipated in high-mobility two-dimensional electron gases in semiconductors [112, 113]. Recent experiments have observed supercurrents flowing through Nb/(In,Fe)As/Nb junctions [114, 115], providing experimental evidence for the presence of spin-triplet Cooper pairs. The Rashba spin-orbit interaction, tunable by gating the ferromagnetic segment in SFS junctions, further modifies the spin configuration and plays a significant role in the spin structure in momentum space.

While several theoretical studies have examined the interplay between exchange potential and spin-orbit interaction in proximity effects [116, 117, 118, 119, 120, 121, 122, 123, 124], a comprehensive analysis of the Cooper pair symmetry that contributes most significantly to the Josephson current across a broad range of exchange potentials, spin-orbit interactions, and disorder degrees has yet to be performed. This chapter aims to address this gap by providing a detailed study of these symmetries.

In this work, we theoretically investigate the Cooper pair symmetries in a two-dimensional ferromagnetic semiconductor with Rashba spin-orbit interaction. The pairing functions are computed numerically using the lattice Green's function technique applied to SFS junctions. This method allows for a detailed analysis across varying strengths of exchange potential, spin-orbit interactions, and impurity-induced disorder. Our results reveal that the pairing symmetry of the dominant Cooper pair in a ferromagnet is highly sensitive to both spin-orbit coupling and disorder. In the regime of strong spin-orbit interaction, a spin-singlet s-wave Cooper pair dominates in ballistic ferromagnets, while in diffusive ferromagnets, an equal-spin-triplet s-wave pair becomes dominant. Additionally, we discuss the influence of spin-orbit interactions on the 0-π transition in SFS junctions.

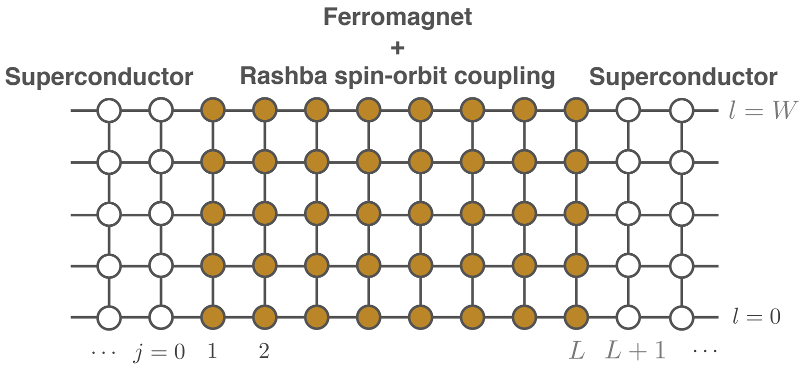

Figure 5.1: SFS junction on two-dimensional tight-binding model.

5.2 Model

Let us consider an SFS junction on two-dimensional tight-binding lattice as shown in Fig. 5.1, where L is the length of the ferromagnetic semiconductor, W is the width of the junction in units of the lattice constant, $\boldsymbol{x}$ ($\boldsymbol{y}$) is the unit vector in the x (y) direction, $\boldsymbol{r} = j\boldsymbol{x} + m\boldsymbol{y}$ points a lattice position. The Hamiltonian of the junction is given by

$$\mathcal{H} = \sum_{\boldsymbol{r},\boldsymbol{r}'} \Psi^\dagger(\boldsymbol{r}) \left[\begin{array}{cc} \hat{H}_{\rm N}(\boldsymbol{r},\boldsymbol{r}') & \hat{\Delta}(\boldsymbol{r},\boldsymbol{r}') \\ -\hat{\Delta}^*(\boldsymbol{r},\boldsymbol{r}') & -\hat{H}^*_{\rm N}(\boldsymbol{r},\boldsymbol{r}') \end{array} \right] \Psi(\boldsymbol{r}'), \tag{5.1}$$

$$\Psi(\boldsymbol{r}) =[\psi_\uparrow(\boldsymbol{r}), \psi_\downarrow(\boldsymbol{r}), \psi^\dagger_\uparrow(\boldsymbol{r}), \psi^\dagger_\downarrow(\boldsymbol{r})]^{\rm T}, \tag{5.2}$$

where $\psi_\alpha(\boldsymbol{r})$ is the annihilation operator of an electron with spin α at $\boldsymbol{r}$. The normal state Hamiltonian consists of four terms as,

$$\hat{H}_{\rm N} =\hat{H}_{\rm k} + \hat{H}_{\rm so} + \hat{H}_{\rm h} + \hat{V}_{\rm i}, \tag{5.3}$$

$$\begin{aligned} \hat{H}_{\rm k}(\boldsymbol{r},\boldsymbol{r}') =& -t\left(\delta_{\boldsymbol{r},\boldsymbol{r}'+\boldsymbol{x}} + \delta_{\boldsymbol{r}+\boldsymbol{x},\boldsymbol{r}'}\right)\hat{\sigma}_0 \\ & -t\left(\delta_{\boldsymbol{r},\boldsymbol{r}'+\boldsymbol{y}} + \delta_{\boldsymbol{r}+\boldsymbol{y},\boldsymbol{r}'}\right)\hat{\sigma}_0 \\ & + (4t - \epsilon_F)\delta_{\boldsymbol{r},\boldsymbol{r}'}\hat{\sigma}_0, \end{aligned} \tag{5.4}$$

$$\begin{aligned} \hat{H}_{\rm so}(\boldsymbol{r},\boldsymbol{r}') =& i(\lambda/2)\left[\left\{\delta_{\boldsymbol{r},\boldsymbol{r}'+\boldsymbol{x}} - \delta_{\boldsymbol{r}+\boldsymbol{x},\boldsymbol{r}'}\right\}\hat{\sigma}_2\right. \\ & \left. - \left\{\delta_{\boldsymbol{r},\boldsymbol{r}'+\boldsymbol{y}} - \delta_{\boldsymbol{r}+\boldsymbol{y},\boldsymbol{r}'}\right\}\hat{\sigma}_1\right]\Theta(j)\,\Theta(L-j), \end{aligned} \tag{5.5}$$

$$\hat{H}_{\rm h}(\boldsymbol{r},\boldsymbol{r}') = -\boldsymbol{h}\cdot\boldsymbol{\sigma}\,\delta_{\boldsymbol{r},\boldsymbol{r}'}\,\Theta(j)\,\Theta(L+1-j), \tag{5.6}$$

$$\hat{H}_{\rm i}(\boldsymbol{r},\boldsymbol{r}') =v_{\boldsymbol{r}}\,\sigma_0\,\delta_{\boldsymbol{r},\boldsymbol{r}'}\,\Theta(j)\,\Theta(L+1-j), \tag{5.7}$$

$$\begin{aligned} \hat{\Delta}(\boldsymbol{r},\boldsymbol{r}') =& \Delta\,\delta_{\boldsymbol{r},\boldsymbol{r}'}\,i\,\hat{\sigma}_2 \\ & \times\left[\Theta(-j+1)e^{i\varphi_L} + \Theta(j-L)e^{i\varphi_R}\right], \end{aligned} \tag{5.8}$$

$$\Theta(j) = \left\{ \begin{array}{ll} 1 & : j > 1 \\ 0 & : j \leq 0 \end{array} \right. , \tag{5.9}$$

where t is the hopping integral among the nearest neighbor lattice sites, ϵ_F is the Fermi energy, $\hat{\sigma}_j$ for $j = 1{-}3$ and $\hat{\sigma}_0$ are the Pauli's matrix and unit matrix in spin space, respectively. In the ferromagnet ($1 \le j \le L$), λ is the amplitude of the spin-orbit interaction, $\boldsymbol{h}$ represents the uniform exchange potential, and $v_{\boldsymbol{r}}$ represents random impurity potential. In the two superconductors, Δ is the amplitude of the pair potential of spin-singlet s-wave symmetry, and $\varphi_L(\varphi_R)$ is the superconducting phase in the left (right) superconductor. We solve the Gor'kov equation

$$\begin{aligned}
&\left[i\omega_n \hat{\tau}_0 \hat{\sigma}_0 - \sum_{\boldsymbol{r}_1} \begin{pmatrix} \hat{H}_{\mathrm{N}}(\boldsymbol{r},\boldsymbol{r}_1) & \hat{\Delta}(\boldsymbol{r},\boldsymbol{r}_1) \\ -\hat{\Delta}^*(\boldsymbol{r},\boldsymbol{r}_1) & -\hat{H}^*_{\mathrm{N}}(\boldsymbol{r},\boldsymbol{r}_1) \end{pmatrix} \right] \\
&\times \check{G}_{\omega_n}(\boldsymbol{r}_1,\boldsymbol{r}') = \hat{\tau}_0\hat{\sigma}_0 \delta(\boldsymbol{r}-\boldsymbol{r}'), \qquad (5.10)\\
&\check{G}_{\omega_n}(\boldsymbol{r},\boldsymbol{r}') = \begin{bmatrix} \hat{G}_{\omega_n}(\boldsymbol{r},\boldsymbol{r}') & \hat{F}_{\omega_n}(\boldsymbol{r},\boldsymbol{r}') \\ -\hat{F}^*_{\omega_n}(\boldsymbol{r},\boldsymbol{r}') & -\hat{G}^*_{\omega_n}(\boldsymbol{r},\boldsymbol{r}') \end{bmatrix}, \qquad (5.11)
\end{aligned}$$

by applying the lattice Green's function technique [95, 125], where τ_0 is the unit matrix in particle-hole space, $\omega_n = (2n+1)\pi T$ is the fermionic Matsubara frequency, and T is a temperature. The Josephson current in a ferromagnet $1 < j < L$ expressed as

$$\begin{aligned}
J(j) = &-\frac{ie}{2} T \sum_{\omega_n} \sum_{m=1}^{W} \mathrm{Tr}\left[\hat{\tau}_3 \check{T}_+ \check{G}_{\omega_n}(\boldsymbol{r},\boldsymbol{r}+\boldsymbol{x}) \right. \\
&\left. - \hat{\tau}_3 \check{T}_- \check{G}_{\omega_n}(\boldsymbol{r}+\boldsymbol{x},\boldsymbol{r}) \right], \qquad (5.12)\\
\check{T}_\pm = &\begin{bmatrix} -t\hat{\sigma}_0 \mp i(\lambda/2)\hat{\sigma}_2 & 0 \\ 0 & t\hat{\sigma}_0 \pm i(\lambda/2)\hat{\sigma}_2 \end{bmatrix}, \qquad (5.13)
\end{aligned}$$

is independent of j.

The pairing function with s-wave symmetry is decomposed into four components

$$\frac{1}{W} \sum_{m=1}^{W} \hat{F}_{\omega_n}(\boldsymbol{r},\boldsymbol{r}) = \sum_{\nu=0}^{3} f_\nu(j) \hat{\sigma}_\nu i\hat{\sigma}_2, \qquad (5.14)$$

where f_0 is a spin-singlet component and f_j with $j = 1-3$ are spin-triplet components. In the clean limit, we also calculate pairing function with an odd-parity symmetry

$$\begin{aligned}
&\frac{1}{2W} \sum_{m=1}^{W} \hat{F}_{\omega_n}(\boldsymbol{r}+\boldsymbol{x},\boldsymbol{r}) - \hat{F}_{\omega_n}(\boldsymbol{r}-\boldsymbol{x},\boldsymbol{r}), \\
&= \sum_{\nu=0}^{3} f_\nu(j)\hat{\sigma}_\nu i\hat{\sigma}_2. \qquad (5.15)
\end{aligned}$$

Throughout this chapter, we fix several parameters as $W = 20$, $\epsilon_F = 2t$, $\Delta = 0.005t$, and $T/T_c = 0.1$. The exchange field is always in the perpendicular direction to the two-dimensional place $\boldsymbol{h} = h\boldsymbol{z}$.

5.3 Results

5.3.1 Josephson current in clean limit

We first discuss the numerical results of the Josephson current plotted as a function of the length of a ferromagnet L in Fig. 5.2, where we fix the phase difference at $\varphi = \varphi_L - \varphi_R = 0.5\pi$. Fig. 5.2(a) and (b) show the results in the absence of exchange potential $h = 0$ and in the presence of an exchange potential $h = 0.5t$, respectively. The Josephson current is normalized to $J_0 = e\Delta$ throughout this chapter. The amplitude of the Josephson current slightly decreases with the increase of L because the pairing functions decay as e^{-x/ξ_T^C} with $\xi_T^C = v_F/2\pi T$ for all pairing symmetry. We will discuss this point later on by using analytic expression of the pairing function obtained by solving Eilenberger equation. Since $h = 0$ in Fig. 5.2(a), the junction corresponds to superconductor/normal-metal/superconductor junction. The results show that the spin-orbit interaction modifies the Josephson current very slightly. On the other hand in Fig. 5.2(b), the Josephson current oscillates as a function of L because of the exchange potential. The period of the oscillations is described by $\xi_h^C = v_F/2h$ in weak spin-orbit interactions. When the spin-orbit interactions increase, the amplitude of the oscillations decreases. At $\lambda = 0.5t$, the Josephson current is always positive at $\varphi = 0.5\pi$. In the present calculation at $T/T_c = 0.1$, the current-phase relationship (CPR) deviates slightly from sinusoidal function. Roughly speaking, the spin-orbit interaction stabilizes the 0 state rather than the π state.

In Fig. 5.3, we show a phase diagram of the Josephson current at $\varphi = 0.5\pi$ and $L = 50$, where horizontal (vertical) axis indicates the amplitude of the spin-orbit interaction (exchange potential). The junction is in the 0 state for $J > 0$ and is in the π state for $J < 0$. At $\lambda = 0$, the Josephson current changes its sign with the increase of h, which indicates the 0-π transition by the exchange potential. When we introduce the spin-orbit interaction, the 0-π transitions is suppressed and the Josephson current is always positive. Roughly speaking π state disappears for $\lambda > h$. We will discuss the reasons for disappearing the π state under the strong spin-orbit interactions in the next subsection.

5.3.2 Pairing functions in clean limit

To analyze the characteristic behavior of the Josephson current, we solve the Eilenberger equation [126] in a ferromagnet,

$$iv_F\hat{\boldsymbol{k}} \cdot \nabla_{\boldsymbol{r}}\check{g} + [\check{H}_0 + \check{\Delta}, \check{g}]_- = 0, \tag{5.16}$$

$$\check{H}_0 = (i\omega_n - \boldsymbol{h} \cdot \hat{\boldsymbol{\sigma}})\,\hat{\tau}_3 - \boldsymbol{\lambda} \times \hat{\boldsymbol{\sigma}} \cdot \hat{\boldsymbol{k}}, \tag{5.17}$$

$$\check{\Delta} = i\hat{\Delta}\hat{\tau}_1. \tag{5.18}$$

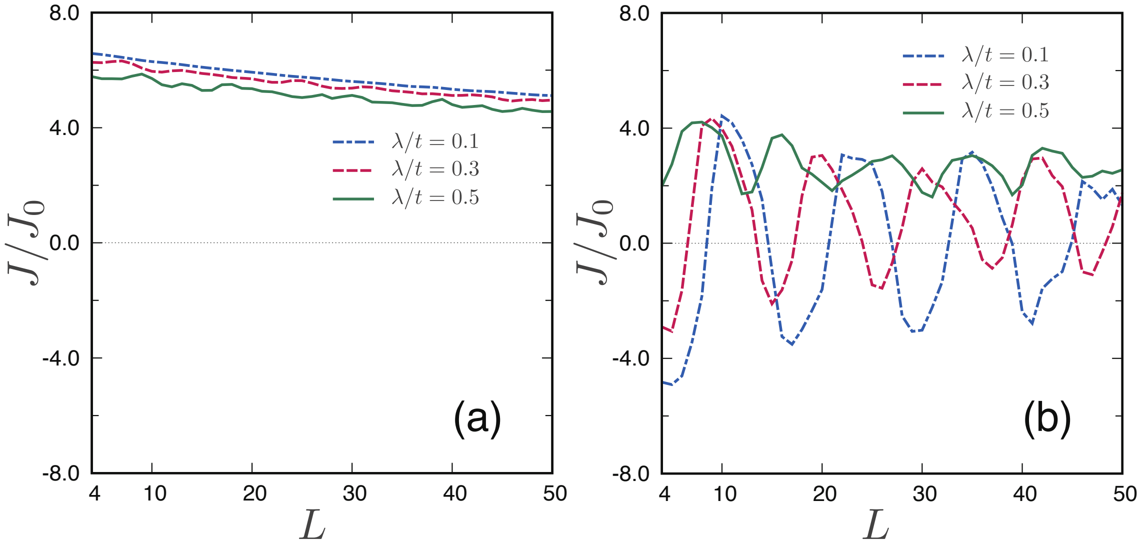

Figure 5.2: The Josephson current versus the length of a normal segment L in the clean limit. (a): an SNS junction at $h = 0$. (b): an SFS junction at $h = 0.5t$.

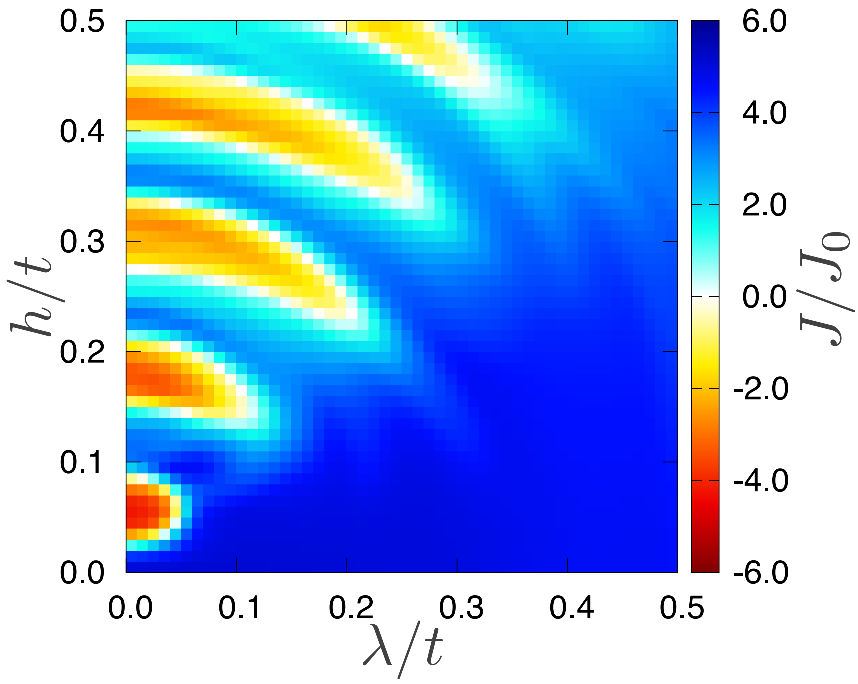

Figure 5.3: The Josephson current at $\varphi = 0.5\pi$ and $L = 50$ is plotted as a function of h and λ in the clean limit.

To solve the Eilenberger equation, we apply the Riccati parameterization,

$$\check{g} = \begin{pmatrix} \hat{N} & \hat{0} \\ \hat{0} & \underline{\hat{N}} \end{pmatrix} \begin{pmatrix} s_{\omega_n}(1-\hat{a}\underline{\hat{a}}) & 2\hat{a} \\ 2\underline{\hat{a}} & -s_{\omega_n}(1-\underline{\hat{a}}\hat{a}) \end{pmatrix}, \tag{5.19}$$

where $s_{\omega_n} = \mathrm{sgn}(\omega_n)$. The two Riccati parameter are related to each other by $\underline{\hat{a}}(\boldsymbol{r}, \hat{\boldsymbol{k}}, \imath\omega_n) = \hat{\sigma}_2 \hat{a}^*(\boldsymbol{r}, -\hat{\boldsymbol{k}}, i\omega_n)\hat{\sigma}_2$. One of the Riccati parameter obeys

$$\begin{aligned} & iv_F \hat{\boldsymbol{k}} \cdot \nabla \hat{a} + 2i\omega_n \hat{a} - \boldsymbol{h} \cdot \hat{\boldsymbol{\sigma}} \hat{a} - \hat{a}\hat{\boldsymbol{\sigma}} \cdot \boldsymbol{h} - \hat{\boldsymbol{k}} \times \boldsymbol{\lambda} \cdot \hat{\boldsymbol{\sigma}} \hat{a} \\ & \quad + \hat{a}\hat{\boldsymbol{k}} \times \boldsymbol{\lambda} \cdot \hat{\boldsymbol{\sigma}} - i\Delta + i\hat{a}\Delta\hat{a} = 0. \end{aligned} \tag{5.20}$$

Since $\Delta = 0$ in a ferromagnet ($x > 0$), it is possible to have an analytic solution of

$$\hat{a}(\boldsymbol{r}, \hat{\boldsymbol{k}}, i\omega_n) = \sum_{\nu=0}^{3} a_\nu(\boldsymbol{r}, \hat{\boldsymbol{k}}, i\omega_n)\hat{\sigma}_\nu. \tag{5.21}$$

The spin-singlet component satisfies

$$a_0(\boldsymbol{r}, \hat{\boldsymbol{k}}, i\omega_n) = a_0(\boldsymbol{r}, -\hat{\boldsymbol{k}}, -i\omega_n), \tag{5.22}$$

and the three spin-triplet components satisfy

$$a_j(\boldsymbol{r}, \hat{\boldsymbol{k}}, i\omega_n) = -a_j(\boldsymbol{r}, -\hat{\boldsymbol{k}}, -i\omega_n), \tag{5.23}$$

for $j = 1-3$. For $\boldsymbol{h} = h\boldsymbol{z}$ and $\boldsymbol{\lambda} = \lambda\boldsymbol{z}$, we obtain the solution in two-dimension,

$$a_0 = \frac{A_0}{V^2}\left[h^2 \cos\left(\frac{2V}{v_{F_x}}x\right) + \lambda^2\right] e^{-\frac{2\omega_n}{v_{F_x}}x}, \tag{5.24}$$

$$a_{\uparrow\uparrow} = a_1 - ia_2, \tag{5.25}$$

$$= \frac{A_0 h\lambda}{V^2}(k_y + ik_x)\left[1 - \cos\left(\frac{2V}{v_{F_x}}x\right)\right] e^{-\frac{2\omega_n}{v_{F_x}}x}, \tag{5.26}$$

$$a_{\downarrow\downarrow} = a_1 + ia_2, \tag{5.27}$$

$$= \frac{A_0 h\lambda}{V^2}(-k_y + ik_x)\left[1 - \cos\left(\frac{2V}{v_{F_x}}x\right)\right] e^{-\frac{2\omega_n}{v_{F_x}}x}, \tag{5.28}$$

$$a_3 = i\frac{A_0 h}{V}\sin\left(\frac{2V}{v_{F_x}}x\right) e^{-\frac{2\omega_n}{v_{F_x}}x}, \tag{5.29}$$

where $V = \sqrt{h^2 + \lambda^2}$, $v_{F_x} = k_x/m$ and $A_0 = \Delta/(|\omega_n| + \sqrt{\omega_n^2 + \Delta^2})$ is the solution in a uniform superconductor. At the interface of a superconductor and a ferromagnet ($x = 0$), we imposed a boundary condition of $a_0 = A_0$ and $a_j = 0$ for $j = 1-3$. The decay length of all the components is basically given by the thermal coherence in the clean limit $\xi_T^C = v_F/2\pi T$. The spin-singlet component a_0 has two contributions: an oscillating term due to the exchange potential and a constant term due to the spin-orbit interaction. Eqs. (5.24)-(5.29) suggest that only a spin-singlet pair stays in an SNS junction. Thus

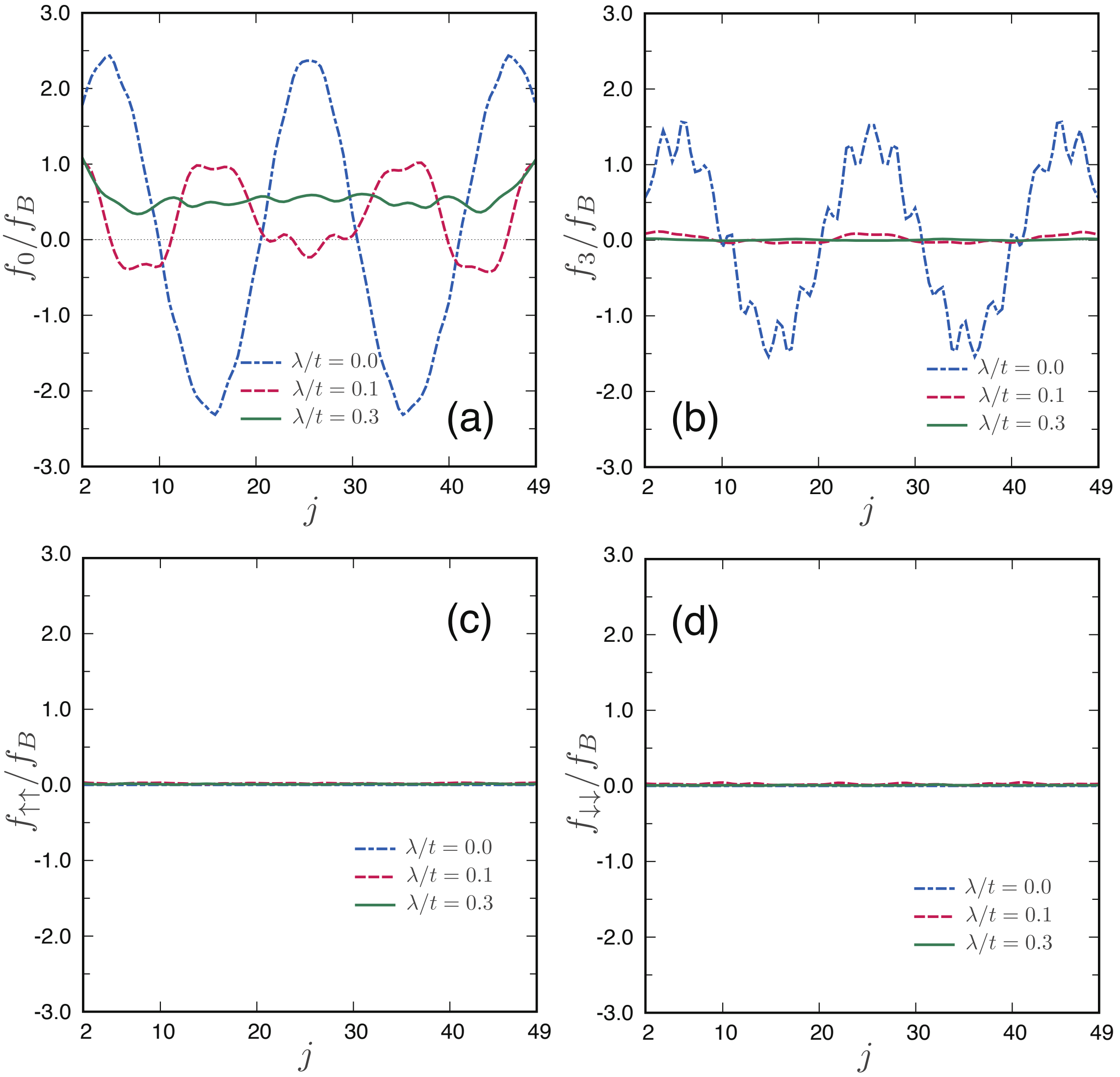

Figure 5.4: The spatial profile of the pairing functions at $L = 50$ and $h = 0.3t$ in the clean limit. The results for an s-wave symmetry in Eq. (5.14) are presented. (a) spin-singlet f_0, (b) opposite-spin-triplet f_3, (c) equal-spin-triplet $f_{\uparrow\uparrow}$, and (c) equal-spin-triplet $f_{\downarrow\downarrow}$

the spin-orbit interaction does not affect the Josephson current so much as shown in Fig. 5.2(a). A opposite-spin-triplet component a_3 also oscillates in real space. The pairing function for equal-spin pairs $f_{\uparrow\uparrow}$ and $f_{\downarrow\downarrow}$ become finite in the presence of the spin-orbit unteraction and oscillate in real space. They, however, do not change their sign.

In Fig. 5.4, we show the numerical results of pairing function in the ferromagnet of an SFS junction on the tight-binding model, where $L = 50$, $\varphi = 0$, $h = 0.3t$, and $\omega_n = 0.02\Delta$. We first display the spatial profile of s-wave components in Eq. (5.14) for several choices of λ. The spin-singlet s-wave component f_0 in (a) oscillates and changes its sign in real space at $\lambda = 0$. However, the spin-orbit interaction suppresses the sign change. As a

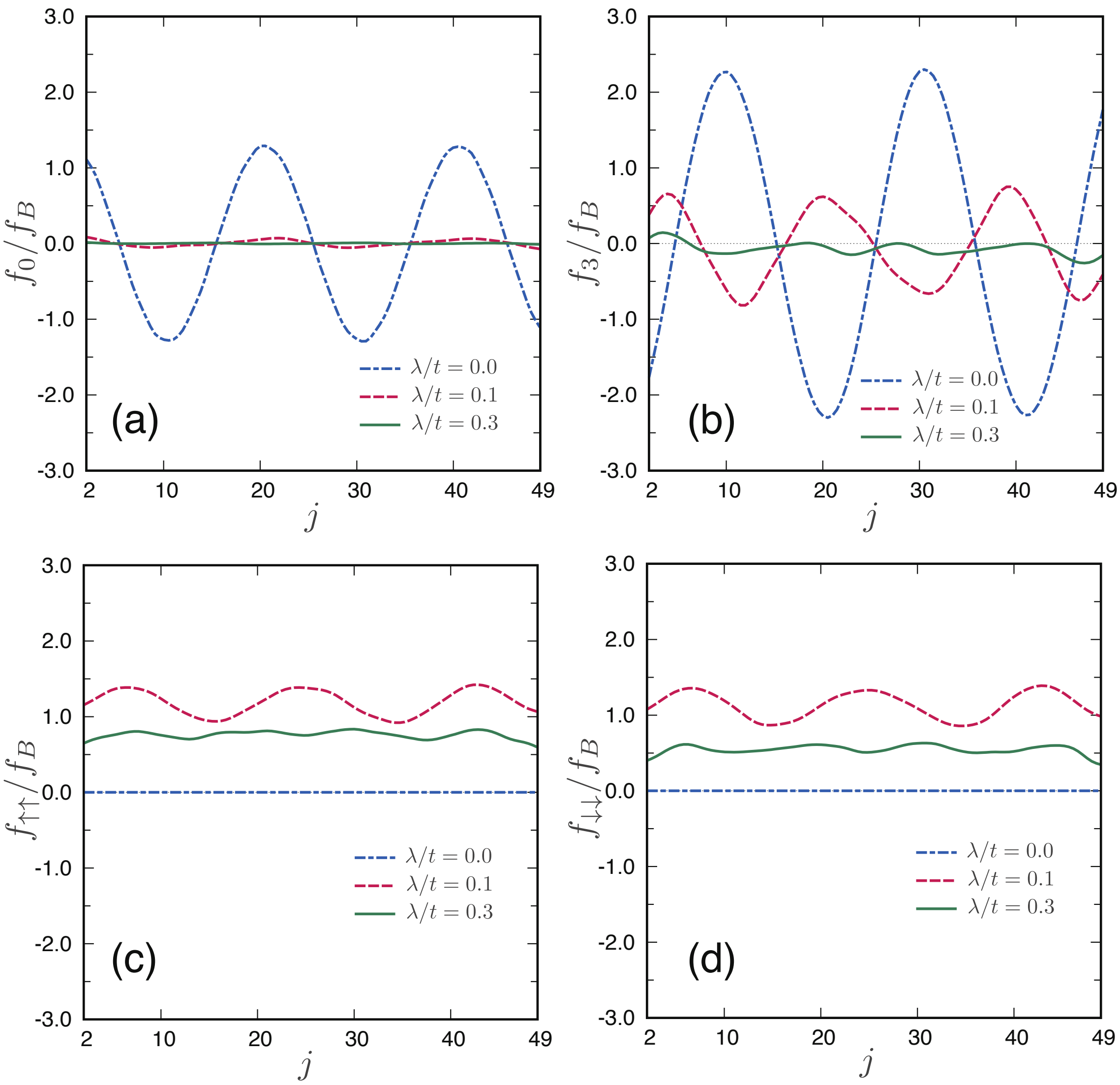

Figure 5.5: The results for an odd-parity symmetry in Eq. (5.15). The parameters are the same with those in Fig. 5.4. (a) spin-singlet f_0, (b) opposite-spin-triplet f_3, (c) equal-spin-triplet $f_{\uparrow\uparrow}$, and (c) equal-spin-triplet $f_{\downarrow\downarrow}$

result, f_0 is positive at any place for $\lambda = 0.3t$. The opposite-spin-triplet component f_3 in (b) always changes its sing but is strongly suppressed by the spin-orbit interactions. We note that f_3 belongs to odd-frequency spin-triplet even-parity (OTE) symmetry class. The two equal-spin-triplet components in (c) and (d) are absent irrespective of λ. The analytical results of the Eilenberger equation predict these behavior well.

In Fig. 5.5, we display the spatial profile of the odd-parity components in Eq. (5.15) for several choices of λ. At $h = 0$ and $\lambda = 0$, the junction becomes an SNS junction and odd-parity components are absent in its normal segment. In the presence of the exchange potential, however, odd-parity opposite-spin Cooper pairs are generated in the

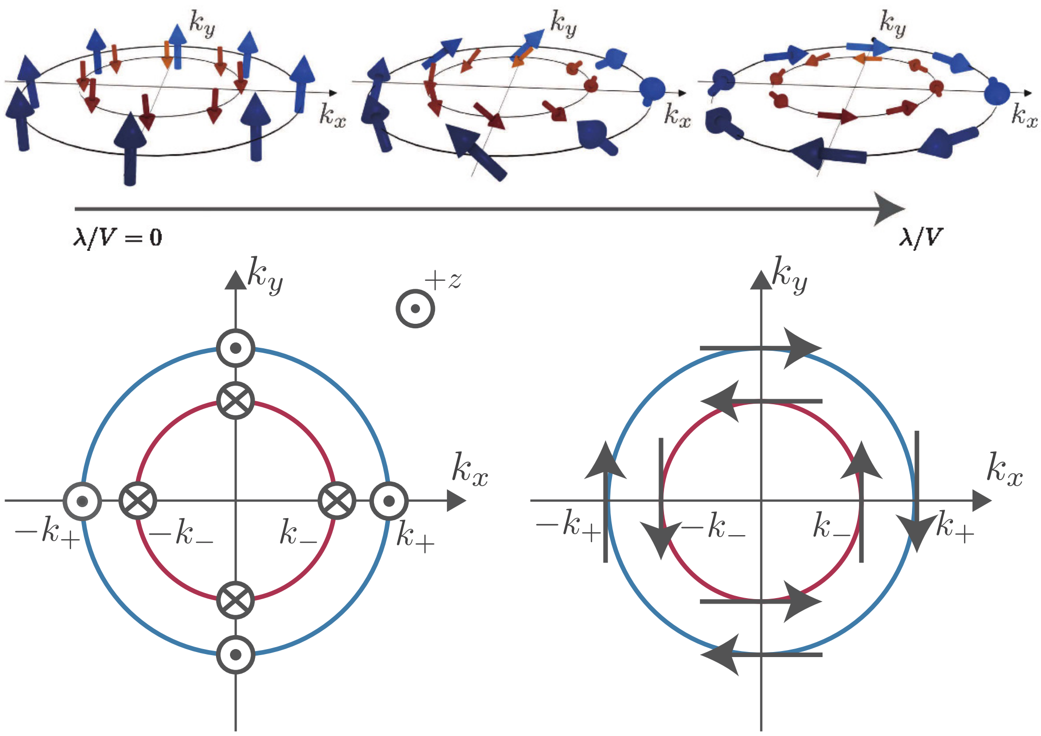

Figure 5.6: Schematic picture of spin-configuration on the Fermi surface. In Upper figure, the spins of an electron in the spin $\uparrow$ band are twisted by the spin-orbit interactions. The strong spin-orbit interaction fells spins down to a two-dimensional plane. In lower figure, spin configuration on the two Fermi surface are shown for the two limits: $h \gg \lambda$ on the left panel and $h \ll \lambda$ on the right panel.

clean junction because the exchange potential breaks inversion symmetry locally at the junction interface. The spin-singlet s-wave component f_0 in (a) oscillates and changes its sign in real space at $\lambda = 0$. The spin-orbit interactions suppresses drastically such an odd-frequency spin-singlet odd-parity (OSO) component. The opposite-spin-triplet component f_3 in (b) belongs to even-frequency spin-triplet odd-parity (ETO) class shows similar behavior to f_0. Finally, the spin-orbit interactions generate two equal-spin-triplet components $f_{\uparrow\uparrow}$ and $f_{\downarrow\downarrow}$ as shown in (c) and (d), respectively. They oscillate slightly in real space but do not change their sign. The amplitude of such odd-parity equal spin components first increases with the increase of λ then decrease in agreement with the analytical results in Eqs. (5.26) and (5.28). The spin-momentum locking due to the spin-orbit interaction explains such behaviors as we discuss in what follows.

Figure 5.6 shows the schematic spin structure on the Fermi surfaces. When the exchange potential is much larger than the spin-orbit interactions, spin of an electron aligns in each spin bands. The spin-orbit interactions twists the spin structure as shown in the upper middle figure. The strong spin-orbit interactions causes the spin-momentum locking as shown in the upper right figure. The spin configuration in the two limits are shown in the lower figure. The wavenumber $k_\pm$ in the figure are $k_\pm = k_F \pm h/v_F$ in the limit of $h \gg \lambda$ on the left and $k_\pm = k_F \pm \lambda/v_F$ in the limit of $h \ll \lambda$ on the right. At $h \gg \lambda$, a spin-singlet pair and an opposite-spin-triplet pair have a center-of-mass-momentum of $k_+ + (-k_-) = 2h/v_F$ on the Fermi surface. As a result, these components oscillate and change their signs in real space [127, 128]. On the other hand, equal-spin-triplet components $f_{\uparrow\uparrow}$ ($f_{\downarrow\downarrow}$) do not have a center-of-mass-momentum because they consist of two electrons at $\pm k_+$ ($\pm k_-$). Thus equal-spin-triplet components do not change signs as shown in the results for $\lambda = 0.1t$ in Fig. 5.5 (c) and (d).

In the opposite limit of $h \ll \lambda$, a spin-singlet Cooper pair does not have a center-of-mass-momentum in this case. The spin-momentum locking due to strong spin-orbit interactions stabilizes such a Cooper pair consisting of two electrons of time-reversal partners. Thus a spin-singlet Cooper pair does not oscillate in real space as shown in the results for $\lambda = 0.3t$ in Fig. 5.4(a). Equal-spin-triplet pairs, on the other hand, have the center-of-mass-momentum $2\lambda/v_F$. In Fig. 5.5 (c) and (d), $f_{\sigma\sigma}$ for $\lambda = 0.1t$ oscillate in real space. Since the spacial oscillations cost the energy, $f_{\sigma\sigma}$ for $\lambda = 0.3t$ is smaller than that for $\lambda = 0.1t$.

In the limit of $\lambda \gg h$, a spin-singlet Cooper pair is dominant in a ferromagnet and carries the Josephson current. The pairing function f_0 in Fig. 5.4 (a) does not changes sign. As a result, the 0 state is stable than the π state for $\lambda > h$ as shown in Fig. 5.3.

5.3.3 Josephson current in dirty limit

In the dirty limit, we switch on the random impurity potential in Eq. (5.7) in a ferromagnet, where the potential is given randomly in the range of $-V_{\text{imp}}/2 \leq v_{\boldsymbol{r}} V_{\text{imp}}/2$. In the numerical simulation, we set $V_{\text{imp}} = 2t$, which results in the mean free path ℓ about five lattice constants. Since $\ell \ll L$, a ferromagnet is in the diffusive transport regime. The coherence length $\xi_0 = v_F/\pi\Delta$ is estimated as twenty lattice constants at $\Delta = 0.005t$. Thus the junction is in the dirty regime because of $\ell < \xi_0$. The Josephson current is first calculated for a single sample with a specific random impurity configuration. Then the results are averaged over N_{s} samples with different impurity configurations,

$$\langle J \rangle = \frac{1}{N_{\text{s}}} \sum_{i=1}^{N_{\text{s}}} J_i. \tag{5.30}$$

In this chapter, we choose N_{s} as 100-500 in numerical simulation.

In Fig. 5.7, we show the ensemble average of the Josephson current as a function of the length of the ferromagnet, where we fix $\varphi = 0.5\pi$, the exchange potential is absent in (a) and the exchange potential is $h = 0.5t$ in (b). We confirmed that the current-phase

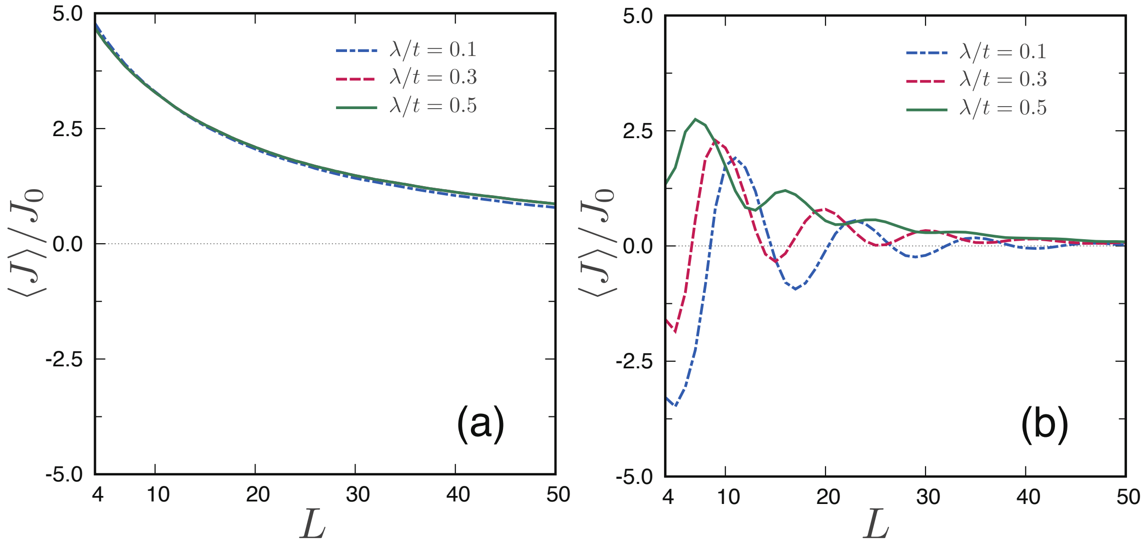

Figure 5.7: The Josephson current versus the length of a normal segment L in the dirty limit. (a): an SNS junction at $h = 0$. (b): an SFS junction at $h = 0.5t$. The parameters here are the same as those in Fig. 5.2

relationship of ensemble aberaged Josephson current is sinusoidal. The decay length of the Josephson current in Fig. 5.7(a) is shorter than that in the clean limit in Fig. 5.2(a). It is well known in a diffusive normal metal that, the penetration length of a Cooper pairs is limited by $\xi_T^D = \sqrt{D/2\pi T}$. The Josephson current is almost free from spin-orbit interactions. The results of a SFS junction in Fig. 5.7(b) shows the oscillations and the sign change of the Josephson current at $\lambda = 0.1t$. The large spin-orbit interaction suppresses the sign change of the Josephson current as show in the result for $\lambda = 0.3t$. In Fig. 5.8, we plot the ensemble average of Josephson current at $\varphi = 0.5\pi$ as a function of h and λ. The results should be compared with those in Fig. 5.3. The amplitude of the Josephson current is suppressed by the impurity scatterings. Although the 0-π transition can be seen at $\lambda = 0$, the spin-orbit interaction suppresses the 0-π transition. Such tendency is common in Figs. 5.3 and 5.8.

In the presence of impurities, however, the current-phase relation in a single sample deviates from the sinusoidal function as

$$J_i = J_c \sin(\varphi - \varphi_i), \tag{5.31}$$

where φ_i is the phase shift depends on the random impurity configuration. In experiments, the Josephson current is measured in a specific sample of SFS junction. Since the Josephson effect is a result of the phase coherence of a quasiparticle developing over a ferromagnet, the Josephson current is not a self-averaged quantity. Therefore, the Josephson current calculated at a single sample J_i corresponds to that at a single measurement in experiments. When the behavior of $\langle J \rangle$ and that of J_i are different qualitatively from each

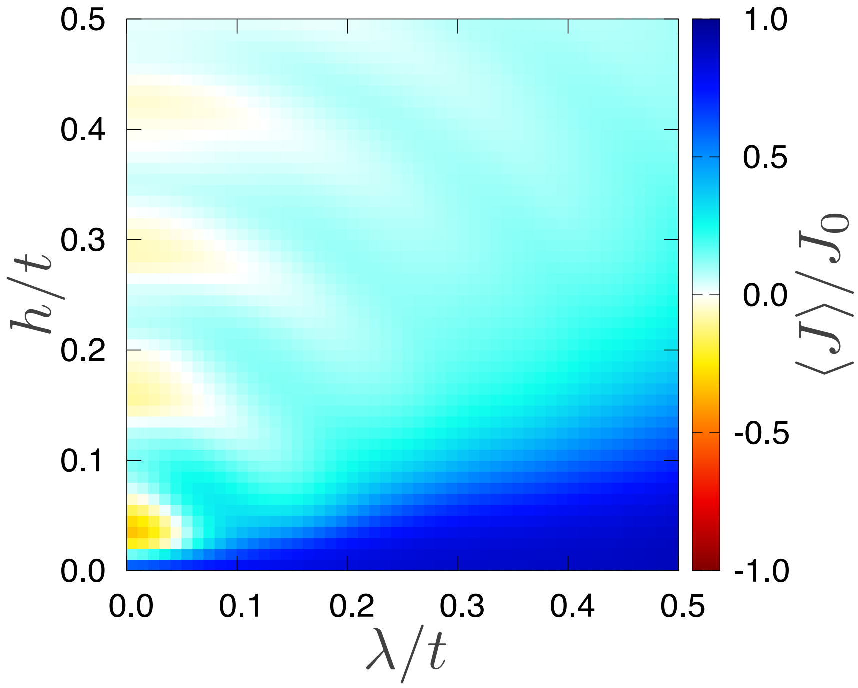

Figure 5.8: The Josephson current is plotted as a function of h and λ in the dirty regime. The parameters are the same as those in Fig. 5.3.

other, $\langle J\rangle$ cannot predict a Josephson current measured in experiments [125]. Therefore, $\langle J\rangle$ in Fig. 5.8 tell us only a tendency of φ_i value. Namely, $\varphi_i \approx 0$ would be expected in experiments for $\lambda \gg h$. A previous paper [117] has discussed that the phase shift in the current-phase relationship φ_0 is tunable by applying the Zeeman field in the y direction. The argument is valid only when a normal segment of a junction is in the ballistic transport regime and a junction geometry is symmetric under $y \to -y$.

5.3.4 Pairing functions in dirty limit

Although the ensemble average of the Josephson current in theories cannot predict the current-phase relationship measured in a real sample, the ensemble average of the pairing functions tells us characteristic features of the proximity effect. In Fig. 5.9, we show the spatial profile of the pairing functions in dirty regime, where $\varphi = 0$, $h_z = 0.5t$ and $L = 50$. The parameters here are the same as those in Fig. 5.4. The singlet component $\langle f_0\rangle$ oscillates and changes its sign at $\lambda = 0$ as shown in Fig. 5.9(a). At $\lambda = 0.5t$, the spin-orbit interaction surpress the amplitude of oscillations. The similar tendency can be found also in the opposite-spin-triplet component $\langle f_3\rangle$ in (b). The equal-spin-triplet components $\langle f_{\sigma\sigma}\rangle$ are zero at $\lambda = 0$. The amplitudes of such OTE pairs become finite and spatially uniform in the dirty regime as shown in in Fig. 5.9(c) and (d).

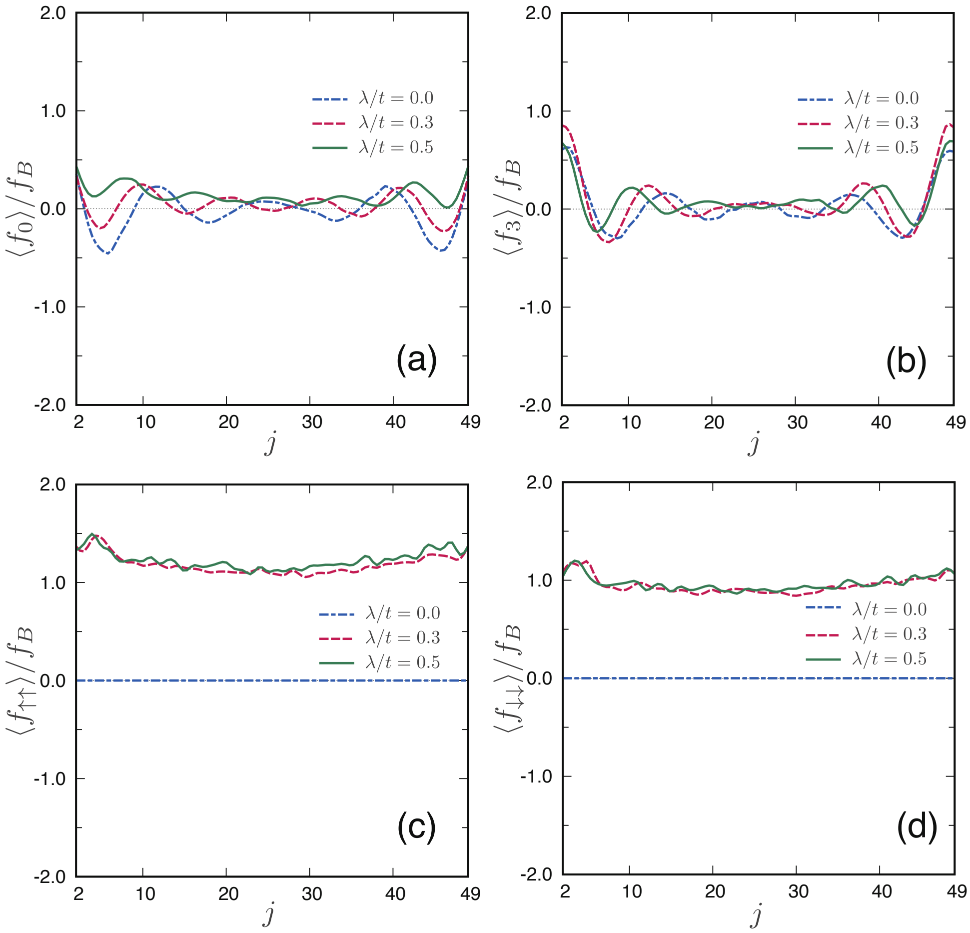

Figure 5.9: The spatial profile of the ensemble average of pairing function in the dirty regime. Only an s-wave component remains finite in the dirty regime. The parameters are the same as those in Fig. 5.4.

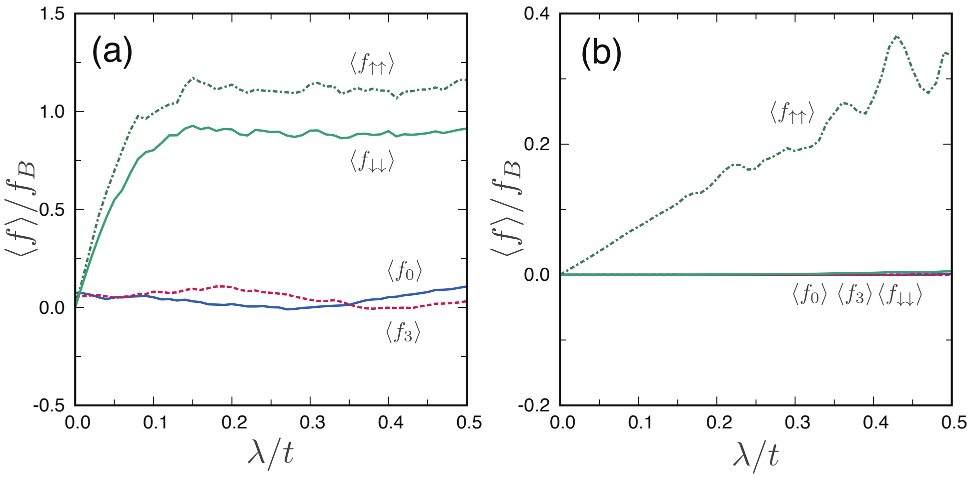

Figure 5.10: The pairing functions at the center of a ferromagnet $j = 25$ are shown as a function of λ. (a): a strong ferromagnet at $h = 0.5t$. (b): a half-metallic ferromagnet at $h = 2.5t$.

In the clean limit, the spin-momentum locking suppresses the equal-spin-triplet components as shown in Figs. 5.4 (c) and (d). In the dirty regime, however, the momentum is not a good quantum number. Equal-spin OTE pairs have the long-range property because random impurity scatterings release the spin-momentum locking.[119, 120] At $\lambda > gh$, the results in Fig. 5.9 show that the most dominant pair in a ferromagnet belongs odd-frequency equal-spin-triplet s-wave symmetry class.

We fix $j = 25$ in Fig. 5.9 at a center of a ferromagnet and calculate the pairing functions as a function of λ. The results are presented in Fig. 5.10, where we choose $h = 0.5t$ in (a) and $h = 2.5t$ in (b). The pairing functions for opposite-spin pair $\langle f_0 \rangle$ and $\langle f_3 \rangle$ are insensitive to spin-orbit interactions. The amplitude of equal-spin pairs $\langle f_{\sigma\sigma} \rangle$ increases with the increase of λ and saturate for $\lambda > 2.0t$ in (a). Thus odd-frequency long-range components are dominant in a strong ferromagnet. When we increase the exchange potential to $h = 2.5t$ in (b), a ferromagnet becomes half-metallic. Namely the ferromagnet is metallic for a spin-$\uparrow$ electron and is insulating for a spin-$\downarrow$ electron. In such a half-metal, only $\langle f_{\uparrow\uparrow} \rangle$ component survives and carries the Josephson current, which is very similar to the situation discussed in the previous papers. [108, 107, 109].

5.4 Summary

In summary, we have theoretically examined the proximity effect in a ferromagnetic semiconductor with Rashba spin-orbit interaction by solving the Gor'kov equation on a two-dimensional tight-binding lattice. Our findings reveal that the interplay between the exchange potential and spin-orbit interaction enriches the symmetry landscape of Cooper pairs. Specifically, the exchange potential in the ferromagnet converts spin-singlet Cooper pairs into opposite-spin-triplet pairs, while strong spin-orbit interaction generates equal-spin-triplet pairs in the clean regime.

Notably, we identified that the dominant pairing symmetry depends on the transport regime: in the clean limit, spin-momentum locking stabilizes conventional spin-singlet s-wave pairs, whereas in the dirty regime, odd-frequency equal-spin-triplet s-wave pairs become dominant due to impurity scattering. This shift underscores the significant role of disorder in releasing spin-momentum constraints.

These results not only deepen our understanding of superconducting proximity effects in materials with complex spin-orbit interactions but also suggest potential route for inducing spin-triplet superconductivity in hybrid structures. Future work could extend these insights by exploring the impact of additional spin-textured states or multilayered structures, offering a richer framework for spin-polarized supercurrent applications.

Chapter **6**

Conclusding Remarks

We have theoretically studied the effects of spin-orbit interactions (SOI) on the low-energy transport properties in two-dimensional dirty normal metal/superconductor (NS) junctions. In this thesis, we considered spin-singlet s-wave, d_{xy}-wave, and $d_{x^2-y^2}$-wave pair potentials in superconductors. However, spin-triplet Cooper pairs dominate the low-energy transport properties. Spin-orbit interactions generate such spin-triplet Cooper pairs from spin-singlet Cooper pairs which form the pair potential. In this thesis, we consider three types of SOI: x-type, y-type, and Rashba SOI. In spintronics, x-type and y-type SOI have been a persistent spin helix state

In chapters 2-4, we discuss the anomalous proximity effect in a normal-metal / superconductor (NS) junction. As discussed in chpater 1 and chapter 2, a topological invariant called Atiyah-Singer index N_{ZES} well characterizes the anomalous proximity effect. Indeed, the minimum of the zero-bias conductance is limited by $(2e^2/h)\, N_{\mathrm{ZES}}$ independent of the degree of disorder in the normal metal and the transparency of the junction interface. The index can be defined when the Bogoliubov-de Gennes Hamiltonian preserves chiral symmetry. Previous theoretical studies showed that N_{ZES} is zero in spin-singlet superconductors in the absence of SOI. In this thesis, we show that the appropriate SOI in a spin-singlet superconductor makes the index a nonzero value.

In chapters 2-3, we consider spin-singlet d_{xy} superconductor in an NS junction, where electric current flows in the x direction. A number of zero-energy states appear at a clean surface of a d_{xy} superconductor. However, the potential disorder in the normal metal lifts the high degeneracy at zero energy, which results in $N_{\mathrm{ZES}} = 0$ meaning the absence of the anomalous proximity effect. The y-type SOI relax such severe situation. In chapter 2, we analytically show that the y-type SOI generates spin-triplet p_x-wave Cooper pairs. In addition, y-type SOI breaks the chiral balance of the zero-energy states, which leads to $N_{\mathrm{ZES}} \neq 0$. In chapter 3, we check the validity of such prediction by numerical simulations, where the conductance of an NS junction is calculated based on the Blonder-Tinkham-Klapwijk formula. The numerical results show the quantization of the conductance minimum in agreement with the theoretical prediction.

In chapter 4, we consider spin-singlet s-wave and spin-singlet $d_{x^2-y^2}$ symmetries in a superconductor motivated by recent experiments suggesting the anomalous proximity effect. In both cases, zero-energy states are absent at a clean surface of a superconductor. We show that x-type SOI generates spin-triplet p_x-wave Cooper pairs and causes the anomalous proximity effect in a spin-singlet $d_{x^2-y^2}$ junction. In a spin-singlet s-wave superconductor junction, however, the proximity effect is always absent even in the presence of strong SOIs. Our numerical simulation on the conductance of an NS junction justifies the validity of the theoretical prediction.

The anomalous proximity effect is understood as a result of the penetration of zero-energy states at a surface of a superconductor into a dirty normal metal with retaining high degeneracy. Simultaneously, it is possible to say that the penetration of odd-frequency Cooper pairs into a dirty normal metal causes the anomalous proximity effect. The existence of odd-frequency Cooper pairs has attracted much attention in a superconductor/ferromagnet/superconductor junction, where superconductors belong to conventional spin-singlet s-wave symmetry class and the exchange potential in a diffusive ferromagnet is much larger than the pair potential. When the length of a ferromagnet is long enough, spin-singlet Cooper pairs no longer carry Josephson current. Several experiments have suggested the existence of spin-triplet Cooper pairs in a ferromagnet. In chapter 5, we discuss how SOIs cause the symmetry conversion of Cooper pairs between spin-singlet and spin-triplet. We also discuss how potential disorder suppress the variety in the pairing symmetry in a ferromagnet. Our numerical simulation shows that only odd-frequency Cooper spin-triplet s-wave Cooper pair carry the Josephson current in a dirty limit.

Although spin-triplet Cooper pairs cause very unusual phenomena, spin-triplet superconductors are very rare. In this thesis, we provide designs for artificial spin-triplet superconductors by combining existing materials and experimentally accessible technologies. The specific type of spin-orbit interaction plays a central role in the symmetry conversion of Cooper pairs. Our findings indicate an alternative route for investigating spin-triplet superconductivity and its topological properties.

Appendix A

Surface Andreev bound states

The BdG Hamiltonian on a two-dimensional tight-binding lattice is represented by

$$\mathcal{H} = \sum_{\boldsymbol{r},\boldsymbol{r}'} \left[\psi^\dagger_{\boldsymbol{r},\uparrow}, \psi^\dagger_{\boldsymbol{r},\downarrow}, \psi_{\boldsymbol{r},\uparrow}, \psi_{\boldsymbol{r},\downarrow}\right] \check{H}_{\mathrm{BdG}}(\boldsymbol{r},\boldsymbol{r}') \left[\psi_{\boldsymbol{r}',\uparrow}, \psi_{\boldsymbol{r}',\downarrow}, \psi^\dagger_{\boldsymbol{r}',\uparrow}, \psi^\dagger_{\boldsymbol{r}',\downarrow}\right]^{\mathrm{T}} \tag{A.1}$$

where $\psi_{\boldsymbol{r},\sigma}$ is the annihilation operator of an electron at $\boldsymbol{r} = j\hat{\boldsymbol{x}} + m\hat{\boldsymbol{y}}$ with with $\hat{\boldsymbol{x}}$ ($\hat{\boldsymbol{y}}$) being unit vector in the $\boldsymbol{x}$ ($\boldsymbol{y}$) direction, $\sigma =\uparrow$ or $\downarrow$ indicates spin of an electron, and T represents the transpose of a matrix. The BdG Hamiltonian for an equal spin-triplet p_x-wave superconductor can be represented as

$$\check{H}_{p_x}(\boldsymbol{r},\boldsymbol{r}') = H_t(\boldsymbol{r},\boldsymbol{r}')\hat{\tau}_3 + \hat{H}_{\Delta_p}(\boldsymbol{r},\boldsymbol{r}')\,\hat{\sigma}_3\,\hat{\tau}_1, \tag{A.2}$$

$$H_t(\boldsymbol{r},\boldsymbol{r}') = -t\left[\delta_{\boldsymbol{r},\boldsymbol{r}'+\hat{\boldsymbol{x}}} + \delta_{\boldsymbol{r},\boldsymbol{r}'-\hat{\boldsymbol{x}}} + \delta_{\boldsymbol{r},\boldsymbol{r}'+\hat{\boldsymbol{y}}} + \delta_{\boldsymbol{r},\boldsymbol{r}'-\hat{\boldsymbol{y}}}\right]\hat{\sigma}_0 + \delta_{\boldsymbol{r},\boldsymbol{r}'}\,(4t - \epsilon_F)\,\hat{\sigma}_0, \tag{A.3}$$

$$H_{\Delta_p} = \frac{\Delta}{2i}\left[\delta_{\boldsymbol{r},\boldsymbol{r}'+\hat{\boldsymbol{x}}} - \delta_{\boldsymbol{r},\boldsymbol{r}'-\hat{\boldsymbol{x}}}\right], \tag{A.4}$$

where τ_j and σ_j for $j = 1-3$ are the Pauli's matrices in particle-hole space and those in spin space, respectively. The unit matrix in these spaces are $\hat{\tau}_0$ and $\hat{\sigma}_0$. The pair potential and the hopping integral are denoted by Δ and t, respectively. We calculate the eigenvalues of $\hat{H}_{p_x}$ under the hard wall boundary condition in the x direction and the periodic boundary condition in the y direction. The results for $\epsilon_F = 2t$ and $\Delta = t$ are plotted as a function of k_y in Fig. A.1(a). The symbols for $E \neq 0$ represent eigenvalues of bulk states. At the present parameter choice, the superconducting gap has two nodes at $k_y = \pm k_F$ with $k_F = \pi/2$. The ZESs between the nodes in Fig. A.1(a) localize at a surface. The wave function of the ZESs near $x = 0$ are described by

$$\phi_{p_x,-}(\boldsymbol{r}) = \begin{bmatrix} 1 \\ 1 \\ i \\ -i \end{bmatrix} f_{k_y}(\boldsymbol{r}), \quad \phi_{p_x,+}(\boldsymbol{r}) = \begin{bmatrix} -1 \\ 1 \\ i \\ i \end{bmatrix} f_{k_y}(\boldsymbol{r}), \quad f_{k_y}(\boldsymbol{r}) = A\, e^{ik_y y} e^{-x/\xi_0}\, \sin k_x x, \tag{A.5}$$

where $\xi_0 = v_F/\Delta$ and A is a constant. It is easy to confirm that $\check{\Gamma}_{\mathrm{BIII}}\,\phi_\pm = \pm\phi_\pm$. As a result, we find $N_+ = N_-$ and $\mathcal{N}_{\mathrm{ZES}} = 0$ in consistent with the prediction. [39]

The wave functions of the ZESs in Eq. (A.5) are described alternatively as

$$\phi_{p_x,\uparrow}(\boldsymbol{r}) = \begin{bmatrix} 1 \\ 0 \\ i \\ 0 \end{bmatrix} f_{k_y}(\boldsymbol{r}), \quad \phi_{p_x,\downarrow}(\boldsymbol{r}) = \begin{bmatrix} 0 \\ 1 \\ 0 \\ -i \end{bmatrix} f_{k_y}(\boldsymbol{r}), \tag{A.6}$$

where $\phi_{p_x,\sigma}$ the the wave function in spin σ sector. It is easy to confirm that $\check{\Gamma}_{\mathrm{BDI}}\,\phi_\sigma = \phi_\sigma$ holds for both $\sigma =\uparrow$ and $\downarrow$. Therefore we find $N_+ = N_c$ and $N_- = 0$, which results in $\mathcal{N}_{\mathrm{ZES}} = N_c$ as long as $\{\check{H}_{p_x}, \check{\Gamma}_{\mathrm{BDI}}\} = 0$.

The eigenvalues of the BdG Hamiltonian of a d_{xy}-wave superconductor,

$$\check{H}_{d_{xy}}(\boldsymbol{r},\boldsymbol{r}') = H_t(\boldsymbol{r},\boldsymbol{r}')\hat{\tau}_3 + H_{\Delta_d}(\boldsymbol{r},\boldsymbol{r}')\,\hat{\sigma}_2\,\hat{\tau}_2, \tag{A.7}$$

$$H_{\Delta_d}(\boldsymbol{r},\boldsymbol{r}') = \frac{\Delta}{2}\left[\delta_{\boldsymbol{r},\boldsymbol{r}'+\hat{\boldsymbol{x}}+\hat{\boldsymbol{y}}} + \delta_{\boldsymbol{r},\boldsymbol{r}'-\hat{\boldsymbol{x}}-\hat{\boldsymbol{y}}} - \delta_{\boldsymbol{r},\boldsymbol{r}'+\hat{\boldsymbol{x}}-\hat{\boldsymbol{y}}} - \delta_{\boldsymbol{r},\boldsymbol{r}'-\hat{\boldsymbol{x}}+\hat{\boldsymbol{y}}}\right], \tag{A.8}$$

are shown in Fig. A.1(b). There are three nodal points at $k_y = 0$ and $\pm k_F$. A surface Andreev bound state appears for each propagating channel on the Fermi surface. The wave functions of the ZESs are described by

$$\phi_{d_{xy},+}(\boldsymbol{r}) = \begin{bmatrix} 1 \\ -1 \\ i\,s_k \\ i\,s_k \end{bmatrix} f_{k_y}(\boldsymbol{r}), \quad \phi_{d_{xy},-}(\boldsymbol{r}) = \begin{bmatrix} 1 \\ 1 \\ -i\,s_k \\ i\,s_k \end{bmatrix} f_{k_y}(\boldsymbol{r}), \quad s_k = \mathrm{sgn}(k_y), \tag{A.9}$$

It is easy to confirm that $\check{\Gamma}_{\mathrm{BDI}}\,\phi_{d_{xy},\pm} = \pm s_k\,\phi_{d_{xy},\pm}$ hold. The chiral eigenvalues of ZESs depend on the sign of k_y in a d_{xy}-wave superconductor. As displayed in Fig. A.1(b), the number of the ZESs at $k_y > 0$ is equal to that at $k_y < 0$. Although $\check{H}_{d_{xy}}$ anticommutes to $\check{\Gamma}_{\mathrm{BDI}}$, the index $\mathcal{N}_{\mathrm{ZES}}$ is always zero in the absence of spin-orbit interactions. The Hamiltonian $\check{H}_{d_{xy}}$ anticommutes also to another chiral operator $\hat{\tau}_1$. We, however, find that $\mathcal{N}_{\mathrm{ZES}} = 0$ in terms of the chiral eigen values of $\hat{\tau}_1$.

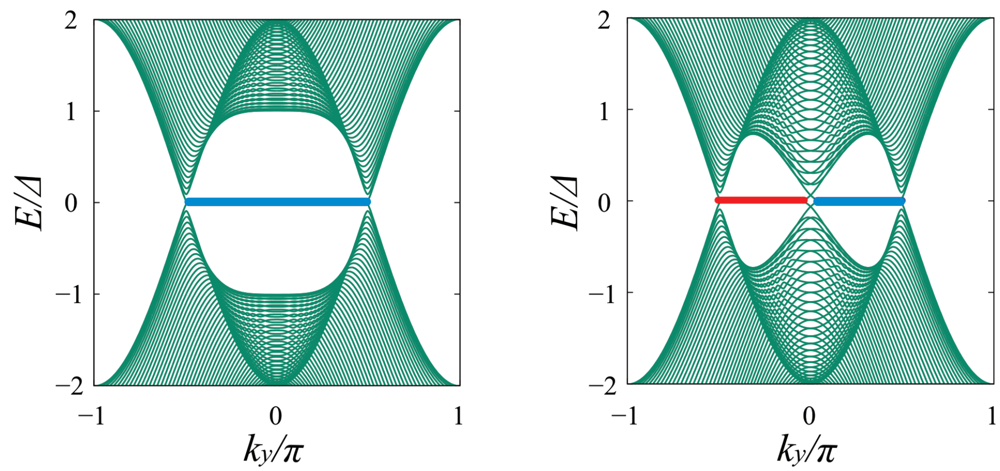

(a) $\mathrm{p_x}$ -wave

(b) $\mathrm{d_{xy}}$ -wave

Figure A.1: The eigenvalues of the BdG Hamiltonian on a two-dimensional tight-binding model are plotted as a function of the wave number in the y direction. The results for a p_x-wave superconductor in (a) have nodes at $k_y = \pm k_F$ with $k_F = \pi/2$. The surface Andreev bound states are degenerate at $E = 0$ as indicated by a line between the two nodal points. All of the ZESs belong to the same chiral eigenvalue of $\check{\Gamma}_{\mathrm{BDI}}$. In (b), the results for a d_{xy}-wave superconductor are shown. An additional nodal point appears at $k_y = 0$. ZESs for $k_y > 0$ and those for $k_y < 0$ belong to the opposite chiral eigenvalue of $\check{\Gamma}_{\mathrm{BDI}}$.

Appendix B

Green's function in real space

The solution of the Gor'kov equation in Eq. (2.36) is obtained as

$$\hat{G}_\epsilon(\boldsymbol{k}) = \left[(\epsilon - \hat{H}_{\mathrm{N}}) + \hat{\Delta}\,(\epsilon + \underset{\sim}{\hat{H}}_{\mathrm{N}})^{-1}\,\underset{\sim}{\hat{\Delta}}\right]^{-1}, \quad \hat{F}_\epsilon(\boldsymbol{k}) = \left[\underset{\sim}{\hat{\Delta}} + (\epsilon + \underset{\sim}{\hat{H}}_{\mathrm{N}})\,\hat{\Delta}^{-1}\,(\epsilon - \hat{H}_{\mathrm{N}})\right]^{-1}. \tag{B.1}$$

The retarded Green's function for H_1 is represented as

$$\hat{G}_\epsilon(\boldsymbol{r}-\boldsymbol{r}') = \frac{1}{W}\sum_{k_y} e^{ik_y(y-y')}\hat{G}_\epsilon(x-x'), \quad \hat{F}_\epsilon(\boldsymbol{r}-\boldsymbol{r}') = \frac{1}{W}\sum_{k_y} e^{ik_y(y-y')}\hat{F}_\epsilon(x-x'), \tag{B.2}$$

with

$$\hat{G}_\epsilon(x-x') = \frac{1}{2\pi}\int_{-\infty}^{\infty} dk\, e^{ik(x-x')}\frac{1}{2}\left[\frac{(\epsilon+\xi_{1,+})(1+\hat{\sigma}_1)}{(\epsilon+i\delta)^2 - E_{1,+}^2} + \frac{(\epsilon+\xi_{1,-})(1-\hat{\sigma}_1)}{(\epsilon+i\delta)^2 - E_{1,-}^2}\right], \tag{B.3}$$

$$\hat{F}_\epsilon(x-x') = \frac{1}{2\pi}\int_{-\infty}^{\infty} dk\, e^{ik(x-x')}\frac{\Delta_{\boldsymbol{k}}}{2}\left[\frac{1-\hat{\sigma}_1}{(\epsilon+i\delta)^2 - E_{1,-}^2} + \frac{1+\hat{\sigma}_1}{(\epsilon+i\delta)^2 - E_{1,+}^2}\right] i\hat{\sigma}_2. \tag{B.4}$$

To proceed the calculation, it is necessary to carry out the integration

$$I_{1,\pm} = \frac{1}{2\pi}\int_{-\infty}^{\infty} dk\, e^{ik(x-x')}\,\frac{f(k,\xi_{1,\pm})}{(\epsilon+i\delta-E_{1,\pm})(\epsilon+E_{1,\pm})}, \tag{B.5}$$

where f is an analytic function. For $\epsilon > 0$, $(\epsilon+E_{1,\pm})^{-1}$ is analytic, whereas $(\epsilon+i\delta-E_{1,\pm})^{-1}$ has two poles at $k = k_\pm^e + i0^+$ and $k = -k_\pm^h + i0^+$ with

$$k_\pm^e = \left[p_{1\pm}^2 + \frac{2m}{\hbar^2}\Omega\right]^{1/2}, \quad k_\pm^h = \left[p_{1\pm}^2 - \frac{2m}{\hbar^2}\Omega\right]^{1/2}, \quad \Omega = \sqrt{(\epsilon+i\delta)^2 - \Delta_{\boldsymbol{k}}^2} \tag{B.6}$$

where $p_{1\pm}$ is defined in Eq. (2.21). Paying attention to the relations $\xi_{1,\pm} \to \Omega$ at $k = k_\pm^e$ and $\xi_{1,\pm} \to -\Omega$ at $k = -k_\pm^h$, $\epsilon + i\delta - E_{1,\pm}$ at the denominator of Eq. (B.5) can be expanded around $k = k_\pm^e$ as

$$\epsilon + i\delta - E_{1,\pm}(k) \approx \epsilon - E_{1,\pm}(k_\pm^e) + i\delta - \frac{\xi_{1,\pm}}{E_{1,\pm}(k_\pm^e)}\frac{\hbar^2 k_\pm^e}{m}(k - k_\pm^e) = -\frac{\Omega}{\epsilon}\frac{\hbar^2 k_\pm^e}{m}(k - k_\pm^e - i\delta'). \tag{B.7}$$

Around a pole of $k = -k^h_\pm$, the $\epsilon + i\delta - E_{1,\pm}$ becomes

$$\epsilon + i\delta - E_{1,\pm}(k) \approx \epsilon - E_{1,\pm}(-k^h_\pm) + i\delta - \frac{\xi_{1,\pm}}{E_{1,\pm}(-k^h_\pm)} \frac{-\hbar^2 k^h_\pm}{m}(k + k^h_\pm) \tag{B.8}$$

$$= -\frac{-\Omega}{\epsilon}\frac{(-\hbar^2 k^h_\pm)}{m}(k + k^h_\pm - i\delta'). \tag{B.9}$$

By picking up the residues of these poles, the integral in Eq. (B.5) is calculated as

$$I_{1,\pm} = -i\frac{m}{2\Omega\hbar^2}\left[\frac{f(s_x k^e_\pm, \Omega)}{k^e_\pm} e^{ik^e_\pm|x-x'|} + \frac{f(-s_x k^h_\pm, -\Omega)}{k^e_\pm} e^{-ik^h_\pm|x-x'|}\right]\Theta(p^2_{1\pm}), \tag{B.10}$$

$$s_x = \mathrm{sgn}(x - x'). \tag{B.11}$$

where we consider the contribution from the propagating channels as indicated by a factor $\Theta(p^2_{1\pm})$. The integral on the upper-half complex plane converges for $x - x' > 0$. On the other hand for $x - x' < 0$, the transformation of $k \to -k$ is necessary, which produces a factor of s_x. In the text, we mainly discuss the Green's function for $0 < \epsilon \ll \Delta$. In such case, it is possible to apply an approximation for the wavenumber $k^e_\pm = p_{1\pm} + iq_x$ and $k^h_\pm = p_{1\pm} - iq_x$ with $q_x = (\Delta/\hbar v_F)\bar{k}_y$. We also apply $p_{1+} \approx p_{1-} \approx p_x = \sqrt{k_F^2 - k_y^2 + 2\alpha k_F|k_y|}$ because the amplitude of the wavenumber is not important for analyzing the pairing symmetry. By the same reason, we consider q_x only in the exponential function. The integral under these approximations is represented as

$$I_{1,\pm} \approx -i\frac{m}{2\Omega\hbar^2}e^{-q_x|x-x'|}\left[\frac{f(s_x p_x, \Omega)}{p_x}e^{ip_x|x-x'|} + \frac{f(-s_x p_x, -\Omega)}{p_x}e^{-ip_x|x-x'|}\right]\Theta(p^2_{1\pm}). \tag{B.12}$$

The normal Greens's function in Eq. (B.3) is calculated as

$$\begin{aligned} G_\epsilon(x - x') = & -i\frac{m}{4\Omega\hbar^2}e^{-q_x|x-x'|}\left[\frac{\epsilon+\Omega}{p_x}e^{ip_x|x-x'|} + \frac{\epsilon-\Omega}{p_x}e^{-ip_x|x-x'|}\right](1 + \hat{\sigma}_1)\Theta(p^2_{1+}) \\ & -i\frac{m}{4\Omega\hbar^2}e^{-q_x|x-x'|}\left[\frac{\epsilon+\Omega}{p_x}e^{ip_x|x-x'|} + \frac{\epsilon-\Omega}{p_x}e^{-ip_x|x-x'|}\right](1 - \hat{\sigma}_1)\Theta(p^2_{1-}), \end{aligned} \tag{B.13}$$

$$= -i\frac{e^{-q_x|x-x'|}}{2\Omega\hbar v_{p_x}}\left[\epsilon\cos(p_x|x - x'|) + i\,\Omega\sin(p_x|x - x'|)\right]\left[n_+(k_y) + n_-(k_y)\hat{\sigma}_1\right]. \tag{B.14}$$

The anomalous Green's function results in

$$\begin{aligned} F_\epsilon(x - x') = & -i\frac{ms_x}{4\Omega\hbar^2}e^{-q_x|x-x'|}\left[\frac{\Delta\bar{k}_y\bar{p}_x}{p_x}e^{ip_x|x-x'|} - \frac{\Delta\bar{k}_y\bar{p}_x}{p_x}e^{-ip_x|x-x'|}\right](1 + \hat{\sigma}_1)\Theta(p^2_{1+})i\hat{\sigma}_2 \\ & -i\frac{ms_x}{4\Omega\hbar^2}e^{-q_x|x-x'|}\left[\frac{\Delta\bar{k}_y\bar{p}_x}{p_x}e^{ip_x|x-x'|} - \frac{\Delta\bar{k}_y\bar{p}_x}{p_x}e^{-ip_x|x-x'|}\right](1 - \hat{\sigma}_1)\Theta(p^2_{1-})\,i\hat{\sigma}_2, \end{aligned} \tag{B.15}$$

$$= -i\frac{e^{-q_x|x-x'|}}{2\Omega\hbar v_F}i\Delta\bar{k}_y\sin p_x(x - x')\left[n_+(k_y) + n_-(k_y)\hat{\sigma}_1\right]i\hat{\sigma}_2. \tag{B.16}$$

To obtain the Green's function at a surface, the four parts of the Green's in a uniform superconductor are necessary. We supply them as follows,

$$\hat{G}_{i\omega_n}(x-x') = -\frac{m}{2\Omega_n\hbar^2}\frac{e^{-q_x|x-x'|}}{p_x}\left[i\hbar\omega_n\cos(p_x|x-x'|) - \Omega_n\sin(p_x|x-x'|)\right] \tag{B.17}$$

$$\times\left[n_+(k_y) + n_-(k_y)\hat{\sigma}_1\right], \tag{B.18}$$

$$\hat{F}_{i\omega_n}(x-x') = -\frac{m}{2\Omega_n\hbar^2}\frac{e^{-q_x|x-x'|}}{p_x}\Delta\bar{p}_x\bar{k}_y\, i\sin p_x(x-x')\left[n_+(k_y) + n_-(k_y)\,\hat{\sigma}_1\right] i\,\hat{\sigma}_2, \tag{B.19}$$

$$-\underset{\sim}{\hat{G}}_{i\omega_n}(x-x') = -\frac{m}{2\Omega_n\hbar^2}\frac{e^{-q_x|x-x'|}}{p_x}\left[i\hbar\omega_n\cos(p_x|x-x'|) + \Omega_n\sin(p_x|x-x'|)\right] \tag{B.20}$$

$$\times\left[n_+(k_y) - n_-(k_y)\hat{\sigma}_1\right], \tag{B.21}$$

$$-\underset{\sim}{\hat{F}}_{i\omega_n}(x-x') = -\frac{m}{2\Omega_n\hbar^2}\frac{e^{-q_x|x-x'|}}{p_x}\Delta\bar{p}_x\bar{k}_y\, i\sin p_x(x-x')\left[-n_+(k_y) + n_-(k_y)\,\hat{\sigma}_1\right] i\,\hat{\sigma}_2, \tag{B.22}$$

where $\Omega_n = \sqrt{(\hbar\omega_n)^2 + \Delta_{\boldsymbol{k}}^2}$ and the particle-hole transformation is expressed by

$$\underset{\sim}{X}_{i\omega_n}(x, k_y) = X^*_{i\omega_n}(x, -k_y), \tag{B.23}$$

in this representation.

The solution of the Gor'kov equation for $\check{H}_2$ is represented as

$$\hat{G}_\epsilon(x-x') = \frac{1}{2\pi}\int_{-\infty}^{\infty} dk\, e^{ik(x-x')}\frac{1}{2}\left[\frac{(\epsilon+\xi_{2,+})(1+\hat{\sigma}_2)}{(\epsilon+i\delta)^2 - E_{2,+}^2} + \frac{(\epsilon+\xi_{2,-})(1-\hat{\sigma}_2)}{(\epsilon+i\delta)^2 - E_{2,-}^2}\right], \tag{B.24}$$

$$\hat{F}_\epsilon(x-x') = \frac{1}{2\pi}\int_{-\infty}^{\infty} dk\, e^{ik(x-x')}\frac{\Delta_{\boldsymbol{k}}}{2}\left[\frac{1-\hat{\sigma}_2}{(\epsilon+i\delta)^2 - E_{2,-}^2} + \frac{1+\hat{\sigma}_2}{(\epsilon+i\delta)^2 - E_{2,+}^2}\right] i\hat{\sigma}_2. \tag{B.25}$$

Within the first order α, the retarded Green's functions in an infinitely long superconductor are calculated as,

$$\hat{G}_\epsilon(x-x') = \frac{-i}{\Omega\,\hbar v_{k_x}}e^{-q_x|x-x'|}\left[\epsilon\cos k_x|x-x'| + i\Omega\sin k_x|x-x'|\right], \tag{B.26}$$

$$\hat{F}_\epsilon(x-x') = \frac{-i}{\Omega\,\hbar v_{k_x}}e^{-q_x|x-x'|}\left[i\Delta_{\boldsymbol{k}}\sin k_x(x-x') + \alpha\,\Delta\,\bar{k}_y\cos k_x(x-x')\hat{\sigma}_2\right] i\hat{\sigma}_2. \tag{B.27}$$

Here we apply the relation,

$$I_{2,\pm} = \frac{1}{2\pi}\int_{-\infty}^{\infty} dk\, e^{ik(x-x')}\,\frac{f(k,\xi_{2,\pm})}{(\epsilon+i\delta-E_{2,\pm})(\epsilon+E_{2,\pm})}, \tag{B.28}$$

$$= -i\frac{e^{-q_x|x-x'|}}{2\Omega\hbar v_x}\left[f(\mp\alpha k_F + s_x k_x, \Omega)\,e^{ik_x|x-x'|} + f(\mp\alpha k_F - s_x k_x, -\Omega)\,e^{-ik_x|x-x'|}\right], \tag{B.29}$$

where $v_x = \hbar k_x/m$ and $k_x = \sqrt{k_F^2 - k_y^2}$ is a real wavenumber.

Appendix C

Lippmann-Schwinger equation

The Lippmann-Schwinger equation relates the Green's function in the presence of a perturbation $\check{\mathbb{G}}$ to that in the absence of the perturbation $\check{G}$ as

$$\check{\mathbb{G}}_{i\omega_n}(\boldsymbol{r},\boldsymbol{r}') =\check{G}_{i\omega_n}(\boldsymbol{r},\boldsymbol{r}') + \int d\boldsymbol{r}_1\, \check{G}_{i\omega_n}(\boldsymbol{r},\boldsymbol{r}_1)\check{V}(\boldsymbol{r}_1)\, \check{\mathbb{G}}_{i\omega_n}(\boldsymbol{r}_1,\boldsymbol{r}'), \tag{C.1}$$

where $\check{V}(\boldsymbol{r})$ is the perturbation potential. In this appendix, we introduce a wall at $x = x_0$

$$\check{V}(\boldsymbol{r}) = V\,\delta(x - x_0)\,\hat{\tau}_3, \tag{C.2}$$

to divide an infinitely long superconductor into two semi-infinite superconductors. Thus $G_{i\omega_n}$ is the Green's function in a infinitely long superconductor in the x direction. Although the wall breaks the translational symmetry in the x direction, the superconductor is translational invariant in the y direction. Therefore it is possible to represent the Green's function as

$$\check{\mathbb{G}}_{i\omega_n}(\boldsymbol{r},\boldsymbol{r}') = \frac{1}{W}\sum_{k_y} \check{\mathbb{G}}_{i\omega_n}(x,x')e^{ik_y(y-y')}. \tag{C.3}$$

By substituting the expression into the equation, we find

$$\check{\mathbb{G}}_{i\omega_n}(x,x') = \check{G}_{i\omega_n}(x,x') + \check{G}_{i\omega_n}(x,x_0)\,V\hat{\tau}_3\,\check{\mathbb{G}}_{i\omega_n}(x_0,x'). \tag{C.4}$$

By putting $x = x_0$, we obtain the Green's function,

$$\check{\mathbb{G}}_{i\omega_n}(x_0,x') = \left[1 - \check{G}_{i\omega_n}(x_0,x_0)\,V\,\hat{\tau}_3\right]^{-1}\check{G}_{i\omega_n}(x_0,x'). \tag{C.5}$$

Finally, we reach an relation,

$$\check{\mathbb{G}}_{i\omega_n}(x,x') = \check{G}_{i\omega_n}(x,x') + \check{G}^{\mathrm{S}}_{i\omega_n}(x,x'), \tag{C.6}$$

$$\check{G}^{\mathrm{S}}_{i\omega_n}(x,x') = \check{G}_{i\omega_n}(x,x_0)\,V\hat{\tau}_3\,\left[1 - \check{G}^{(0)}_{i\omega_n}(x_0,x_0)\,V\,\hat{\tau}_3\right]^{-1}\check{G}_{i\omega_n}(x_0,x'). \tag{C.7}$$

The Green's function at a surface of a superconductor is calculated by taking a limit of $V \to \infty$. In the text, we input $x_0 = 0$ and analyze Eq. (C.7) near the surface $0 < x \lesssim \xi_0$ and $0 < x' \lesssim \xi_0$ with $\xi_0 = \hbar v_F/\pi\Delta$ being the coherence length.

Appendix **D**

Atiyah-Singer's Index

We briefly summarize the relation between the quantized value of the zero-bias conductance and an index $\mathcal{N}_{\text{ZES}}$. Let us begin with a BdG Hamiltonian for a spin-singlet SC with the x-type SOI in momentum space

$$H_{\text{BdG}}(\boldsymbol{k}) = (\xi_{\boldsymbol{k}} - \lambda_x k_x \hat{\sigma}_y)\tau_z - \Delta(\boldsymbol{k})\sigma_y \tau_y, \tag{D.1}$$

where $\xi_{\boldsymbol{k}} = \hbar^2 \boldsymbol{k}^2/2m - \mu$ is the kinetic energy of an electron with m being the mass of an electron and τ_i for $i = x, y$, and z are the Pauli's matrix in particle-hole space. To enhance the readability, we consider Hamiltonian in continuous space. The wave number on the Fermi surface is determined by

$$\xi_k + s\,\lambda_x\,k_x = 0, \quad s = \pm 1, \tag{D.2}$$

where $s = 1(-1)$ corresponds to the Fermi surface shifted to left (right) in Fig. 4.5(a). The wave numbers in the two directions satisfy

$$(k_x + s\tilde{\lambda}k_F)^2 + k_y^2 = (1+\tilde{\lambda}^2)k_F^2, \tag{D.3}$$

$$\tilde{\lambda} \equiv \frac{\lambda_x k_F}{2\mu} \ll 1. \tag{D.4}$$

The x-type SOI shifts the center of the Fermi surface to $\pm\tilde{\lambda}k_F$ on the k_x axis. The pair potential of a $d_{x^2-y^2}$-wave SC on the Fermi surface has nodes at $k_x = \pm k_y$. As a result, Eq. (4.14) is satisfied at the channels

$$\frac{k_F}{2}(\sqrt{\tilde{\lambda}^2+2} - \tilde{\lambda}) \leq |k_y| \leq \frac{k_F}{2}(\sqrt{\tilde{\lambda}^2+2} + \tilde{\lambda}), \tag{D.5}$$

for both the left and the right Fermi surfaces. The schematic figure of the pair potentials are shown in Fig. 4.5(a). The pair potential indicated by shaded area in Fig. 4.5(a) satisfies Eq. (4.14), indicating the appearance of surface Andreev bound state at each propagating channel. The number of such ZESs for the two spin sectors is estimated as

$$N = [4N_c\tilde{\lambda}]_{\text{G}}, \tag{D.6}$$

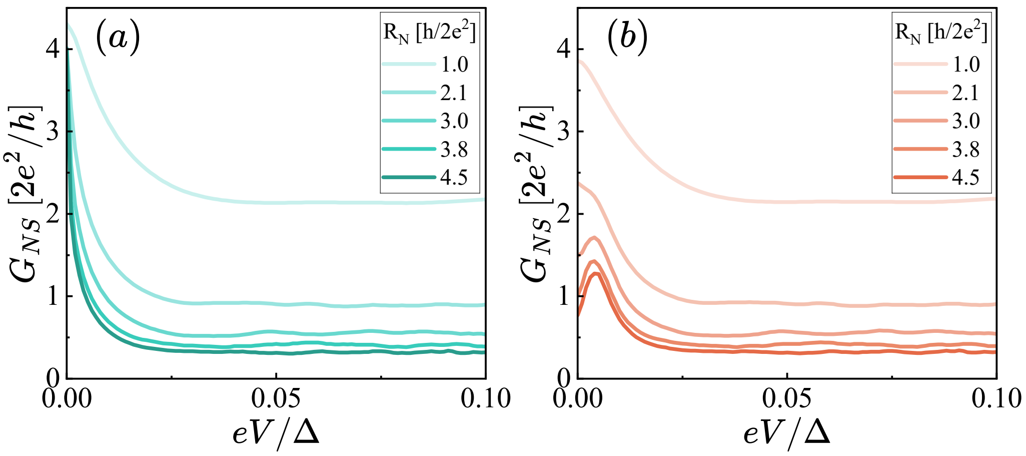

Figure D.1: The zero-bias conductance of a $d_{x^2-y^2}$-wave junction is plotted as a function of the bias voltage for several R_N. The results for the x-type at $\lambda_x = 0.5t$ are shown in (a). In (b), we choose $\lambda_x = 0.5t$ and $\lambda_y = 0.05t$.

where $N_c = Wk_F/\pi$ is the number of propagating channels for each spin sector, W is the width of the SC in the y direction, and $[\ldots]_G$ means the Gauss symbol providing the integer part of a number. As a result, the number of Andreev bound states at zero-energy is N at a clean surface of a $d_{x^2-y^2}$-wave SC with the x-type SOI. In other words, N represents the degree of the degeneracy at zero-energy states at a surface of a SC. Such a high degeneracy is a result of translational symmetry in the y direction of a clean SC. In a clean normal-metal / SC junction, the zero-energy states penetrate into the clean normal metal and form the perfect transmission channels.

To discuss effects of random potentials in a normal metal attached to a SC, the analysis of chiral property of zero-energy states is necessary.[14, 15] The BdG Hamiltonian in Eq. (D.1) preserves chiral symmetry,

$$\{H_{\mathrm{BdG}}, \Gamma_{\mathrm{BDI}}\}_+ = 0, \quad \Gamma_{\mathrm{BDI}} = \tau_x. \tag{D.7}$$

Since $\Gamma_{\mathrm{BDI}}^2 = 1$, the eigenvalues of Γ_{BDI} are 1 (positive chirality) and -1 (negative chirality). It is known that a zero-energy state of H_{BdG} is the eigenstate of Γ_{BDI}. Therefore such a zero-energy state has either the positive chirality or the negative chirality. The wave functions of the zero-energy states are calculated as

$$\psi_1 = \begin{pmatrix} i \\ 1 \\ -i \\ -1 \end{pmatrix} A e^{ik_y y} f(x), \;\; \psi_2 = \begin{pmatrix} 1 \\ i \\ -1 \\ -i \end{pmatrix} A e^{ik_y y} f(x) \tag{D.8}$$

where A is a normalization constant and $f(x)$ is a function localizing at a surface of a SC. It is easy to confirm that all of the zero-energy states belong to the negative chirality, as it satisfies $\Gamma_{\mathrm{BDI}}\psi_j = -\psi_j$ for $j = 1$ and 2. The Atiyah-Singer index is defined by

$$\mathcal{N}_{\mathrm{ZES}} = N_+ - N_-, \tag{D.9}$$

where N_+ (N_-) is the number of zero-energy states belonging to positive (negative) chirality. Therefore, the index is calculated as

$$|\mathcal{N}_{\mathrm{ZES}}| = \left[4N_c\tilde{\lambda}\right]_G. \tag{D.10}$$

The index $\mathcal{N}_{\mathrm{ZES}}$ is an invariant in the presence of chiral symmetry of the Hamiltonian. Here we calculate the index in a clean SC by assuming the translational symmetry in the y direction. The index remains unchanged even when the random impurity potentials

$$H_{\mathrm{imp}} = V(\boldsymbol{r})\,\tau_z, \tag{D.11}$$

enters the Hamiltonian in Eq. (D.1). This is because the random potential preserves chiral symmetry. In physics, $|\mathcal{N}_{\mathrm{ZES}}|$ represents the number of zero-energy states that penetrate into a dirty normal metal while retaining their high degeneracy and form the perfect transmission channels. The electric current through such perfect transmission channels is independent of R_{N}, whereas the electric current through usual tranmission channels decreases with increasing R_{N}. As a result, the minimum value of the conductance at zero bias is described by Eq. (4.20) [14, 15, 69].

Here we also demonstrate the effects of the y-type SOI additionally introduced to a $d_{x^2-y^2}$-wave SC with x-type SOI. The Hamiltonian of the y-type SOI

$$\lambda_y k_y \sigma_x, \tag{D.12}$$

breaks chiral symmetry in Eq. (D.7). Therefore, the index $\mathcal{N}_{\mathrm{ZES}}$ can no longer be defined and the conductance would deviate from its quantized value. In Fig. D.1, the conductance is plotted as a function of the bias voltage for several choices of R_{N}. We choose $(\lambda_x, \lambda_y) = (0.5t, 0)$ in (a) and $(\lambda_x, \lambda_y) = (0.5t, 0.05t)$ in (b). The minimum value of the zero-bias conductance is quantized as Eq. (4.20) in (a) irrespective of R_{N}. When we additionally introduce the y-type SOI in (b), the zero-bias conductance decreases gradually with increasing R_{N}. When λ_y is increased to λ_x, the results for RSOI in Fig. 4.2 do not exhibit any indication of the APE. The APE disappears under any perturbations breaking chiral symmetry.

Bibliography

[1] K. K. Likharev. Superconducting weak links. Rev. Mod. Phys., 51:101–159, Jan 1979.

[2] W. Belzig, C. Bruder, and Gerd Schön. Diamagnetic response of normal-metal–superconductor double layers. Phys. Rev. B, 53:5727–5733, Mar 1996.

[3] A. A. Golubov and M. Yu. Kupriyanov. Theoretical investigation of Josephson tunnel junctions with spatially inhomogeneous superconducting electrodes. Journal of Low Temperature Physics, 70(1):83–130, Jan 1988.

[4] Yasuhiro Asano. Disappearance of ensemble-averaged Josephson current in dirty superconductor-normal-superconductor junctions of d-wave superconductors. Phys. Rev. B, 64:014511, Jun 2001.

[5] Y. Tanaka and S. Kashiwaya. Anomalous charge transport in triplet superconductor junctions. Phys. Rev. B, 70:012507, Jul 2004.

[6] Yasuhiro Asano, Yukio Tanaka, and Satoshi Kashiwaya. Anomalous Josephson effect in p-wave dirty junctions. Phys. Rev. Lett., 96:097007, Mar 2006.

[7] Yukio Tanaka and Satoshi Kashiwaya. Theory of tunneling spectroscopy of d-wave superconductors. Phys. Rev. Lett., 74:3451–3454, Apr 1995.

[8] Yasuhiro Asano, Yukio Tanaka, and Satoshi Kashiwaya. Phenomenological theory of zero-energy andreev resonant states. Phys. Rev. B, 69:134501, Apr 2004.

[9] C. W. J. Beenakker. Random-matrix theory of quantum transport. Rev. Mod. Phys., 69:731–808, Jul 1997.

[10] A. Kastalsky, A. W. Kleinsasser, L. H. Greene, R. Bhat, F. P. Milliken, and J. P. Harbison. Observation of pair currents in superconductor-semiconductor contacts. Phys. Rev. Lett., 67:3026–3029, Nov 1991.

[11] Masatoshi Sato. Nodal structure of superconductors with time-reversal invariance and z_2 topological number. Phys. Rev. B, 73:214502, Jun 2006.

[12] Masatoshi Sato and Satoshi Fujimoto. Topological phases of noncentrosymmetric superconductors: Edge states, Majorana fermions, and non-Abelian statistics. Phys. Rev. B, 79:094504, Mar 2009.

[13] Masatoshi Sato, Yukio Tanaka, Keiji Yada, and Takehito Yokoyama. Topology of Andreev bound states with flat dispersion. Phys. Rev. B, 83:224511, Jun 2011.

[14] Satoshi Ikegaya, Yasuhiro Asano, and Yukio Tanaka. Anomalous proximity effect and theoretical design for its realization. Phys. Rev. B, 91:174511, May 2015.

[15] Satoshi Ikegaya, Shu-Ichiro Suzuki, Yukio Tanaka, and Yasuhiro Asano. Quantization of conductance minimum and index theorem. Phys. Rev. B, 94:054512, Aug 2016.

[16] Yasuhiro Asano, Yukio Tanaka, Alexander A. Golubov, and Satoshi Kashiwaya. Conductance spectroscopy of spin-triplet superconductors. Phys. Rev. Lett., 99:067005, Aug 2007.

[17] Shao-Pin Chiu, C. C. Tsuei, Sheng-Shiuan Yeh, Fu-Chun Zhang, Stefan Kirchner, and Juhn-Jong Lin. Observation of triplet superconductivity in $CoSi_2$/$TiSi_2$/heterostructures. Science Advances, 7(29):eabg6569, 2021.

[18] Kitomi Tsutsumi, Shigeru Takayanagi, Masayasu Ishikawa, and Toshiyuki Hirano. Superconductivity of intermetallic compound $CoSi_2$. Journal of the Physical Society of Japan, 64(6):2237–2238, 1995.

[19] Vivek Mishra, Yu Li, Fu-Chun Zhang, and Stefan Kirchner. Effects of spin-orbit coupling in superconducting proximity devices: Application to $CoSi_2$/$TiSi_2$ heterostructures. Phys. Rev. B, 103:184505, May 2021.

[20] Roman M. Lutchyn, Jay D. Sau, and S. Das Sarma. Majorana fermions and a topological phase transition in semiconductor-superconductor heterostructures. Phys. Rev. Lett., 105:077001, Aug 2010.

[21] Yuval Oreg, Gil Refael, and Felix von Oppen. Helical liquids and majorana bound states in quantum wires. Phys. Rev. Lett., 105:177002, Oct 2010.

[22] Xiao-Liang Qi, Taylor L Hughes, Srinivas Raghu, and Shou-Cheng Zhang. Time-reversal-invariant topological superconductors and superfluids in two and three dimensions. Phys. Rev. Lett., 102(18):187001, 2009.

[23] Yasuhiro Asano and Yukio Tanaka. Majorana fermions and odd-frequency cooper pairs in a normal-metal nanowire proximity-coupled to a topological superconductor. Phys. Rev. B, 87:104513, Mar 2013.

[24] Shun Tamura and Yukio Tanaka. Theory of the proximity effect in two-dimensional unconventional superconductors with Rashba spin-orbit interaction. Phys. Rev. B, 99:184501, May 2019.

[25] Jacob Linder and Alexander V. Balatsky. Odd-frequency superconductivity. Rev. Mod. Phys., 91:045005, Dec 2019.

[26] Jorge Cayao, Christopher Triola, and Annica M. Black-Schaffer. Odd-frequency superconducting pairing in one-dimensional systems. The European Physical Journal Special Topics, 229(4):545–575, Feb 2020.

[27] Yasuhiro Asano. Unconventional superconductivity and Josephson effect in superconductor/dirty normal metal/superconductor junctions. Journal of the Physical Society of Japan, 71(3):905–909, 2002.

[28] Y. Tanaka, Yu. V. Nazarov, and S. Kashiwaya. Circuit theory of unconventional superconductor junctions. Phys. Rev. Lett., 90:167003, Apr 2003.

[29] E. Bauer, G. Hilscher, H. Michor, Ch. Paul, E. W. Scheidt, A. Gribanov, Yu. Seropegin, H. Noël, M. Sigrist, and P. Rogl. Heavy fermion superconductivity and magnetic order in noncentrosymmetric $CePt_3Si$. Phys. Rev. Lett., 92:027003, Jan 2004.

[30] N. Reyren, S. Thiel, A. D. Caviglia, L. Fitting Kourkoutis, G. Hammerl, C. Richter, C. W. Schneider, T. Kopp, A.-S. Rüetschi, D. Jaccard, M. Gabay, D. A. Muller, J.-M. Triscone, and J. Mannhart. Superconducting interfaces between insulating oxides. Science, 317(5842):1196–1199, 2007.

[31] Lev P. Gor'kov and Emmanuel I. Rashba. Superconducting 2d system with lifted spin degeneracy: Mixed singlet-triplet state. Phys. Rev. Lett., 87:037004, Jul 2001.

[32] P. A. Frigeri, D. F. Agterberg, A. Koga, and M. Sigrist. Superconductivity without inversion symmetry: MnSi versus $CePt_3Si$. Phys. Rev. Lett., 92:097001, Mar 2004.

[33] Satoshi Fujimoto. Electron correlation and pairing states in superconductors without inversion symmetry. Journal of the Physical Society of Japan, 76(5):051008, 2007.

[34] Christopher R. Reeg and Dmitrii L. Maslov. Proximity-induced triplet superconductivity in rashba materials. Phys. Rev. B, 92:134512, Oct 2015.

[35] I. V. Bobkova and A. M. Bobkov. Quasiclassical theory of magnetoelectric effects in superconducting heterostructures in the presence of spin-orbit coupling. Phys. Rev. B, 95:184518, May 2017.

[36] Jorge Cayao and Annica M. Black-Schaffer. Odd-frequency superconducting pairing in junctions with Rashba spin-orbit coupling. Phys. Rev. B, 98:075425, Aug 2018.

[37] A. A. Abrikosov, L. P. Gor'kov, and I. E. Dzyaloshinski. Methods of Quantum Field Theory in Statistical Physics. Dover Publications, New York, 1975.

[38] Yasuhiro Asano. Andreev reflection in superconducting junctions. Springer, 2021.

[39] Satoshi Ikegaya, Shingo Kobayashi, and Yasuhiro Asano. Symmetry conditions of a nodal superconductor for generating robust flat-band Andreev bound states at its dirty surface. Phys. Rev. B, 97:174501, May 2018.

[40] Jason Alicea. Majorana fermions in a tunable semiconductor device. Phys. Rev. B, 81:125318, Mar 2010.

[41] Jiabin You, C. H. Oh, and Vlatko Vedral. Majorana fermions in s-wave noncentrosymmetric superconductor with Dresselhaus (110) spin-orbit coupling. Phys. Rev. B, 87:054501, Feb 2013.

[42] Y. Tanaka and A. A. Golubov. Theory of the proximity effect in junctions with unconventional superconductors. Phys. Rev. Lett., 98.

[43] B. Andrei Bernevig, J. Orenstein, and Shou-Cheng Zhang. Exact su(2) symmetry and persistent spin helix in a spin-orbit coupled system. Phys. Rev. Lett., 97:236601, Dec 2006.

[44] J. Koralek, C. Weber, J. Orenstein, B. A. Bernevig, Shou-Cheng Zhang, S. Mack, and D. D. Awschalom. Emergence of the persistent spin helix in semiconductor quantum wells. Nature, 458:610–613, 2009.

[45] M. Kohda, V. Lechner, Y. Kunihashi, T. Dollinger, P. Olbrich, C. Schönhuber, I. Caspers, V. V. Bel'kov, L. E. Golub, D. Weiss, K. Richter, J. Nitta, and S. D. Ganichev. Gate-controlled persistent spin helix state in (In,Ga)As quantum wells. Phys. Rev. B, 86:081306, Aug 2012.

[46] M. P. Walser, C. Reichl, W. Wegscheider, and G. Salis. Direct mapping of the formation of a persistent spin helix. Nature Physics, 8(10):757–762, Oct 2012.

[47] John Schliemann. Colloquium: Persistent spin textures in semiconductor nanostructures. Rev. Mod. Phys., 89:011001, Jan 2017.

[48] Y Tanaka, S Kashiwaya, and T Yokoyama. Theory of enhanced proximity effect by midgap Andreev resonant state in diffusive normal-metal/triplet superconductor junctions. Phys. Rev. B, 71(9):094513, Mar 2005.

[49] Yasuhiro Asano, Yukio Tanaka, Takehito Yokoyama, and Satoshi Kashiwaya. Josephson current through superconductor/diffusive-normal-metal/superconductor junctions: Interference effects governed by pairing symmetry. Phys. Rev. B, 74:064507, Aug 2006.

[50] S Ikegaya and Y Asano. Degeneracy of Majorana bound states and fractional josephson effect in a dirty sns junction. Journal of Physics: Condensed Matter, 28(37):375702, 2016.

[51] Yasuhiro Asano, Alexander A. Golubov, Yakov V. Fominov, and Yukio Tanaka. Unconventional surface impedance of a normal-metal film covering a spin-triplet superconductor due to odd-frequency cooper pairs. Phys. Rev. Lett., 107:087001, Aug 2011.

[52] L. J. Buchholtz and G. Zwicknagl. Identification of p-wave superconductors. Phys. Rev. B, 23:5788–5796, Jun 1981.

[53] Chia-Ren Hu. Midgap surface states as a novel signature for d^2_{xa}-x^2_b-wave superconductivity. Phys. Rev. Lett., 72:1526–1529, Mar 1994.

[54] Satoshi Kashiwaya and Yukio Tanaka. Tunnelling effects on surface bound states inunconventional superconductors. Reports on Progress in Physics, 63(10):1641, 2000.

[55] Y. Tanaka, Y. Asano, A. A. Golubov, and S. Kashiwaya. Anomalous features of the proximity effect in triplet superconductors. Phys. Rev. B, 72:140503, Oct 2005.

[56] S. Higashitani, Y. Nagato, and K. Nagai. Proximity effect between a dirty Fermi liquid and superfluid ^{3}He. Journal of Low Temperature Physics, 155(1-2):83–97, 2009.

[57] Yukio Tanaka, Masatoshi Sato, and Naoto Nagaosa. Symmetry and topology in superconductors –odd-frequency pairing and edge states–. Journal of the Physical Society of Japan, 81(1):011013, 2012.

[58] Shun Tamura, Shintaro Hoshino, and Yukio Tanaka. Odd-frequency pairs in chiral symmetric systems: Spectral bulk-boundary correspondence and topological criticality. Phys. Rev. B, 99(18):184512, 2019.

[59] Takehito Yokoyama, Yukio Tanaka, and Naoto Nagaosa. Anomalous meissner effect in a normal-metal–superconductor junction with a spin-active interface. Phys. Rev. Lett., 106(24):246601, 2011.

[60] S. Mironov, A. Mel'nikov, and A. Buzdin. Vanishing Meissner effect as a hallmark of in–plane Fulde-Ferrell-Larkin-Ovchinnikov instability in superconductor–ferromagnet layered systems. Phys. Rev. Lett., 109:237002, Dec 2012.

[61] Shu-Ichiro Suzuki and Yasuhiro Asano. Paramagnetic instability of small topological superconductors. Phys. Rev. B, 89:184508, May 2014.

[62] Chris LM Wong, Jie Liu, Kam Tuen Law, and Patrick A Lee. Majorana flat bands and unidirectional Majorana edge states in gapless topological superconductors. Phys. Rev. B, 88(6):060504, 2013.

[63] Timo Hyart, Anthony R Wright, and Bernd Rosenow. Zeeman-field-induced topological phase transitions in triplet superconductors. Phys. Rev. B, 90(6):064507, 2014.

[64] S Rubanov and PR Munroe. FIB-induced damage in silicon. Journal of Microscopy, 214(3):213–221, 2004.

[65] Lucille A Giannuzzi et al. Introduction to focused ion beams: instrumentation, theory, techniques and practice. Springer Science & Business Media, 2004.

[66] Ming-Hao Liu, Kuo-Wei Chen, Son-Hsien Chen, and Ching-Ray Chang. Persistent spin helix in rashba-dresselhaus two-dimensional electron systems. Phys. Rev. B, 74(23):235322, 2006.

[67] Makoto Kohda and Gian Salis. Physics and application of persistent spin helix state in semiconductor heterostructures. Semiconductor Science and Technology, 32(7):073002, 2017.

[68] Jaechul Lee, Satoshi Ikegaya, and Yasuhiro Asano. Odd-parity pairing correlations in a d-wave superconductor. Phys. Rev. B, 103:104509, Mar 2021.

[69] Satoshi Ikegaya and Yasuhiro Asano. Stability of flat zero-energy states at the dirty surface of a nodal superconductor. Phys. Rev. B, 95:214503, Jun 2017.

[70] YS Chen, Stefan Fält, Werner Wegscheider, and Gian Salis. Unidirectional spin-orbit interaction and spin-helix state in a (110)-oriented GaAs/(Al, Ga) As quantum well. Phys. Rev. B, 90(12):121304, 2014.

[71] LL Tao and Evgeny Y Tsymbal. Persistent spin texture enforced by symmetry. Nature communications, 9(1):2763, 2018.

[72] Moh Adhib Ulil Absor and Fumiyuki Ishii. Doping-induced persistent spin helix with a large spin splitting in monolayer SnSe. Phys. Rev. B, 99(7):075136, 2019.

[73] Moh Adhib Ulil Absor and Fumiyuki Ishii. Intrinsic persistent spin helix state in two-dimensional group-IV monochalcogenide MX monolayers (M= Sn or Ge and X= S, Se, or Te). Phys. Rev. B, 100(11):115104, 2019.

[74] Carmine Autieri, Paolo Barone, Jagoda Sławińska, and Silvia Picozzi. Persistent spin helix in rashba-dresselhaus ferroelectric $CsBiNb_2O_7$. Physical Review Materials, 3(8):084416, 2019.

[75] Haoqiang Ai, Xikui Ma, Xiaofei Shao, Weifeng Li, and Mingwen Zhao. Reversible out-of-plane spin texture in a two-dimensional ferroelectric material for persistent spin helix. Physical Review Materials, 3(5):054407, 2019.

[76] Hosik Lee, Jino Im, and Hosub Jin. Emergence of the giant out-of-plane rashba effect and tunable nanoscale persistent spin helix in ferroelectric snte thin films. Applied Physics Letters, 116(2), 2020.

[77] Jagoda Sławińska, Frank T Cerasoli, Priya Gopal, Marcio Costa, Stefano Curtarolo, and Marco Buongiorno Nardelli. Ultrathin snte films as a route towards all-in-one spintronics devices. 2D Materials, 7(2):025026, 2020.

[78] G. E. Blonder, M. Tinkham, and T. M. Klapwijk. Transition from metallic to tunneling regimes in superconducting microconstrictions: Excess current, charge imbalance, and supercurrent conversion. Phys. Rev. B, 25:4515–4532, Apr 1982.

[79] Chr Bruder. Andreev scattering in anisotropic superconductors. Phys. Rev. B, 41(7):4017, 1990.

[80] T. Ando. Quantum point contacts in magnetic fields. Phys. Rev. B, 44:8017–8027, Oct 1991.

[81] Andreas P Schnyder, Shinsei Ryu, Akira Furusaki, and Andreas WW Ludwig. Classification of topological insulators and superconductors in three spatial dimensions. Phys. Rev. B, 78(19):195125, 2008.

[82] IC Fulga, F Hassler, AR Akhmerov, and CWJ Beenakker. Scattering formula for the topological quantum number of a disordered multimode wire. Phys. Rev. B, 83(15):155429, 2011.

[83] Yasuhiro Asano. Disappearance of ensemble-averaged josephson current in dirty superconductor-normal-superconductor junctions of d-wave superconductors. Phys. Rev. B, 64:014511, Jun 2001.

[84] G. R. Stewart, Z. Fisk, J. O. Willis, and J. L. Smith. Possibility of Coexistence of Bulk Superconductivity and Spin Fluctuations in UPt3. Springer Netherlands, 1993.

[85] H. R. Ott, H. Rudigier, Z. Fisk, and J. L. Smith. Ube_{13}: An unconventional actinide superconductor. Phys. Rev. Lett., 50:1595–1598, May 1983.

[86] S. S. Saxena, P. Agarwal, K. Ahilan, F. M. Grosche, R. K. W. Haselwimmer, M. J. Steiner, E. Pugh, I. R. Walker, S. R. Julian, P. Monthoux, G. G. Lonzarich, A. Huxley, I. Sheikin, D. Braithwaite, and J. Flouquet. Superconductivity on the border of itinerant-electron ferromagnetism in UGe_2. Nature, 406(6796):587–592, 2000.

[87] Sheng Ran, Chris Eckberg, Qing-Ping Ding, Yuji Furukawa, Tristin Metz, Shanta R. Saha, I-Lin Liu, Mark Zic, Hyunsoo Kim, Johnpierre Paglione, and Nicholas P. Butch. Nearly ferromagnetic spin-triplet superconductivity. Science, 365(6454):684–687, 2019.

[88] Lin Jiao, Sean Howard, Sheng Ran, Zhenyu Wang, Jorge Olivares Rodriguez, Manfred Sigrist, Ziqiang Wang, Nicholas P. Butch, and Vidya Madhavan. Chiral superconductivity in heavy-fermion metal ute2. Nature, 579(7800):523–527, 2020.

[89] Y. S. Hor, A. J. Williams, J. G. Checkelsky, P. Roushan, J. Seo, Q. Xu, H. W. Zandbergen, A. Yazdani, N. P. Ong, and R. J. Cava. Superconductivity in Cu_x Bi_2 Se_3 and its implications for pairing in the undoped topological insulator. Phys. Rev. Lett., 104:057001, Feb 2010.

[90] Satoshi Sasaki, M. Kriener, Kouji Segawa, Keiji Yada, Yukio Tanaka, Masatoshi Sato, and Yoichi Ando. Topological superconductivity in Cu_2 Bi_2 Se_3. Phys. Rev. Lett., 107:217001, Nov 2011.

[91] Sankar Das Sarma, Michael Freedman, and Chetan Nayak. Majorana zero modes and topological quantum computation. npj Quantum Information, 1:15001, 2015.

[92] Satoshi Ikegaya, Jaechul Lee, Andreas P. Schnyder, and Yasuhiro Asano. Strong anomalous proximity effect from spin-singlet superconductors. Phys. Rev. B, 104:L020502, Jul 2021.

[93] L. F. Mattheiss and D. R. Hamann. Electronic structure and properties of $CoSi_2$. Phys. Rev. B, 37:10623–10627, Jun 1988.

[94] Kitomi Tsutsumi, Shigeru Takayanagi, Masayasu Ishikawa, and Toshiyuki Hirano. Superconductivity of intermetallic compound $CoSi_2$. Journal of the Physical Society of Japan, 64(6):2237–2238, 1995.

[95] Patrick A. Lee and Daniel S. Fisher. Anderson localization in two dimensions. Phys. Rev. Lett., 47:882–885, Sep 1981.

[96] Vivek Mishra, Yu Li, Fu-Chun Zhang, and Stefan Kirchner. Effects of spin-orbit coupling on proximity-induced superconductivity. Phys. Rev. B, 107:184505, May 2023.

[97] LN Bulaevskii, VV Kuzii, and AA Sobyanin. Superconducting system with weak coupling to the current in the ground state. JETP lett, 25(7):290–294, 1977.

[98] Alexandre I Buzdin, LN Bulaevskii, and SV Panyukov. Critical-current oscillations as a function of the exchange field and thickness of the ferromagnetic metal F in an sfs josephson junction. JETP lett, 35(4):178–180, 1982.

[99] F. S. Bergeret, A. F. Volkov, and K. B. Efetov. Long-range proximity effects in superconductor-ferromagnet structures. Phys. Rev. Lett., 86:4096–4099, Apr 2001.

[100] A. A. Golubov, M. Yu. Kupriyanov, and E. Il'ichev. The current-phase relation in josephson junctions. Rev. Mod. Phys., 76:411–469, Apr 2004.

[101] V. V. Ryazanov, V. A. Oboznov, A. Yu. Rusanov, A. V. Veretennikov, A. A. Golubov, and J. Aarts. Coupling of two superconductors through a ferromagnet: Evidence for a π junction. Phys. Rev. Lett., 86:2427–2430, Mar 2001.

[102] T. Kontos, M. Aprili, J. Lesueur, F. Genêt, B. Stephanidis, and R. Boursier. Josephson junction through a thin ferromagnetic layer: Negative coupling. Phys. Rev. Lett., 89:137007, Sep 2002.

[103] R. S. Keizer, S. T. B. Goennenwein, T. M. Klapwijk, G. Miao, G. Xiao, and A. Gupta. A spin triplet supercurrent through the half-metallic ferromagnet CrO_2. Nature, 439(7078):825–827, Feb 2006.

[104] M. S. Anwar, F. Czeschka, M. Hesselberth, M. Porcu, and J. Aarts. Long-range supercurrents through half-metallic ferromagnetic CrO_2. Phys. Rev. B, 82:100501, Sep 2010.

[105] Trupti S. Khaire, Mazin A. Khasawneh, W. P. Pratt, and Norman O. Birge. Observation of spin-triplet superconductivity in Co-based josephson junctions. Phys. Rev. Lett., 104:137002, Mar 2010.

[106] J. W. A. Robinson, J. D. S. Witt, and M. G. Blamire. Controlled injection of spin-triplet supercurrents into a strong ferromagnet. Science, 329(5987):59–61, 2010.

[107] Yasuhiro Asano, Yukio Tanaka, and Alexander A. Golubov. Josephson effect due to odd-frequency pairs in diffusive half metals. Phys. Rev. Lett., 98:107002, Mar 2007.

[108] V. Braude and Yu. V. Nazarov. Fully developed triplet proximity effect. Phys. Rev. Lett., 98:077003, Feb 2007.

[109] Matthias Eschrig and Tomas Löfwander. Triplet supercurrents in clean and disordered half-metallic ferromagnets. Nature Physics, 4(2):138–143, 2008.

[110] Matthias Eschrig. Spin-polarized supercurrents for spintronics: a review of current progress. Reports on Progress in Physics, 78(10):104501, 2015.

[111] Hiroshi Irie, Yuichi Harada, Hiroki Sugiyama, and Tatsushi Akazaki. Josephson coupling through one-dimensional ballistic channel in semiconductor-superconductor hybrid quantum point contacts. Phys. Rev. B, 89(16):165415, 2014.

[112] Hideaki Takayanagi, Tatsushi Akazaki, and Junsaku Nitta. Observation of maximum supercurrent quantization in a superconducting quantum point contact. Phys. Rev. Lett., 75(19):3533, 1995.

[113] Anatoly F Volkov and Hideaki Takayanagi. ac long-range phase-coherent effects in mesoscopic superconductor–normal metal structures. Phys. Rev. Lett., 76(21):4026, 1996.

[114] Taketomo Nakamura, Yoshiaki Hashimoto, Yu Iwasaki, Shinobu Ohya, Masaaki Tanaka, Shingo Katsumoto, et al. Proximity-induced superconductivity in a ferromagnetic semiconductor (In, Fe) As. In Journal of Physics: Conference Series, volume 969, page 012036. IOP Publishing, 2018.

[115] Taketomo Nakamura, Le Duc Anh, Yoshiaki Hashimoto, Shinobu Ohya, Masaaki Tanaka, and Shingo Katsumoto. Evidence for spin-triplet electron pairing in the proximity-induced superconducting state of an Fe-doped InAs semiconductor. Phys. Rev. Lett., 122(10):107001, 2019.

[116] Eugene A Demler, GB Arnold, and MR Beasley. Superconducting proximity effects in magnetic metals. Phys. Rev. B, 55(22):15174, 1997.

[117] A Buzdin. Direct coupling between magnetism and superconducting current in the josephson φ 0 junction. Phys. Rev. Lett., 101(10):107005, 2008.

[118] Xin Liu, JK Jain, and Chao-Xing Liu. Long-range spin-triplet helix in proximity induced superconductivity in spin-orbit-coupled systems. Phys. Rev. Lett., 113(22):227002, 2014.

[119] FS Bergeret and IV Tokatly. Singlet-triplet conversion and the long-range proximity effect in superconductor-ferromagnet structures with generic spin dependent fields. Phys. Rev. Lett., 110(11):117003, 2013.

[120] FS Bergeret and IV Tokatly. Spin-orbit coupling as a source of long-range triplet proximity effect in superconductor-ferromagnet hybrid structures. Phys. Rev. B, 89(13):134517, 2014.

[121] Sol H Jacobsen and Jacob Linder. Giant triplet proximity effect in π-biased josephson junctions with spin-orbit coupling. Phys. Rev. B, 92(2):024501, 2015.

[122] Sol H Jacobsen, Jabir Ali Ouassou, and Jacob Linder. Critical temperature and tunneling spectroscopy of superconductor-ferromagnet hybrids with intrinsic rashba-dresselhaus spin-orbit coupling. Phys. Rev. B, 92(2):024510, 2015.

[123] Andreas Costa, Petra Högl, and Jaroslav Fabian. Magnetoanisotropic Josephson effect due to interfacial spin-orbit fields in superconductor / ferromagnet / superconductor junctions. Phys. Rev. B, 95(2):024514, 2017.

[124] S Mironov and A Buzdin. Spontaneous currents in superconducting systems with strong spin-orbit coupling. Phys. Rev. Lett., 118(7):077001, 2017.

[125] Yasuhiro Asano. Numerical method for dc josephson current between d-wave superconductors. Phys. Rev. B, 63(5):052512, 2001.

[126] Gert Eilenberger. Transformation of gorkov's equation for type ii superconductors into transport-like equations. Zeitschrift für Physik A Hadrons and nuclei, 214(2):195–213, Apr 1968.

[127] Peter Fulde and Richard A. Ferrell. Superconductivity in a strong spin-exchange field. Phys. Rev., 135:A550–A563, Aug 1964.

[128] AI Larkin and Yu N Ovchinnikov. Nonuniform state of superconductors. Soviet Physics-JETP, 20(3):762–762, 1965.